YEMLİHA ALTINTAS

SYNTHESIS AND CHARACTERIZATION OF SEMICONDUCTOR COLLOIDAL QUANTUM DOTS AND QUANTUM WELLS FOR OPTOELECTRONIC DEVICES

AGU 2018

SYNTHESIS AND CHARACTERIZATION OF SEMICONDUCTOR COLLOIDAL QUANTUM DOTS AND QUANTUM WELLS FOR OPTOELECTRONIC DEVICES

A Ph.D. Thesis

By

Yemliha ALTINTAS

December 2018

ABDULLAH GÜL UNIVERSITY

SYNTHESIS AND CHARACTERIZATION OF SEMICONDUCTOR COLLOIDAL QUANTUM DOTS AND QUANTUM WELLS FOR OPTOELECTRONIC DEVICES

A THESIS
SUBMITTED TO THE DEPARTMENT OF MATERIALS SCIENCE AND MECHANICAL ENGINEERING AND THE GRADUATE SCHOOL OF ENGINEERING AND SCIENCES OF
ABDULLAH GÜL UNIVERSITY
IN PARTIAL FULFILLMENT OF THE REQUIREMENTS
FOR THE DEGREE OF
DOCTOR OF PHILOSOPHY

By
Yemliha ALTINTAS
December 2018

SCIENTIFIC ETHICS COMPLIANCE

I hereby declare that all information in this document has been obtained in accordance with academic rules and ethical conduct. I also declare that, as required by these rules and conduct, I have fully cited and referenced all materials and results that are not original to this work.

Yemliha ALTINTAS

REGULATORY COMPLIANCE

Ph.D. thesis titled "Synthesis and Characterization of Semiconductor Colloidal Quantum Dots and Quantum Wells for Optoelectronic Devices" has been prepared in accordance with the Thesis Writing Guidelines of the Abdullah Gül University, Graduate School of Engineering and Science.

Prepared By	Advisor
Yemliha ALTINTAS	Assoc. Prof. Evren Mutlugün

Head of the Materials Science and Mechanical Engineering Program
Prof. Murat DURANDURDU

ACCEPTANCE AND APPROVAL

Ph.D. thesis titled "Synthesis and Characterization of Semiconductor Colloidal Quantum Dots and Quantum Wells for Optoelectronic Devices" was prepared by Yemliha ALTINTAS, which has been accepted by the jury in the Materials Science and Mechanical Engineering Graduate Program at Abdullah Gül University, Graduate School of Engineering and Science.

25/12/2018

JURY:

Advisor : Assoc. Prof. Dr. Evren MUTLUGÜN

Member : Assoc. Prof. Dr. Hakan USTA

Member : Assoc. Prof. Dr. M. İbrahim T. ÖZDÜR

Member : Assoc. Prof. Dr. M. Serdar ÖNSES

Member : Prof. Dr. Savaş SÖNMEZOĞLU

APPROVAL:

The acceptance of this Ph.D. thesis has been approved by the decision of the Abdullah Gül University, Graduate School of Engineering and Science, Executive Board dated ….. /….. / …….. and numbered ……..……. .

Graduate School Dean
Prof. İrfan ALAN

ABSTRACT

SYNTHESIS AND CHARACTERIZATION OF SEMICONDUCTOR COLLOIDAL QUANTUM DOTS AND QUANTUM WELLS FOR OPTOELECTRONIC DEVICES

Yemliha ALTINTAS

Ph.D. in Materials Science and Mechanical Engineering

Supervisor: Assoc. Prof. Evren MUTLUGÜN

December 2018

In the last few decades, semiconductor quantum dots (QDs) have become one of the important branches of the nanomaterials thanks to their size (2-10 nm) dependent optical properties and excitonic features, narrow emission bandwidth, excellent photo and thermal stabilities. All these properties have named QDs as exotic nanomaterials for optoelectronic applications such as light emitting diodes, solar cells and colloidal lasers. The main focus of this thesis study is to demonstrate high quality and stable colloidal nanocrystals synthesis and present their optoelectronic applications.

To realize this purpose, high quality, monodisperse and pure color emitting CdSe/ZnS QDs have been synthesized and high-quality white light emitting diodes (w-LED) have been obtained by using free-standing flexible polymeric films of these QDs. The results obtained with these films have been presented both for display and lighting applications with white light parameters of NTSC color gamut of 122.5 (CIE-1931), CRI of 88.6, LER of 190 lm/Woptand CCT of 2763 K.

In addition to CdSe based QDs, due to the environmental concern towards Cd-based nanomaterials, we focused our attention to Cd-free QDs as well. Evaluation and the performance of the QDs for various applications depend on their optical properties as QY, FWHM and tunable emission wavelength. To improve optical properties of the environmentally friendly QDs, various synthesis protocols and synthesis recipe have been used with different chemicals, precursor concentrations and structure. By the help

of optimized precursor concentration and proposed structure of alloyed core/shell InPZnS/ZnS QDs, 78 % of QY and 45 nm of FWHM have been obtained by carefully designed synthesis recipe. The variation of the optical properties of the QDs have been characterized with steady state and time resolved photoluminescence (TRPL) analysis by monitoring the synthesis products at all stages of the synthesis. The lifetime of the alloyed core increased from 20.3 ns to 50.4 ns with shell coating by the suppression of the nonradiative decay components. For further improvements of Cd-free QDs synthesis, we have systematically studied the type and concentration of the Zn-precursor. Green emissive QDs have been synthesized with 87% of QY, having 54 nm of FWHM. Emission kinetics and Förster Resonance Energy Transfer (FRET) efficiency between donor and acceptor pairs of the green and red emitting QDs have been investigated by using steady state and TRPL analysis. Efficient green emissive Cd-free QDs have provided 70.3 % FRET efficiency by mixing with red emissive Cd-free QDs in their polymeric film structure.

As an alternative matrix to polymer structures to incorporate the nanocrystals, salt macrocrystals have recently emerged as an efficient platform to keep QY and optical properties of the emitters in their solid forms. FRET efficiency, photo-stability and white-LED performance of Cd-free QDs embedded salt pellets have been investigated by varying the acceptor to donor ratio in the salt matrix. 65% of FRET efficiency, 84.7 of CRI with 324 lm/Wopt of high LER has been achieved from pellets form of Cd-free QDs.

We have also focused on the synthesis of the two-dimensional colloidal quantum wells to efficiently use them in optical gain and laser application. However, low QY and stability of the core/shell nanoplatelets (NPLs) that produced with c-ALD methods limits their performance in an application. So, first we have started to improve their optical properties and stability both in solution and film form. Finally, near-unity emitting CdSe/ZnS core/shell NPLs have been successfully synthesized by using hot-injection shell growth approach. Synthesized NPLs with our new synthesis protocol exhibited outstanding photo, thermal-stability and optical gain performance with lasing thresholds as low as 7 μJ cm^{-2}.

Keywords: semiconductor nanocrystals, quantum dots, optoelectronic applications, colloidal gain, white-LED, FRET

ÖZET

OPTOELEKTRONİK AYGITLAR İÇİN YARIİLETKEN KOLLOİDAL KUANTUM NOKTALARI VE KUANTUM KUYULARININ SENTEZİ VE KARAKTERİZASYONU

Yemliha ALTINTAS
Malzeme Bilimi ve Makina Mühendisliği Anabilim Dalı Doktora
Tez Yöneticisi: Doç. Dr. Evren MUTLUGÜN

Aralık 2018

Yarıiletken kuantum noktalar son derece küçük boyutları (2-20 nm), boyutlarına bağlı değişen eksitonik özellikleri, mükemmel derecede ışık ve ısı stabilite özellikleri sayesinde son birkaç on yılda nanomalzemelerin önemli dallarından biri haline gelmiştir. Kuantum noktaların tüm bu özellikleri onları ışık yayan diyotlar, güneş pilleri ve kolloidal lazer gibi optoelektronik uygulamalar için egzotik nanomalzemeler olarak adlandırmasını sağlamıştır. Bu tez çalışmasının ana odağı yüksek kalitede ve stabil nanokristal malzemeler üretmek ve onların optoelektronik uygulamalarını sunmaktır.

Bu amacı gerçekleştirmek için yüksek kalitede ve saf renkte ışık yayan CdSe/ZnS kuantum noktaları sentezlendi ve bu kuantum noktalar kullanılarak hazırlanan esnek polimerik filmler yardımıyla da yüksek kalitede beyaz ışık yayan diyotlar elde edildi. Bu filmlerin kullanılması ile elde edilen sonuçlar 122,5 NTSC renk gamı (CIE-1931), 88,6 CRI, 190 lm/Wopt LER ve 2763 K CCT değerleri sayesinde hem ekran hem de aydınlatma uygulamaları için sunulmuştur.

Cd-tabanlı nanomalzemelere yönelik çevresel kaygılar nedeniyle Cd-tabanlı nanomalzemelere ek olarak dikkatimizi Cd-içermeyen kuantum noktacıkları üzerine odakladık. Birçok farklı uygulamada kuantum noktaların performanslarının değerlendirilmesi onların QY, FWHM ve değişebilen ışıma dalga boyu gibi optik özelliklerine bağlıdır. Çevreye duyarlı kuantum noktaların optik özelliklerini

iyileştirmek için birçok sentez yöntem ve tarifi, farklı kimyasallar, konsantrasyonlar ve yapılar ile denendi. Dikkatlice hazırlanan sentez tarifi, kimyasalların optimize edilmesi ve önerilen InPZnS/ZnS alaşımlı çekirdek/kabuk yapısının yardımı ile % 78 QY ve 45 nm FWHM değerleri elde edildi. Tüm sentez aşamalarında sentezden numune almak suretiyle kuantum noktaların optik özelliklerin değişimi kararlı hal ve zaman çözünürlüklü fotolüminesans analizi ile karakterize edildi. Alaşımlı çekirdeğin ışıma ömrü, 20,3 ns' den 50,4 ns' ye kabuk kaplama ve ışımasız lifetime bileşenlerinin baskılanmasıyla arttı. Kadmiyum içermeyen kuantum noktaların optik özelliklerinin daha da artması için sentezde kullanılan Zn çeşidi ve konsantrasyonunu sistematik olarak çalıştık. Yeşil ışıyan kuantum noktalar 54 nm FWHM ve % 87 kuantum verimlilik ile sentezlendi. Yeşil ve kırmızı ışıyan kuantum noktaların verici ve alıcı çiftleri arasındaki ışıma kinetiği ve FRET verimliliği kararlı hal ve zaman çözünürlüklü fotolüminesans analizi yardımıyla araştırıldı. Verimli yeşil ışıyan kuantum noktalar ile kırmızı ışıyan kadmiyum içermeyen kuantum noktaların polimerik filmler içerisindeki karışımı ile % 70,3 FRET verimliliğini sağladı.

Son yıllarda, ışıyan numunelerin film içerisindeki optik özelliklerinin ve veriminin korunması için nanokristallerin polimerik yapı ile kullanılmasına alternatif olarak tuz kristalleri verimli bir platform olarak ortaya çıktı. FRET verimliliği, ışık stabilitesi ve tuz tablet içerisine konulmuş kadmiyum içermeyen kuantum noktaların beyaz-LED performansı tuz karışımı içerisindeki alıcı ve verici arasındaki konsantrasyon oranının değiştirilmesiyle araştırıldı. % 65 FRET verimliliği 324 lm/Wopt LER ile 84,7 CRI değerleri kadmiyum içermeyen kuantum noktalardan elde edildi.

Ayrıca iki boyutlu kuantum kuyuların sentezi ve bu malzemelerin verimli bir şekilde optic kazanç ve lazer uygulamalarında kullanılmasına odaklandık. c-ALD metodu ile üretilen çekirdek/kabuk yapıdaki nanolevhaların (NPL)' lerin düşük verim ve düşük kararlılıkları onların optik kazanç ve lazer uygulamalarında kullanılmalarını kısıtlıyordu. Bu nedenle, ilk olarak numunelerin optik özellik ve kararlılıklarını hem solüsyon içerisinde hem film içerisinde iyileştirmeye çalıştık. Nihayetinde %100 verimli CdSe/ZnS çekirdek/kabuk NPL' leri sıcak ekleme kabuk büyütme yaklaşımı ile başarılı bir şekilde sentezlendi. Yeni sentez protokolümüz ile sentezlenen NPL' ler,

sıradışı ısı ve ışık kararlılıkları ve 7 μJ cm^{-2} kadar düşük eşik değerine sahip optik kazanç performansı sergiledi.

Anahtar kelimeler: Yarıiletken nanokristaller, kuantum noktalar, optoelektronik uygulamalar, kolloidal kazanç, beyaz-LED, FRET.

Acknowledgements

I would like to point out my gratitude to my advisor Assoc. Prof. Evren Mutlugun for his support and guidance during my thesis study. Thanks to his invaluable support, I have overcome the difficulties that I lived during my studies.

I would like to thank my thesis committee members Assoc. Prof. Hakan Usta, Assoc. Prof. İbrahim Özdür, Assoc. Prof. Serdar Önses and Prof. Dr. Savaş Sönmezoğlu for their constructive and valuable suggestions and evaluations. I would like to thank Prof. H. Volkan Demir and his group members for their help to improve my research experiences.

I am thankful to Solid State Lighting group leader Dr. Ekaterina Nannen and her group members Julia, Fabian and Enes in NETZ, Duisburg. I would like to thank Mutlugun research group members Ahmet, Emre and Eren. I would like to specially thank our previous group member of Dr. Mohammed Younis Talpur.

I would like to acknowledge the support from Abdullah Gul University Scientific Research Project no's FDK-2017-96, BAP-FAB-010, Turkish Academy of Sciences The Young Scientists Award Program (TUBA-GEBIP 2017) and TUBITAK grant nos. 114E107, 117E249 and 5140079.

Finally, I would like to thank my wife and children with my love for their percipience. This thesis work would not be possible without their support and understanding.

Table of Contents

List of Figures

List of Tables

Chapter 1

1. Introduction

Colloidal quantum dots (CQDs) are one of the exciting classes of the nanocrystal semiconductor materials. Their fascinating properties such as being extremely small size, bandgap engineerable structure, size-composition and shape dependent tunable optical properties and solution based low cost fabrication process make them promising materials for all nanomaterial related science. Up to now from the first discovering of this materials in 1980 [1], QDs have been used in many optoelectronic applications such as solar cells [2], light emitting diodes[3], [4], photodetector [5] and laser[6], [7], thanks to the the strong interaction between excited light and their own nature that have discrete energy level and electronic structure. QDs have also gained substantial interest for biological applications such as in vivo imaging and detection for photodynamic studies [8][9][10].

With the interest of the researchers boosted up by the discovery of the quantum confinement properties of the QDs [1] [11], the understanding of the chemical and physical aspect of the QDs took place in the last few decades. Owing to the smaller or comparable size of the QDs as compared to the exciton Bohr radius, QDs have quantum confinement effect as their bandgap can be changed with their sizes. Therefore, emission color of the same QDs red shifted with the increasing size of the QDs and blue shifted with the reduced size of the QDs. Monodisperse, efficient and reproducible QDs synthesis was able to succeed after the reporting of the first hot-injection synthesis study by Bawendi group in 1993[12].

To improve capability of the QDs, various kinds of QDs have been synthesized by using II-IV group elements as CdSe, CdS, CdTe and III-V group elements as InP, ZnSe and ZnS, IV-IV group elements as PbS and PbSe. Whereas spectral range in

electromagnetic spectrum of the IV-IV group elements and III-V group elements (except InP) comprise only near infrared and UV-light region, respectively. Spectral range of InP and II-IV group elements enclose nearly full-visible spectrum of the light.

Only core QDs has low QYs and optical properties are highly sensitive to the environmental factors. Due to the high surface to volume ratio of the nanocrystalline QDs, optical properties of the QDs mostly depend on their surface. Surface trap and surface-related defect as dangling bounds reduces quantum yield (QY) of QDs and increases the nonradiative recombination rate within the structure [13]. The protection of the core surface from environmental factors was able to be achieved by shell growth on the surface of the core. Whereas the different shell materials have been used by coating of the core surface to obtain different types of semiconductor materials such as Type-I, quasi-Type II, Type-II and inverse Types (I and II).

The most convenient shell material to protect core surface was found as ZnS having wider bandgap as 3.54 eV when compared to other shell materials as CdS, ZnSe or CdTe. ZnS shell materials are commonly used in Type-I structure to confine electron and hole into the core structure. Due to the isolated excitons (electron and hole pairs) of the core/shell QDs from surrounding environment, QY and temperature and UV stability of the QDs sample increases within Type-I structure. All of these advantages of type-I structure and using ZnS material as a shell, CdSe/ZnS and InZnP/ZnS core/shell QDs have been efficiently synthesized within the scope of this thesis for various applications with high QYs, narrow spectral bandwidth and high stability.

Different type of the core/shell structure uses different purpose and application. Type-I structure of the core/shell have been generally selected for their high luminescence with increased stability of the sample and enhanced recombination efficiency of the exciton in the core/shell structure commonly for lighting and display applications. Core/shell with Type-II structure commonly used in solar cell (SC) and photodetector applications to efficiently collect photogenerated excitons via light harvesting device structure. Emission wavelength of the QDs is also very important to use and choose proper core/shell type and kind of the QD materials for specific application. Red and near-far infrared emitting materials such as CdTe, PbSe and PbS have been generally used for SC application. However, due to the potential toxicity of the Pb and Cd containing QDs, recently red and near infrared emitting CuInS, CuInGaS,

CuInZnS (or Se) and CuInSe based core and core/shell QDs have been preferred for SCs instead of Cd and Pb-containing QDs.

QDs have been efficiently used as color converter in light emitting diodes (LED) application to achieve high quality and desirable white-LED parameter as color temperature (CT), luminous efficacy of optical radiation (LER), national TV standard color (NTSC) and color gamut. In QLEDs, activated QDs with charge-injection have been used as emissive material to obtain pure color emissive LED device thanks to their narrow bandwidth, low cost of synthesis and solution processable production. In this thesis work, to gain high standard white-LED device application proposed on display and lighting, color convertor materials of green and red emissive QDs have been utilized with their significantly enhanced optical properties via modification and setting of the new synthesis protocol. White light parameters of constructed white-LED have been investigated well-prepared polymeric films of the QDs which are hybridized commercial blue-LED to acquire white spectrum. To further improve desired white-color parameters, four color mixing approach have been also employed by mixing green, red and yellow emitting QDs.

When the different colors of the QD mix in a matrix, one may face energy transfer phenomena from donor-QDs to acceptor-QDs. The physical phenomena of energy transfer between two QDs or QDs and other organic molecules have been mostly observed in the mixture of these materials in a solid film or in solution with concentrated samples. This transfer can be observed when some conditions are met such as proximity of emitters and spectral overlap between absorbance of the acceptor and PL-emission of the donor. Energy transfer phenomena generally studied within Cd-based samples. Environmental concerns have triggered to achieve high quality Cd-free QDs, commonly based on InP/ZnS core/shell QDs. Therefore, we spanned most of the thesis time to advance InP-based Cd-free QDs synthesis and their applications. To clarify the physics and beneficial effect of the energy transfer mechanism in Cd-free QDs polymeric films, green and red Cd-free QDs have been mixed in polymeric matrix and measured steady-state and time-resolved PL characterizations. FRET efficiency in the films of the QDs has been calculated by using the lifetime of the samples as 70%.

The endeavors obtaining ultra-pure color emissive material having ultra-narrow bandwidth result in the emergence of the two-dimensional Nanoplatelets as an exciting

branch of the semiconductor colloidal nanomaterials. Unique properties such as their quantum well-like structure, high absorption coefficient-cross section and giant oscillator strength made NPLs one of the best materials for colloidal laser and optical gain materials. While growing considerable interest of the researcher on NPLs, low stability and low QYs of NPLs did not figure out up to now. We attempt numerous syntheses to stabilize and improve optical properties of the NPLs. Finally, CdSe/ZnS core/shell NPLs have been synthesized with near-unity QYs and high stability by using hot-injection shell growth approach.

In addition to this Introduction part as Chapter 1, the scopes and organization of this thesis study is presented as follows;

In Chapter 2, the brief information of the QDs structure and different kind of synthesis have been summarized with used characterization techniques.

In Chapter 3, green, yellow and red emissive CdSe/ZnS core/shell QDs synthesis, characterization and white-LED applications have been given with polymeric films of the QDs and white-LED spectrum. White-color parameters have also investigated for efficient white LED generation.

In Chapter 4, highly efficient Cd-free InP-based QDs synthesis and characterization have been presented by using optimization of the all parameter and precursors and then full-visible spectral color have been showed with their optical properties.

In Chapter 5, Cd-free green emissive InZnP/ZnS QDs have been demonstrated to achieve high quality donor species by changing 5-different kind of Zn-precursor and after selection of the best kind of Zn precursor, then the concentration of the Zn precursor increased to obtain high QYs. From the polymeric films of different ratio of the red and green-emissive InP/ZnS QDs, FRET efficiency has been calculated as 70 %.

In Chapter 6, InP/ZnS QDs embedded macrocrystals salt matrix and their white-LED device application have been efficiently reported to protect QY of the QDs in a solid matrix.

In Chapter 7, CdSe/ZnS core/shell NPLs synthesis and their outstanding temperature stability and optical properties have been shown by using hot-injection shell growth approach. Ultra-low optical gain threshold of this sample have been also highlighted both with and without annealing samples.

Chapter 2

2. Scientific Background and Characterizations

2.1 Colloidal Quantum Dots

Within the scope of thesis, quantum dots and nanoplatelets synthesis, characterization and application carried out with various synthesis procedures, characterization techniques and applications. This thesis part includes basic knowledge of QDs structure, quantum confinement effect and synthesis of the CQDs.

Bandgap of the CQDs can be changed with their size, composition and shape. Size dependent bandgap and discrete electronic properties of CQDs structure, thanks to the confinement effects, gives rise to many possibilities to engineer CQDs via thickness and different heterostructures in CQDs synthesis and device fabrication.

Average size of the nanocrystal QDs are as small as from 2 to 20 nm which compose of approximately 10^2 to 10^3 atoms. The relationship between average size, bandgap and emission color of the QDs have been presented in Figure 2.1.1. Without changing of the type of the used semiconductor, effective bandgap of the QDs can be adjusted for specific application as shown in Figure 2.1.1 or can be used to find a way to increase efficiency of their performance in an application.

Electron and hole pair which are called exciton forms when semiconductor material are excited a photon with higher than their band gap energy. Photogenerated

electron and hole in bulk semiconductor are generally weakly bounded each other with columbic interaction due to their high electric constant. They are freely moved in bulk semiconductor as free carrier. Columbic binding energy of exciton in nanocrystals QDs owing to their quantum confinement effects is much higher than bulk semiconductors. Owing to the strong excitonic feature of the QDs, broad and strong absorption behavior observed in their absorption spectra. When compared to the organic emissive counterpart, QDs have higher QYs, narrower spectral linewidth and faster PL-lifetime.

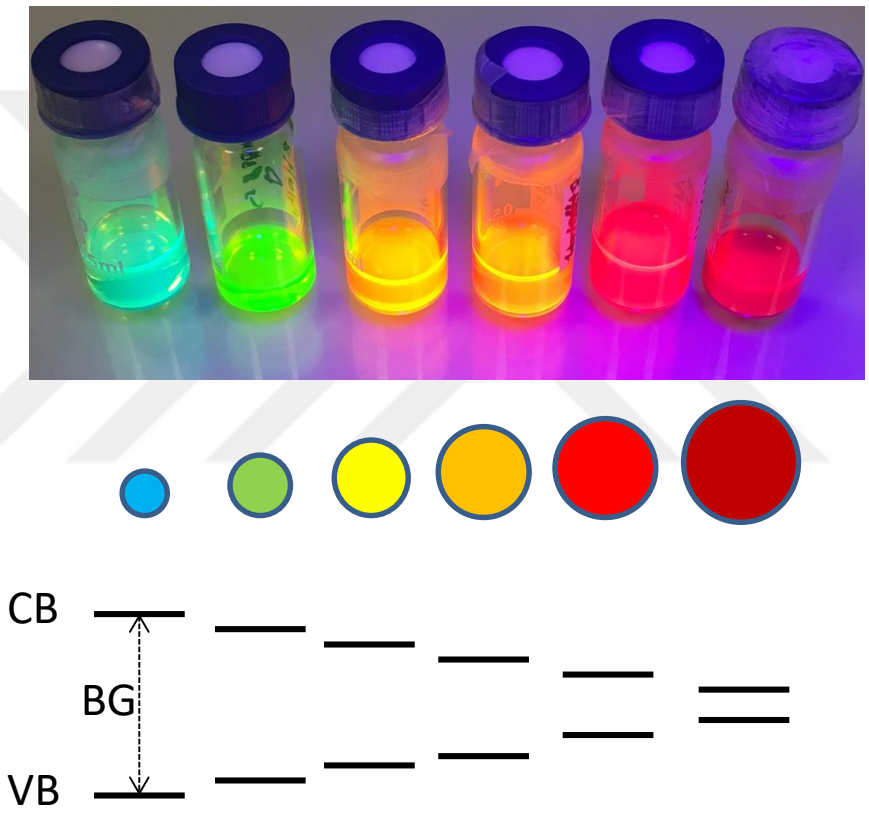

Figure 2.1. 1 Different sized and same kind of QDs have been presented with UV-illumination and their emitting light depends on their size. When the size of the QDs increased, their bandgap energy decreased. CB: Conduction Band, VB: Valance Band and BG: Bandgap

Core/shell QDs compose of three significant components as core, shell and ligand as shown Figure 2.1.2. Core can be form with II-IV, III-V or IV-IV group elements as binary, ternary or quaternary semiconductor materials such as CdSe, CdSeS or

CdZnSeS. Emission color and bandgap of the QDs mostly depend on core materials. Emission color of the QDs can be changed with alloyed structure. Quantum efficiency and stability of the core can be dramatically enhanced with shell growth on core QDs owing to the effective passivation of the core surface. Ligand provides solubility of the QDs in organic or water phase solution. Ligand also serves as stabilizer on QDs and the surface of the QD can be functionalized with different type of ligands.

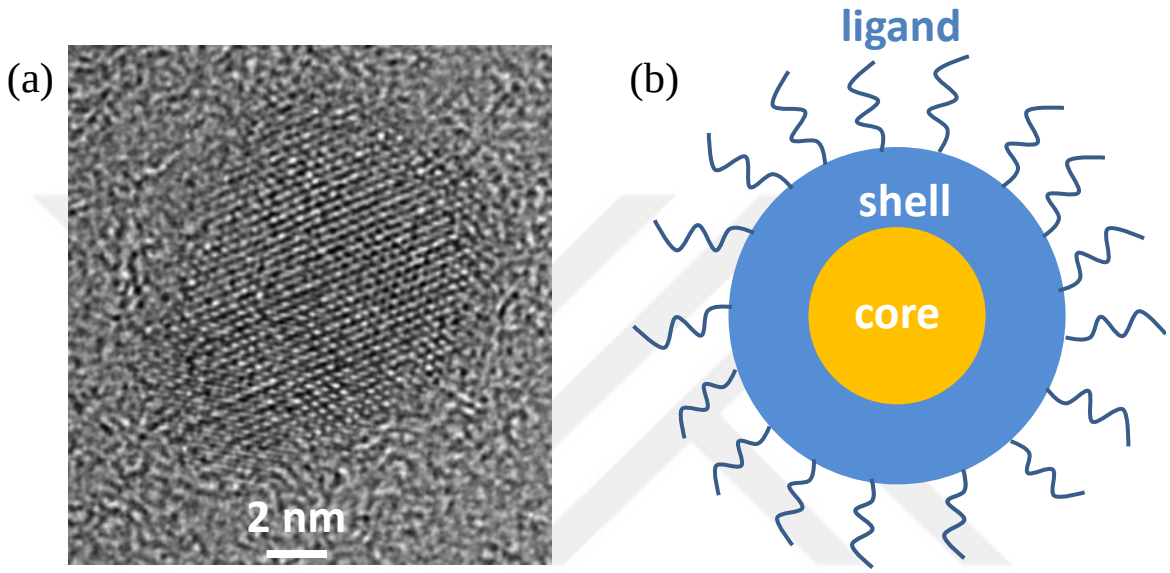

Figure 2.1. 2 (a) HR-TEM image of the core/shell sample synthesized in our laboratory and (b) schematic representation of the core/shell QDs structure.

Unique properties such as ability to tune easier their optical properties, their functionalized surface and solution processable low-cost production make QDs one of the mostly used colloidal nanoparticles for optoelectronic applications in recent years.

2.1.1 Nanocrystal Synthesis and Growth Mechanism

Day by day, the interest of the researchers on the synthesis of QDs has increased with their enhanced size, shape and composition tunable excitonic and electronic properties.

CQD synthesis has been performed by using solvent having high boiling point, precursor to provide forming of the monomer, ligand to stabilize formed NCs. [14]–[16]

The dissolution of the molecular precursor is enabled by used solvent having high boiling temperature. Three stages should be carefully designed to form nanocrystal during the synthesis as monomer forming, nucleation and growth. The decomposition of the molecular precursor of the synthesis takes place at high temperatures and the reactivity of the monomers generally depends on side group of the molecules [17]. Uniformity of the synthesized nanocrystals, size and shape of the QDs mostly effected used ligands which play critical role for all aspect of optical and structural properties of the QDs and it is dynamically bounded to the surface of the QDs [18]–[20]. The stability of the synthesized QDs in organic solvents also is provided by their ligands. High quality, crystalline, monodisperse and stable nanocrystals can be synthesized by selection and optimization of the proper solvent, precursor and their ligands [15], [21].

In order to understand nucleation and growth mechanism in the synthesis of the NCs, La Mer and Dinegar [22] presented a model to obtain uniform and monodisperse nanocrystals by the help of separation of the stages of nucleation and growth as shown in Figure 2.1.1.1.

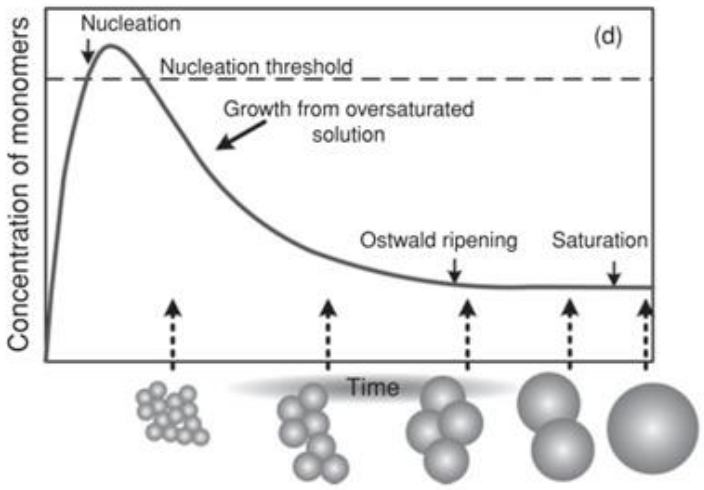

Figure 2.1.1. 1 The history of the QDs synthesis and the stages which are nucleation, growth, Oswald ripening and saturation. Reprinted from [23]**.**

Nucleation and growth stages of the reaction can be separated by the fast injection of the precursor into the solution. After injection, homogenous nucleation of the small sized nanocrystals rapidly starts with the decomposition of the monomers which has critical concentration to form homogenous nucleation. When the concentration of the

monomer decreased under the critic levels for nucleation, then subsequent stage of the growth is started to provide uniform nanocrystals. After the depletion of the monomers into the reaction, smaller NCs dissolve into the reaction and bigger NCs grow with dissolving of the smaller NCs. This phenomena is called as Ostwald ripening [24].

In order to get uniform size distribution from the synthesis, all these stages should carefully been carried out by using suitable type and accurate concentration of the precursors, solvents and ligands. In last decade, the attempt searching of less toxic or non-toxic precursor has increased to protect environmental, human life and health.

2.1.2 Nanocrystal Quantum Dots and Nanoplatelets Synthesis

Highly emissive CdSe/ZnS, InP/ZnS core/shell QDs and 4ML CdSe core, CdSe/ZnS core/shell NPLs have been synthesized by using solution based chemical synthesis procedure and shlenk-line system possessing high performance optical properties. In order to get monodisperse, efficient and stable NCs, hot-injection methods have been preferred to optimize synthesis condition and precursors. Synthesis system in our laboratory has been demonstrated in Figure 2.1.2.1.

Figure 2.1.2. 1 Nanocrystal synthesis system composes of shlenk-line, heater, vacuum pump, vacuum gauge, condenser, clips and temperature probe.

Detailed synthesis procedures for different kind of materials were given in following chapter of this thesis work.

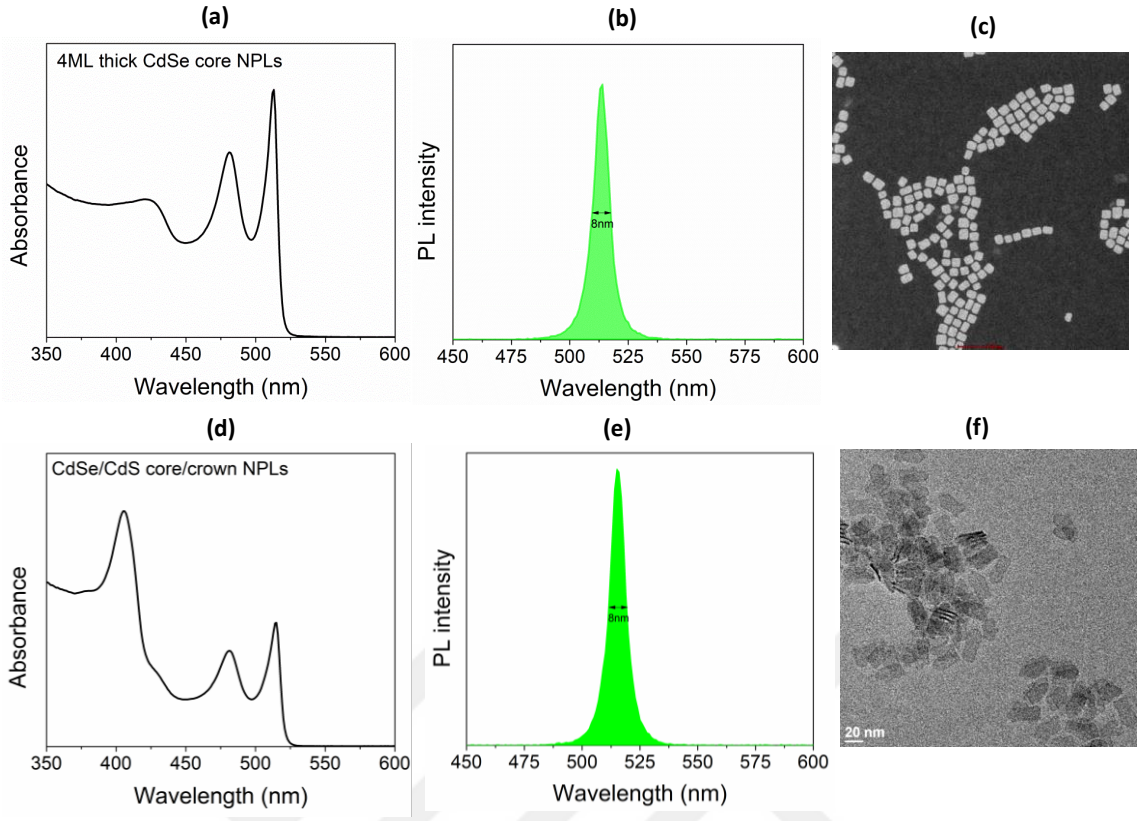

Figure 2.1.2. 2 (a), (b) and (c) PL, Abs and TEM image of 4ML thick CdSe core NPLs and (d), (e) and (f) PL, Abs and TEM image of CdSe/CdS core/crown Nanoplatelets.

While FWHM and maximum achieved QY of 4ML CdSe core NPLs are 8 nm and 38 %, FWHM and QYs of CdSe/CdS core/crown NPLs 8nm and 85% (Figure 2.1.2.2). Due to the low stability of the core and core/crown NPLs as compare to QDs, we synthesized high quality and stable core/shell NPLs with hot-injection approach. Synthesis recipe and our results have been presented in Chapter 7.

2.2 Characterizations

Synthesized CQDs and NPLs have been characterized with structural and optical characterization techniques to reveal their emission characteristics, crystal structure, shape, lifetime and excitonic properties.

2.2.1 Optical Characterizations

For optical characterization, photoluminescence (PL), absorbance (Abs), time-resolved photoluminescence (TRPL) and quantum yield (QY) measurements have been carried out by using sufficient amount of sample in solution.

2.2.1.1 Absorbance and Photoluminescence Measurements

As-synthesized QDs and NPLs first have cleaned 2 times with acetone-methanol mixture which is generally used for QDs sample or ethanol used for NPLs cleaning. In final centrifuge, precipitated NCs have been dispersed in toluene or hexane. PL and Absorbance measurements have been performed with and Cary Eclipse Fluorescence Spectroscopy and Genesys 10S UV-Vis Spectrometer, respectively, as shown in their images in Figure 2.2.1.1.1.

Figure 2.2.1.1. 1 Absorbance spectrometer and Photoluminescence spectrometer used in our experiments

Absorption peak, PL-emission peak and stock shift of the samples have been obtained from Absorption and PL measurements. The thickness of the NPLs sample can be determined from their Absorption- PL spectra. The uniformity of the NPLs also can be determined from their PL-Absorption spectruma due to their strong pronounced peak positions in their spectra. The variation of optical properties during shell growth was obtained by measuring PL and Absorption from samples taken at different times as given in Figure 2.2.1.1.2.

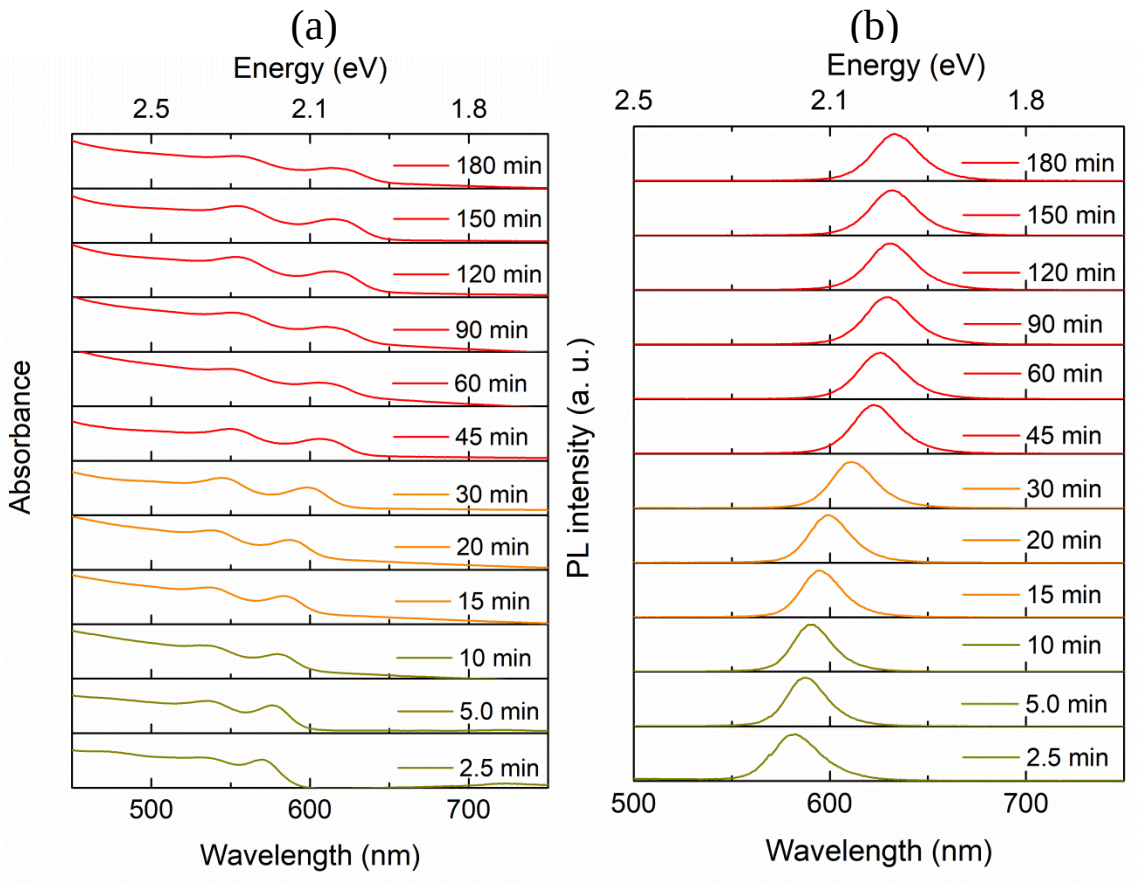

Figure 2.2.1.1. 2 Abs and PL spectra of the aliqout samples which are taken during shell growth at different times. This sample have been synthesized in our laboratuary.

2.2.1.2 Quantum Yield Measurement

One of the important optical properties of the QDs is their quantum yield which shows the performance of the emitting light. Basic explanation of the QY is the ratio between number of photons emitted from the QDs to the number of absorbed photons by the QD. QYs of the emitters can be calculated with two methods, as relative comparison methods with dye and absolute QY measurements system.

For example, quantum efficiency of CdSe/ZnS QDs green and red emitting QDs are calculated by using the dyes Rh6G for green QD and Sulphorhodamine 101 for red QDs with relative QY measurement technique which are reported by Grabolle [25]. QY of the Rh 6G and Sulphorhodamine 101 in ethanol are 95 and 90%, respectively. Useful range for Rh 6G and Sulphorhodamine 101 to accurately calculate QYs are 460-490 nm and 510-560 nm, respectively. Intersection of the absorbance spectrum of the green QDs and Rh 6G should be 460-490 nm and for red QDs and Sulphorhodamine 101 should be

510-560 nm. In order to prevent re-absorption during the measurements, absorbance value of the intersection point must be under the 0.2. After obtaining of the intersection in absorbance spectra, PL spectrum of the QDs and dye have been recorded at same excitation wavelength of the intersection to calculate under the area of the PL-spectra as shown in Figure 2.2.1.2.1.

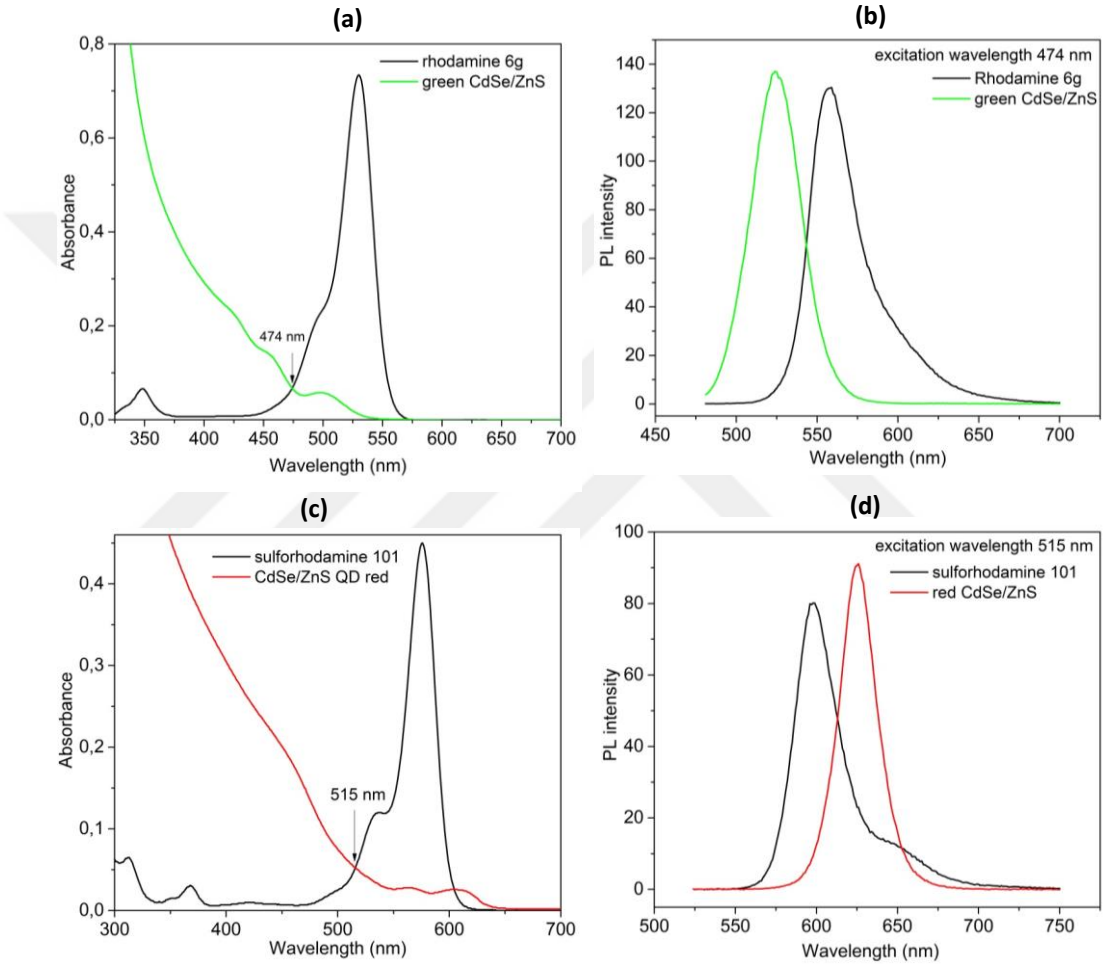

Figure 2.2.1.2. 1 An example of QY measurements methodology. Reprinted with permission from [26]**. Copyright 2016 IOP Publishing.**

QYs can be calculated following equation;

$$\Phi_{\text{flu}}^{\text{sample}} = \Phi_{\text{flu}}^{\text{reference}} \left(\frac{F^{\text{sample}}}{F^{\text{reference}}} \right) \left(\frac{\eta^{\text{sample}}}{\eta^{\text{reference}}} \right) \left(\frac{\text{Abs}^{\text{reference}}}{\text{Abs}^{\text{sample}}} \right) \quad \textbf{(2.2.1-1)}$$

(Φ: QY, F: integrated area under the PL spectrum, η: refractive index of the solvents, Abs: absorbance at determined wavelength)

2.2.1.3 Time Resolved Photoluminescence Measurements

The lifetime and emission kinetics of the samples have been measured by using time-resolved PL spectroscopy with Picoquant Fluotime 200 as given in Figure 2.2.1.3.1. Flouresence decay cure of the sample have been determined from time duration between generation of the laser pulse and accumulated photon, both are recorded by TRF with the unit of TCSPC (time-correlated single photon counting). All decay curves of the samples have been fit and analysed multi-exponential fit parameter keeping chie-square value near unity.

Figure 2.2.1.3. 1 Photo of the Picoquant Fluotime 200 used for the measurements of the lifetime.

2.2.2 Structural Characterizations

For structural characterization of the samples, X-ray photoelectron spectroscopy (XPS), X-ray diffraction spectroscopy (XRD) and transmission electron microscopy (TEM) methods have been carefully implemented by using prepared solid films of the samples under appropriate conditions.

2.2.2.1 X-Ray Photoelectron Spectroscopy

Surface properties and elemental analysis of the sample can be clarified with X-ray photoelectron spectroscopy measurements (XPS). To prepare samples for XPS measurements, two or three times cleaned concentrated samples have been spin-coated on cleaned Si substrate. Binding energies of the elements composing of the sample and elemental quantization can be determined with XPS measurements.

The intensity of the photoelectron coming from surface of the sample when the sample is excited X-ray during the measurements shows the concentration of the element inside the structure. The overlap binding energies of different sample in XPS spectra should be properly fitted and calculated for elemental quantization. In our measurements, the overlap between S-2p and Se-3p with their spin-orbital binding energies has been showed in Figure 2.2.2.1.1 and carefully fit to determine accurate elemental quantization for the structure of CdSe/ZnS nanocrystal sample.

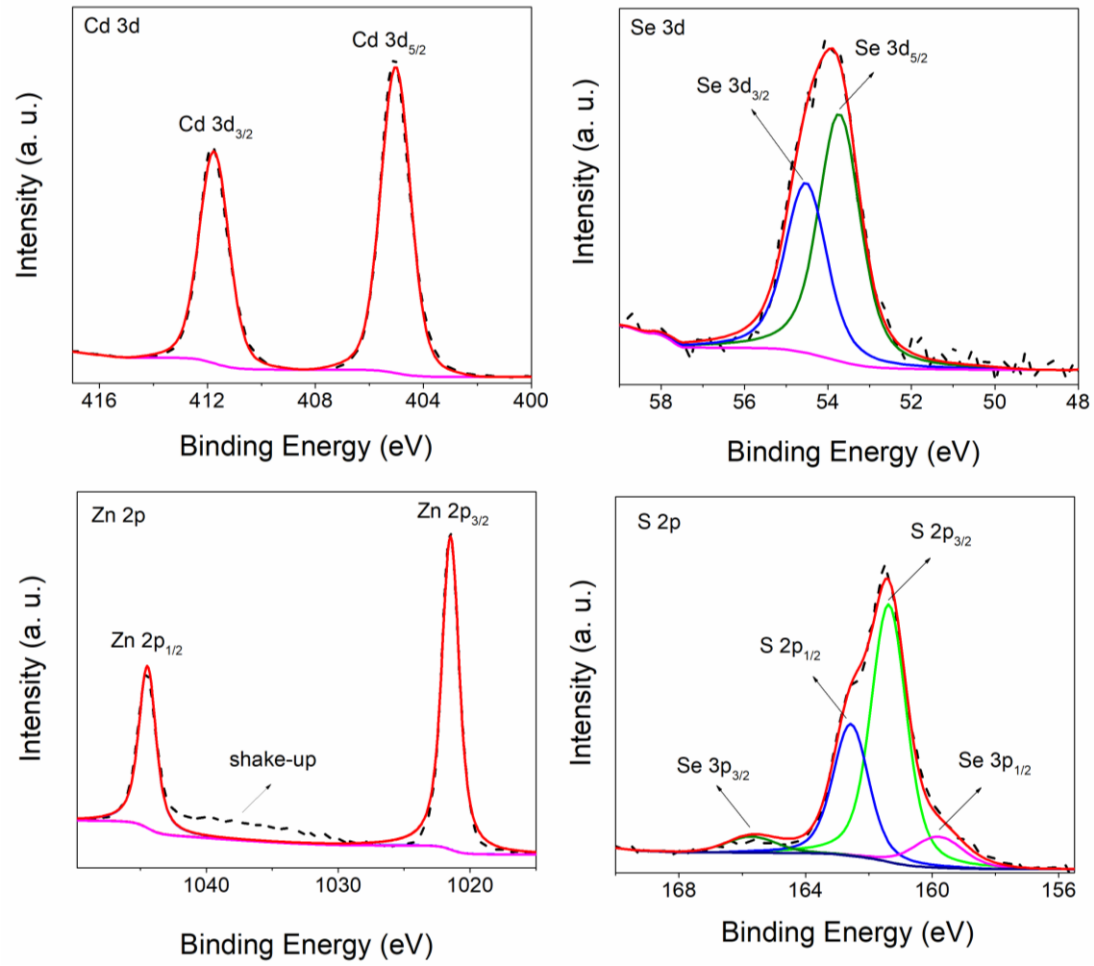

Figure 2.2.2.1. 1 XPS measurements of the CdSe/ZnS nanocrystals and elemental binding energies of the Cd-3d, Se-3d, Zn-2p and S-2p.

2.2.2.2 X-Ray Diffraction Spectroscopy

Optical properties of the QDs have been affected with their crystals structure and their crystal structure can be efficiently determined by using X-ray diffraction spectroscopy measurements. During the synthesis to control the crystal structure of the synthesized sample are important to obtain with desired shape or properties of the QDs. While the synthesis of the rod-like growth on CdSe QDs are realized on wurtzite type crystal structure, tetrapod shaped growth on CdSe QDs are possible with zinc-blende type crystal structure [27]. XRD pattern of the core/shell QDs has ranked the material between core and shell, owing to the heterostructure of the core/shell QDs as shown in Figure 2.2.2.2.1.

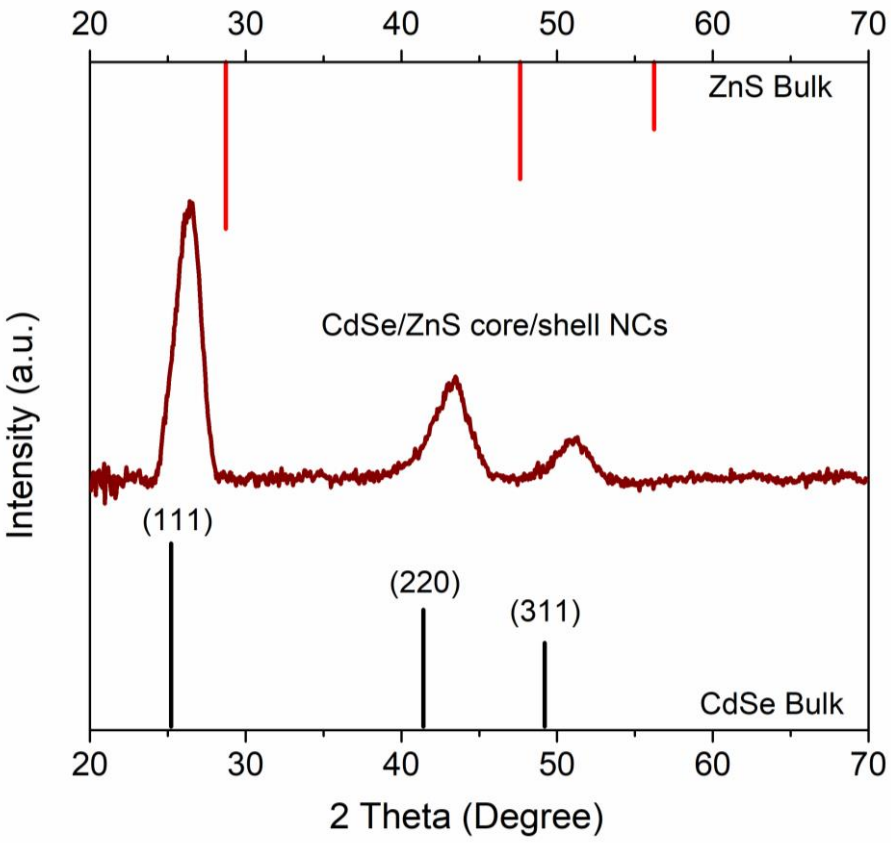

Figure 2.2.2.2. 1 XRD-pattern of core/shell CdSe/ZnS NCs. 2 Theta values of zinc blend bulk CdSe and ZnS semiconductor are also inserted in this graph with their crystal orientation planes as (111), (220) and (311).

2.2.2.3 Transmission Electron Microscopy

Surface and structural properties as shape, size, composition, in plane orientation of the atoms (crystalline structure) and morphological knowledges can be detected by using high-resolution TEM, HAADF-STEM and EDX analysis. To prevent charging effect on sample, synthesized NCs have been cleaned at least 5 times with ethanol to lift excess ligands of the NCs. Then 8 µL of diluted sample in hexane have been dropped on Cu-grid and solvent is completely evaporated before using. The thicknesses of the nanoplatelets have been also determined from the TEM images. Different kind of nanocrystals synthesized in our laboratories has been presented in Figure 2.2.2.3.1.

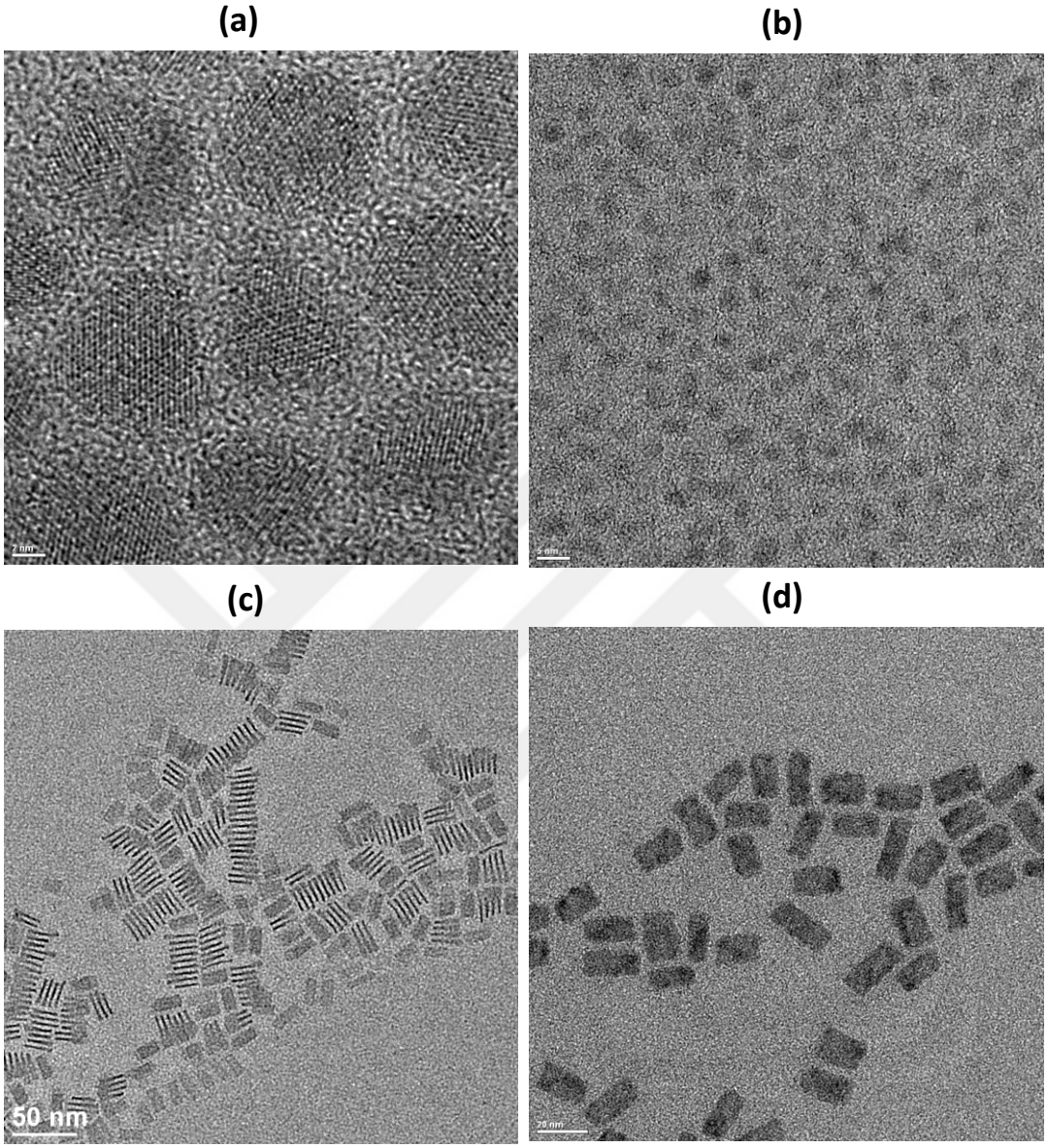

Figure 2.2.2.3. 1 HR-TEM images of our (a) CdSe/ZnS QDs, (b) InP/ZnS QDs, (c) 4ML thick CdSe NPLs, (d) CdSe/ZnS core/shell NPLs.

Chapter 3

3. High Performance QD Films for WLED and QLED Applications

3.1 Flexible CdSe/ZnS QD Films for WLED Application

The sub-chapter of this thesis is based on the publication "CdSe/ZnS quantum dot films for high performance flexible lighting and display applications," **Y. Altintas**, S. Genc, M. Y. Talpur, and E. Mutlugun, *Nanotechnology*, vol. 27, no. 29, p. 295604, 2016. Reprinted with permission from [26]. Copyright 2016 IOP Publishing.

3.1.1 Introduction

Colloidal quantum dots (QDs) have emerged in last few decades due to their promising optical and electronic properties, which make them one of the concrete building blocks of the next generation technology. They have been serving for optoelectronics regarding many applications i.e., in solar cells [28], [29], photodetectors [30], [31], and light emitting diodes [32], [33].

One of the key properties that the QDs offer is their tunable emission characteristic, which is due to the quantum confinement effect [34]. This has inspired the tremendous field of lighting and display applications based on the quantum dots. The quantum dots propose the engineering of the output white light and allow sharp characteristics of emitters, which can be hybridized to generate the desired light output. The next generation displays require wider color gamut to mimic the natural appearance on displays; and lighting applications require high color performance, both of which cannot be met by the conventionally used phosphor based emitters. According to a

recent report, the revenues based on quantum dot emitters are projected to exceed phosphor revenue by 2020 [35]. In alignment with that, quantum dots have started emerging for lighting and display applications to boost up their colorimetric performance.

Up to date there had been remarkable work on the systematic tuning of the white light parameters using colloidal quantum dots and their implementation for the display applications [36]–[39]. The applications for lighting applications using QDs are generally based on the utilization of the different sized quantum dots hybridized on blue light emitting diode platform to generate white light. However, this approach brings out the questions regarding the degradation of the emitters in direct contact with the underlying LED platforms. Due to their long-term thermal instability, the QDs cannot withstand the high temperature generated by the underlying current driven platform. This has led to research efforts on the implementation of the stand-alone sheets of QDs ready to be utilized as the remote phosphor agents. In this regard, the QD films can be employed at a distance from the excitation platform and can sustain their performance for longer time, also allowing for the surface emission rather than point like sources. However, the literature is lacking in means of the possible novel approaches towards achieving flexible high performance emitting platforms for lighting and displays. In addition to that, the stand-alone quantum dot films for high performance lighting and display applications, of which the requirements are different, have also not been shown to date. The lighting applications require high color rendering index, warm color temperature and high luminous efficacy of optical radiation, however the design of the emitters for the display applications require the enhancement of the color gamut that can enhance the viewer's color vision, allowing to provide more vivid colors at the display. In this study, we propose and demonstrate stand-alone sheets of CdSe/ZnS quantum dots of surface emitters which can be combined to generate white light in the 3-color mixing approach (blue LED, green and red emitting QDs) for display applications; and remarkable performance of white light emitting device, when a yellow emitting sheet of quantum dot is combined as the fourth emitter.

A versatile use of the prepared QD sheets allow for the application specific solution (lighting or display). In addition to this, our efforts have a significant contribution towards realization of flexible lighting platforms. The synthesis of up to

near unity quantum yield emitters, preparation of stand-alone sheets of QD emitters and the development of routes for the flexible lighting platforms have been performed. This has led to the achievement of blue LED excited films providing the best performing enhanced color gamut of 122.5% (as compared to the NTSC (National Television System Committee) color gamut) with those remote phosphor approach based sheets in the display application mode. A color rendering index of 88.6, luminous efficacy of optical radiation value of 290 lm/Wopt and warm color temperature of 2763 K has been achieved in the white light application mode. (the reported values are the optimal data for achieving warm white light, however CRI>90 levels and LER>300 are possible with cold white light corresponding to color temperature ca. 2000K using our flexible films) The performance values achieved are the best optimal achieved experimental values for the flexible remote phosphor films for lighting and display applications.

3.1.2 Result and Discussion

The CdSe/ZnS QDs have been synthesized using recipes explained in the previous section. By changing the composition of the colloidal quantum dots, the tunability in their optical properties have been achieved. In our experiments we have used the colloidal quantum dots with in solution peak emission wavelengths of 520, 562 and 626 nm along with their 34, 35, 26 nm full width half max. (FWHM) value, having photoluminescence quantum yield of 90%, 50% and 78%, respectively. Absorption and photoluminescence spectra were collected using UV-1800 Shimadzu and Cary Eclipse Fluorometer. Green, yellow and red emitting quantum dots' quantum efficiency has been measured by comparing with an organic dye using the methodology explained in the literature [40]. Green and yellow emitting dots have been compared with Rhodamine 6G in ethanol (QE: 95%) and red emitting dots with Sulphorhodamine 101 in ethanol (QE: 90%). Intersecting the absorption curves of the quantum dot and respected dye at the 460-490 nm range for the Rhodamine 6G and 510-560 nm range for Sulphorhodamine 101, around 0.1-0.2 absorbance value to prevent reabsorption, the photoluminescence measurements have been performed at the intersection wavelength and the spectral area have been compared to calculate the quantum efficiencies. The photoluminescence and absorption spectra of the quantum dots and the respected dyes are given in the Figure 2.2.1.2.1.

The emission properties of the synthesized quantum dots have been shown in Figure 3.1.2.1, along with the High-angle annular dark field transmission electron microscopy images in Figure 3.1.2.2, and high resolution transmission electron microscopy images in Figure 3.1.2.3 for the green, yellow and red emitting CdSe/ZnS quantum dots (using FEI - Model: Tecnai G2 F30 (with EDAX).

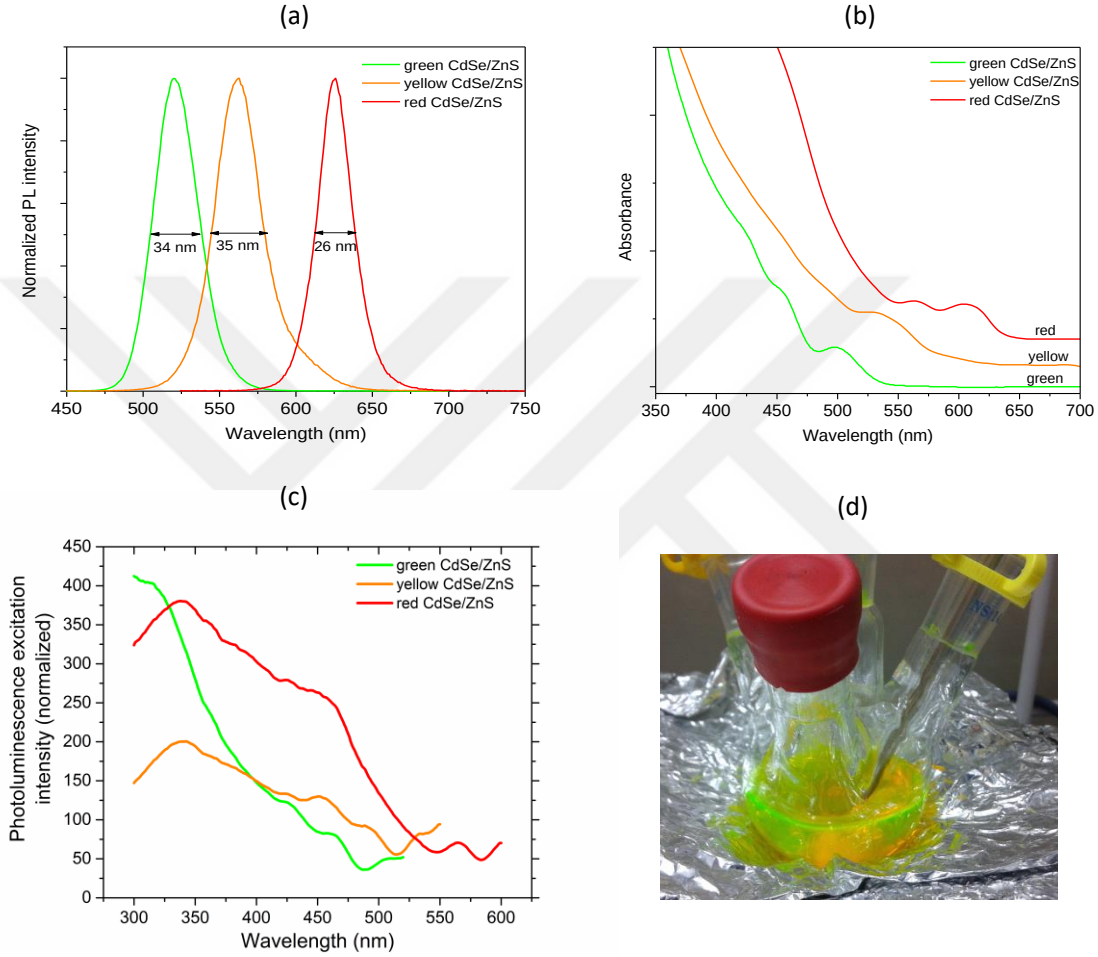

Figure 3.1.2. 1(a) The absorption, (b) emission, (c) photoluminescence excitation spectra of the synthesized CdSe/ZnS colloidal quantum dots, (d) photo of the green emitting quantum dots just after synthesis, under room light (without UV illumination). Reprinted with permission from [27]. Copyright 2016 IOP Publishing.

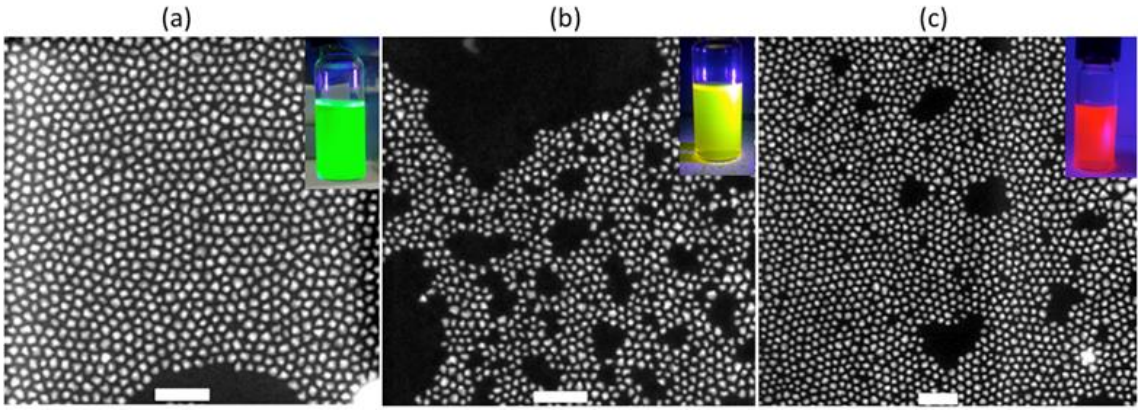

Figure 3.1.2. 2 HAADF-TEM images of the (a) green, (b) yellow and (c) red emitting CdSe/ZnS quantum dots. (The scale bar is 50 nm). Reprinted with permission from [27]. Copyright 2016 IOP Publishing.

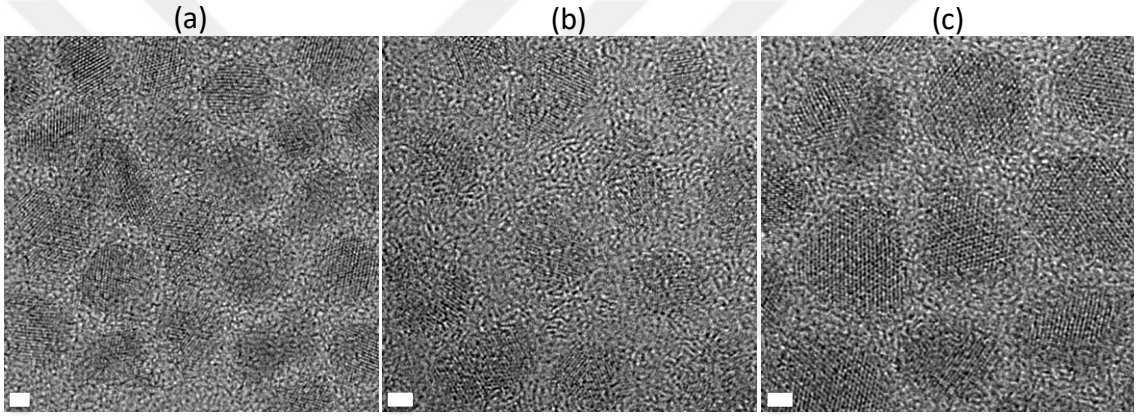

Figure 3.1.2. 3 HR-TEM images of the (a) green, (b) yellow, and (c) red emitting CdSe/ZnS quantum dots. (The scale bar is 2 nm). Reprinted with permission from [27]. Copyright 2016 IOP Publishing.

Regarding the generation of the white light for the display or lighting application, there is a definite need for the careful optimization of the emission peak wavelength and FWHM of the nano emitters. Whereas the narrow emitters provide an enhanced color gamut for the display applications, the optimization for the lighting requires satisfying the desired white coordinates along with high color performance (i.e., providing color temperature <3000K, color rendering index >90 and luminous efficacy of optical radiation >300 lm/Wopt). In that regards, although it is possible to achieve a larger color gamut using 3 color mixing approach with narrow emitters, for the lighting applications, the narrow green and red emitters itself are not sufficient to address the requirements of the high quality lighting. This then leads us to the use of the yellow emitters to fill the spectral content. In addition to that, the peak positions of the emission peaks and their spectral contribution to the output white light also effects the

performance figure of merits of the white light generated, which requires fine tuning of the optical properties of the nano emitters.

Table 3.1.2. 1 Energy dispersive X-ray spectroscopy data for the green, yellow and red emitting quantum dots. Reprinted with permission from [27]. Copyright 2016 IOP Publishing.

	Green QD			Yellow QD			Red QD		
Element	Weight (%)	Atomic (%)	Uncertainty (%)	Weight (%)	Atomic (%)	Uncertainty (%)	Weight (%)	Atomic (%)	Uncertainty (%)
S	20.51	36.71	0.48	14.63	29.80	0.51	17.95	40.25	0.71
Zn	54.13	47.49	1.03	38.60	38.54	0.98	9.39	10.32	0.36
Se	13.23	9.61	0.52	18.28	15.11	0.91	10.95	9.96	0.58
Cd	12.10	6.17	0.50	28.46	16.53	1.63	61.70	39.45	2.63

The energy disperse X-ray spectroscopy experiment results achieved from the STEM measurements have been given in Table 3.1.2.1, which presents the Cd, Se, Zn and S content for the different sized QDs. In accordance with the synthesis approach explained previously, the color tuning of the QDs have been achieved by modifying the Cd and Zn content of the synthesized particles. The average size of the quantum dots have been found to be 5.42, 4.60, 6.00 nm for green, yellow and red quantum dots, respectively, using dynamic light scattering technique (Malvern-Zeta Sizer).

The particles have further been investigated using X-ray diffraction (XRD) and X-ray photoelectron spectroscopy (XPS). Figure 3.1.2.4a demonstrates the XRD of the colloidal quantum dots taken by PANalytical: X'pert Pro MPD. The diffraction peaks of CdSe/ZnS quantum dots shift to (111), (220), (311) planes of the ZnS for green emitting QDs, which is in good agreement with the EDAX measurement analysis given in Table 3.1.2.1. Due to their more pronounced Cd content, the red emitting quantum dots' XRD spectra resembles the peaks of bulk CdSe. However in green emitting QDs where the Zn and S content is relatively much higher, we observe the XRD peaks are closer to the bulk values of ZnS crystal structure. Figure 3.1.2.4b depicts the XPS peak area percentage for Cd-3d, Se-3d, Zn-2p3 and S-2p performed by K-Alpha –X-ray photoelectron spectroscopy. In this comparison, the oxygen, carbon and nitrogen peaks have not been included in the analysis. The results have a similar pattern with the atomic percentages shown for EDAX analysis (Table 3.1.2.1). In agreement with our synthesis approach, the areal comparison of the XPS also depicts the compositional nature of the synthesized QDs.

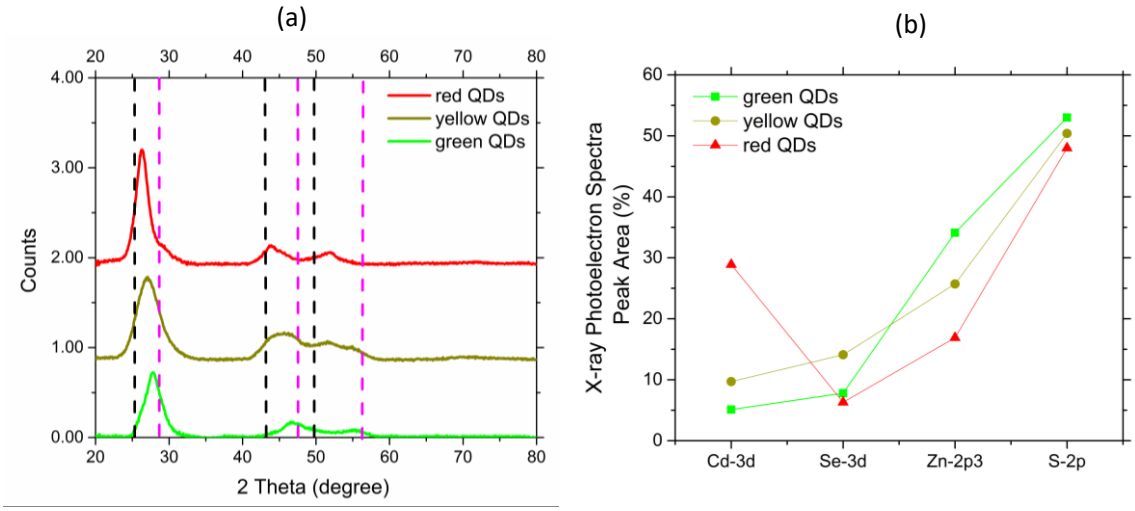

Figure 3.1.2. 4 a) X-ray diffraction (XRD) spectra of CdSe/ZnS core-shell QDs. Dashed black and purple lines represents the corresponding (111), (220) and (311) planes of zincblende CdSe and ZnS respectively. b) X-ray photoelectron spectra (XPS) peak area percentages of each QDs for Cd-3d, Se-3d, Zn-2p3 and S-2p peaks. Reprinted with permission from [27]. Copyright 2016 IOP Publishing.

As has been outlined in the introduction, the importance of the use of remote phosphor approach stems from the fact that the colloidal quantum dots cannot withstand high temperatures when in direct contact with the underlying LED platform. This effect has also been observed for the existing phosphor material used as the color converter. This has led to research efforts on the fabrication of free-standing color converting films that can allow for the versatile use of them and in that respect, very large areas of the quantum dot free-standing films have been shown previously [41]. The free-standing films of CdSe/ZnS QDs have been achieved by using polymethylmethacrylate (PMMA) matrix as the host polymer material. Figure 3.1.2.5 shows the QD films made up of green, yellow and red emitters that offer flexible, foldable solutions to be used for solid state lighting and display applications.

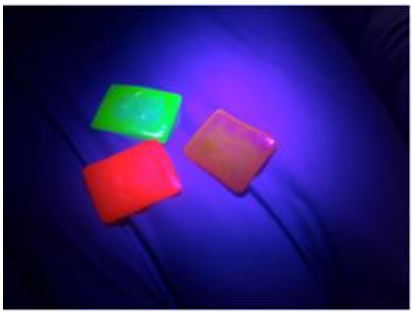

Figure 3.1.2. 5 Free-standing sheets of CdSe/ZnS quantum dots under UV light. Reprinted with permission from [27]. Copyright 2016 IOP Publishing.

In order to investigate the effect of the photoluminescence emission kinetics of the free standing films, we have performed time resolved photoluminescence measurements both for in solution and film samples, excited using a pulsed diode laser at 375nm (using PicoQuant Fluo Time 200). Regarding the emission kinetics, we have observed the lifetime decays of the in solution quantum dots get faster in their film form (Figure 3.1.2.6). This is due to the nonradiative channels being dominant in the film form of the colloidal quantum dots. As the nanocrystals are transferred to a film structure, we observe the amplitude averaged lifetime values (fit by 3-exponentials) of the green QDs decrease from 25.19 ns to 13.70 ns, the yellow QDs lifetime from 23.29 to 5.94 ns, red QDs 29.63 to 22.40 ns. The decrease in the average lifetime of the QDs are mostly attributed to the increase in the contribution of τ3, the fastest decay component, of which have been shown to increase from 13.45% to 34.12% for green, 20.06% to 72.07% for yellow and 5.15% to 32.11% for red emitting QDs. The details of the decay analysis have been given in Table 3.1.2.2. It is also worth noting here that the energy transfer (nonradiative) within the ensemble of quantum dots may also contribute to the change in QD lifetime.

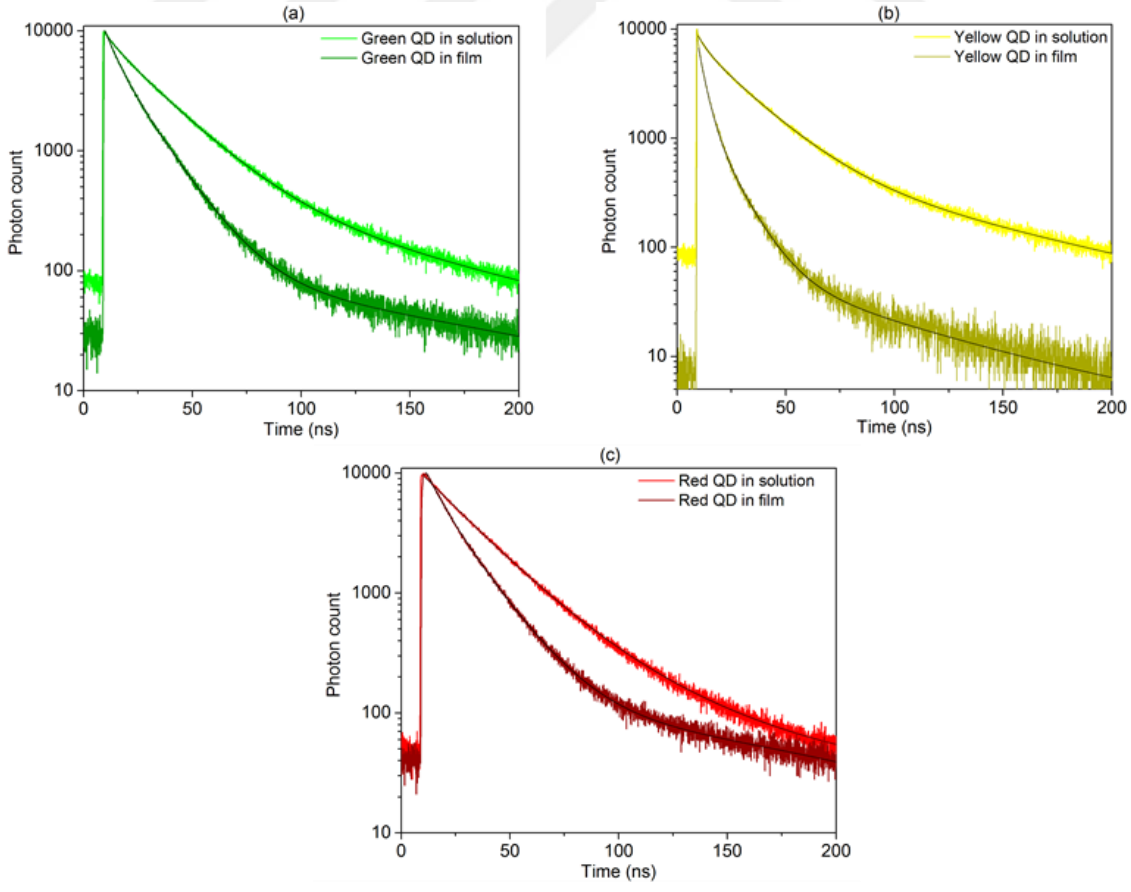

Figure 3.1.2. 6 (a) Time resolved photoluminescence decays of a) green, b) yellow, c) red emitting CdSe/ZnS colloidal quantum dots. Reprinted with permission from [27]. Copyright 2016 IOP Publishing.

Table 3.1.2. 2 Time resolved fluorescence fit for data for the green, yellow and red emitting quantum dots. Reprinted with permission from [27]. Copyright 2016 IOP Publishing.

	τ_1(ns)	τ_2 (ns)	τ_3 (ns)	$\tau_{amp\text{-}average}$ (ns)
Green QD in solution	113.56 (4.77 %)	23.379 (81.78%)	4.925 (13.45%)	25.19
Green QD in film	161.4 (1.18%)	15.435 (64.70%)	5.277 (34.12%)	13.70
Yellow QD in solution	100.2 (6.81%)	21.365 (73.13%)	4.202 (20.06%)	23.29
Yellow QD in film	67.91 (1.05%)	10.694 (26.88%)	3.266 (72.07%)	5.94
Red QD in solution	227.31 (3.16%)	24.136 (91.69%)	5.970 (5.15%)	29.63
Red QD in film	398.3 (2.20%)	17.165 (65.69%)	7.354 (32.11%)	22.40

Figure 3.1.2.7 shows the intensity of the output light generated when the green and red emitting films have been hybridized on the blue emitting LED platform. As the blue LED excitation source, we use 456 nm emitting commercially available InGaN LEDs, which is driven by using Keithley-2400 Sourcemeter. The spectral content of the output light is used to determine the performance of the output light generated.

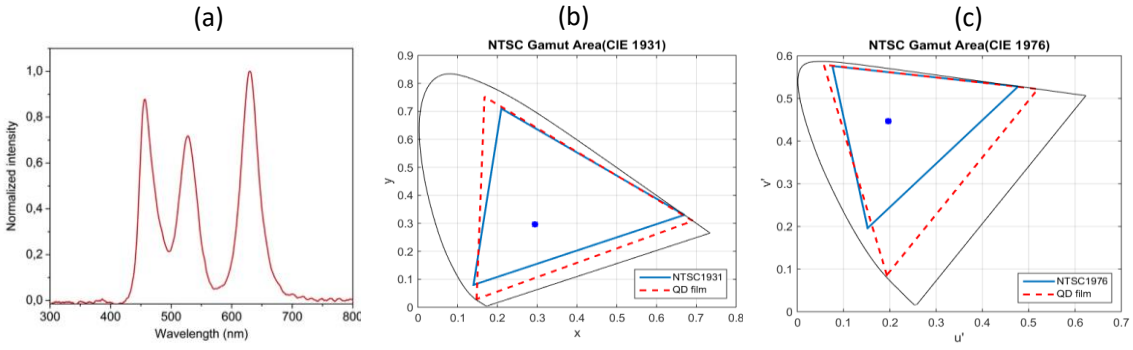

Figure 3.1.2. 7 a) The output light intensity as the red and the green emitters hybridized with blue LED. The color gamut enhancement in b) NTSC 1931, (c) in NTSC 1976 coordinates. Reprinted with permission from [27]. Copyright 2016 IOP Publishing.

For the three color mixing approach, the color coordinates have been determined as (x,y) (0.2939, 0.2958) along with the CRI value of 49.0, CCT of 8357 K and LER value of 239 lm/Wopt (Figure 3.1.2.7a). As also has been seen in the output light content of the three color mixing, there is a gap to deliver the high quality white light. Although the color mixing of the green and the red emitters allow for the generation of

the white light for a non-optimized performance for the lighting perspective, it provides wide color gamut as to enhance the color gamut to 122.5% (NTSC-1931) and to 148% (NTSC-1976). The corresponding color gamut enhancement visualization is given in Figure 7b and 7c for the CIE (International Commission on Illumination) 1931 and 1976 diagrams. In the calculation of the color gamut enhancement, the peak emission wavelengths and FWHM values read as (456 nm, 28 nm) for the blue LED, (527 nm, 37 nm) for the green and (629 nm, 33 nm) for the red emitters. The emission properties of the QDs are slightly different (red-shifted) in their film form as compared to the in solution optical emission properties due to environmental effects governing when the medium is changed.

In order to address for the high quality white light parameters, we have further incorporated an additional yellow emitting sheet to the existing green and red emissive layer and have performed the experiment for the spectral light output. The collected output light from the fiber (StellarNet Inc. Spectrometer with fiber optic output) is investigated to calculate the figures of merit of the white light generated.

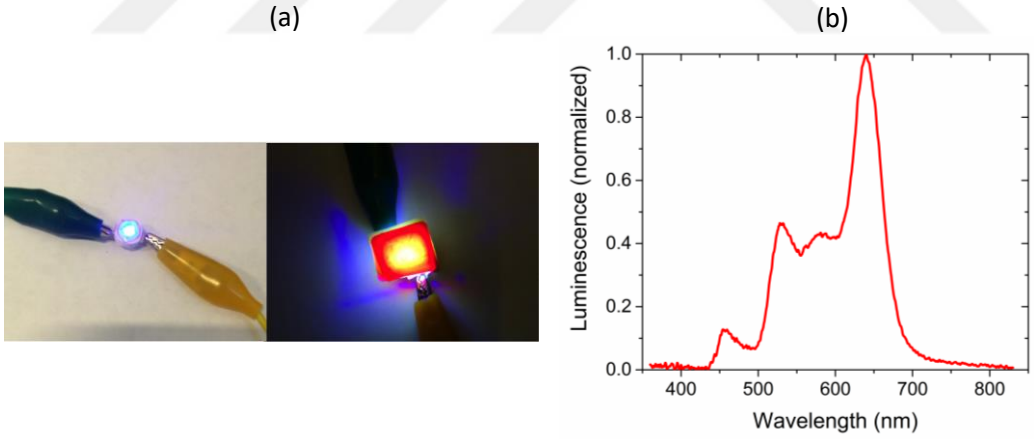

Figure 3.1.2. 8 (a) blue LED hybridized with and without CdSe/ZnS quantum dot flexible sheets (b) Spectral light output from the free-standing sheets of CdSe/ZnS quantum dots hybridized with blue LED. Reprinted with permission from [27]. Copyright 2016 IOP Publishing.

Using a four color mixing approach we have achieved the coordinates (x,y) (0.4709, 0.4393) along with the CRI value of 88.6, luminous efficacy of optical radiation value of 290 lm/Wopt and color temperature of 2763 K, which suits well with the warm white light spectrum. Figure 8a shows the blue LED hybridized with and without CdSe/ZnS quantum dot flexible sheets and Figure 8b shows the spectral output

of the color converter hybridized with the blue LED, with 2.65 V potential difference applied to the end terminals of the device.

It is worth noting here that a careful optimization on the color coordinates and the emission intensity of the individual emitters is necessary in order to optimize the light output, thus the color coordinates. It is evident from the literature that the red component has a great influence on the quality of the white light achieved [42]. In our experiment we have incorporated red emitting free-standing sheet in an orientation such that not only the blue emission but also the green and yellow emission is contributing to the excitation of the red emitting species. The quantum dot films have been used as separate sheets rather than mixing them in a film form as to prevent Förster type resonance energy transfer among them. The physical distance between different optical sheets, therefore is not effecting the overall output spectrum.

3.1.3 Summary

In conclusion, we have demonstrated the free-standing sheets of versatile CdSe/ZnS quantum dots as light generating agents to be implemented for lighting and display applications. Starting from the synthesis of high quality colloidal quantum dots with in solution peak emission wavelengths of 520, 562 and 626 nm along with their 34, 35, 26 nm full width half maximum (FWHM) value, having in solution photoluminescence quantum yield of 90%, 50% and 78%, respectively; we have extensively characterized QDs using transmission electron microscopy, X-ray diffraction, X-ray photoelectron spectroscopy, steady state and time resolved photoluminescence and dynamic light scattering methods. Further incorporating quantum dots to flexible polymeric films; we have utilized green and red emitters have provided an enhanced NTSC color gamut reaching 122.5%. The incorporation of the yellow emitting sheets has allowed us to target for high performance lighting allowing warm white light with high CRI level and color temperature around 2700 K. The realization of high efficiency and high performance quantum dot sheets for flexible lighting and display applications will pave the way for the sustainable growth of the lighting and displays industry.

3.1.4 Methods

Synthesis of CdSe/ZnS quantum dots and preparation of free-standing films

Cadmium oxide (CdO, 99.99%), zinc acetate (ZnAc, 99.99%), zinc acetate dihydrate ($ZnAc.2H_2O$, 99.999%), selenium (Se, 99.99% powder; 99.999% pellets), sulfur (S, 99.998% trace metals basis; 99.5% purum), oleic acid (OA, 99.99% technical grade), 1-dodecanethiol (DDT, 98%) 1-octadecene (1-ODE, 90% technical grade), trioctylphosphine (TOP, 90% technical grade), poly (methyl methacrylate (Mw: 996000)), anisole (99.0%), ethanol (EtOH, 99.8% absolute), acetone (Act, 99.5% absolute) and methanol (MeOH, absolute). All chemicals and reagents were purchased from Sigma-Aldrich. All chemicals were used without further purification.

3.1.4.1 Synthesis of green emitting QDs

The synthesis of green emitting CdSe/ZnS QDs have been performed by using modified method from the previous in the literature [43], [44]. Individual precursor concentrations, their ratio, vacuum level and stirring speed all contribute to the quality of the synthesized colloidal quantum dots and it is possible to drastically change the quality of the end product by small modifications to the recipe [45]. 0.3 mmol of CdO and 4 mmol of zinc acetate (ZnAc) reacted with 5 mL of oleic acid in a 50 mL three necked flask under vacuum at 150 ^{o}C for 30 min (vacuum level reaching ca. 10^{-3} Torr). Following, the solution was cooled to 50 ^{o}C and 15 mL of 1-ODE was loaded in a 50mLreaction flask equipped with a condenser and heated to 100 ^{o}C under vacuum. As the reaction system was maintained under Ar gas flow, the temperature was increased to 300 ^{o}C to obtain the transparent mixed solution of cadmium oleate and zinc oleate. Separately, a mixture of 0.3 mmol of Se and 3 mmol of S were dissolved in 2 mL of TOP at room temperature with overnight stirring at 800 rpm in the glove box. Afterwards, the clear solution of Se and S in TOP was obtained and rapidly injected into the reaction flask at 300 ^{o}C and the solution was kept for 10 min. for the completion of the green CdSe/ZnS QDs. Then, the mixture was cooled to room temperature to end the reaction. The synthesized QDs at room temperature are transferred to the cleaning process. A precipitation and re-dispersion method was used for the cleaning of QDs. The crude solution was precipitated in the presence of absolute acetone and methanol by centrifugation at 5000 rpm for 15 min and finally QDs have been re-dispersed in the hexane.

3.1.4.2 Synthesis of yellow emitting QDs

The reported methods were modified for the synthesis of yellow emitting CdSe/ZnS QDs [43], [44]. 0.8 mmol of CdO and 4 mmol of zinc acetate (ZnAc) reacted with 5mLof oleic acid in 50 mL reaction flask with condenser equipped system under vacuum at 150 ^{o}C for 30 min (vacuum level reaching ca. 10^{-3} Torr). The solution was cooled to 50 ^{o}C; 15 mL of 1-ODE was loaded in the reaction vessel and reaction was heated up to 100 ^{o}C under vacuum. Later, the reaction was heated to 300 ^{o}C under Ar gas flow to obtain the clear and homogenous mixed solution of cadmium oleate and zinc oleate. A mixture of 0.8 mmol of Se and 3 mmol of S were prepared by dissolving in 2 mL of TOP at room temperature with overnight stirring at 800 rpm in the glove box. The homogenous clear solution of Se and S in TOP was rapidly injected into the reaction system at 300 ^{o}C and the solution was kept at this temperature for 10 min in order to grow yellow emitting CdSe/ZnS QDs. The cleaning process is carried out in a same way as explained for the green emitting dots.

3.1.4.3 Synthesis of red emitting QDs

The reported procedures [43], [44], [46] were modified for the synthesis of red emitting CdSe/ZnS core shell QDs. 1 mmol of CdO and 1.68 mmol of zinc acetate dihydrate and 5mLoleic acid were added in a 50 mL three necked flask and heated to 140 ^{o}C under vacuum for 30 min (vacuum level reaching ca. 10^{-3} Torr). Then, the solution was cooled to 50 ^{o}C and 25 mL of 1-ODE was loaded to the mixture of cadmium oleate and zinc oleate in the reaction flask. The solution was firstly heated to 100 ^{o}C under vacuum and then the temperature was increased up to 300 ^{o}C under Ar gas flow. Separately, the injection solution is prepared as 1M TOP-Se (pellet) solution, prepared by stirring overnight at 800 rpm at 100 ^{o}C in the glove box. From the stock solution of TOP-Se, 0.2 mLof solution is rapidly injected in the reaction flask at the elevated temperature (300 ^{o}C) and kept for 80 seconds. Then, 0.3 mLof 1-DDT in 1mLof 1-ODE was injected into the system and the reaction continued for 20 min. Afterwards, 1 mL of TOP-S (2M) was slowly injected to the flask at 300 ^{o}C in 10 min. Subsequently, the solution was cooled to room temperature in order to produce the red emitting CdSe/ZnS QDs. The cleaning process is carried out in a same way as explained for the green emitting dots.

3.1.4.4 Preparation of the free-standing films

The PMMA has been prepared ca. 7.5% by dissolving in anisole. Upon preparation of the viscous solution, the cleaned QDs in fresh hexane has been mixed with the PMMA and left for rigorous stirring to provide well mixing of the QDs with polymeric solution. The solution is drop casted on the pre cleaned glass slides (pre washed with detergents using tap water, followed by cleaning with ethanol under sonication for 20 min.) and left for drying under controlled evaporation for overnight. The fully dried films have been peeled off from the glass surface and used as the flexible sheets of QDs ready for further experiments.

3.2 QLED Applications

QLED fabrication and characterizations have been carried out in collaboration with the Solid State Lighting group leader Dr. Ekaterina Nanen in Duisburg-Essen University by using Infra-structure of Nano Energie Technik Zentrum (NETZ). All solution processable device structure has been used for device fabrications. All layers except aluminum used as cathode electrode have been spin coated on the ITO coated glass.

Device fabrication has been started with the cleaning of the ITO glass by using acetone and ethanol with ultrasonication, then used 10 minute ozone cleaning. Filtered Pedot-PSS has been spin coated at 2000 rpm for 1 min, then baked at 150 ^{o}C for 20 min. 50 µL of Poly-TPD as hole transport layer (HTL) has been spin-coated at 2000 rpm for 1 min, then baked at 150 ^{o}C for 30 min in glovebox. 2-times cleaned and filtered green and red QDs prepared the concentration of 28 mg/mL and 13 mg/mL, respectively, have been spin-coated by using two spin parameters first 5 second 100 rpm and then 2000 rpm with 2000 rpm acceleration for 1 min. Then It has been baked in glovebox at 120 ^{o}C for 30 min. ZnO nanoparticles have been used as electron transport layer (ETL) and spin-coated at 2000 rpm for 1 min and then baked at 120 ^{o}C for 30 min in glovebox. To finish device fabrication stage, 150 nm of thick layer of aluminum has been thermally evaporated on ZnO coated layer.

Device characterizations have been done by using Keithley 2601 as source-meter, calibrated Si-photodiode (818-UV from Newport) operated by specially designed

LabVIEW software program, and device characterizations have been carried out under inert gas atmosphere. CS-2000A (Konica Minolta) spectroradiometer has been used to collect electroluminescence spectra of the QLEDs.

Red and green emitting QLED device performance has been presented with External quantum efficiency (EQE), luminance (Lum) and I-V (current-voltage) graphs in Figure 3.2.1 and Figure 3.2.2.

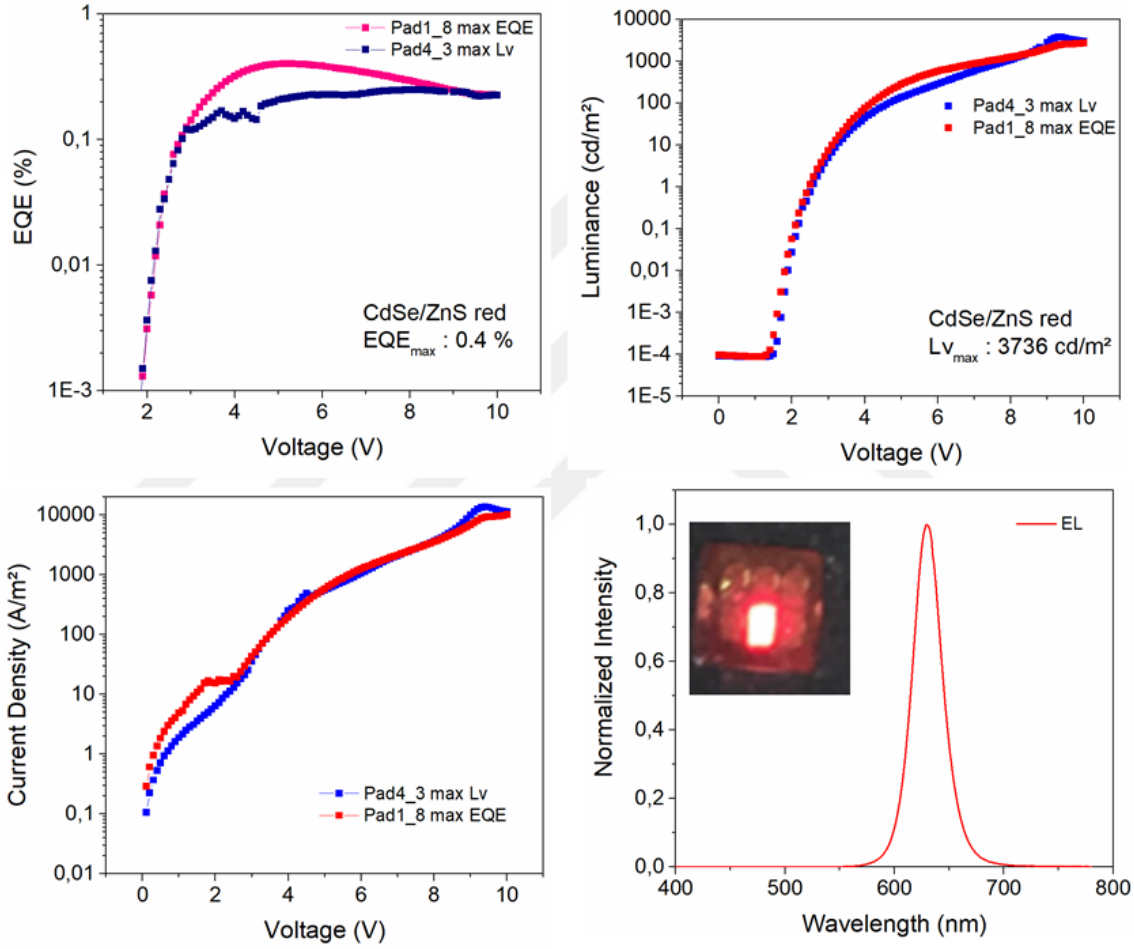

Figure 3.2. 1 All solution processed red emitting CdSe/ZnS QLED device performance. The inset photo in EL spectrum shows illumination of the CdSe/ZnS red emitting QLED at 7 V operation.

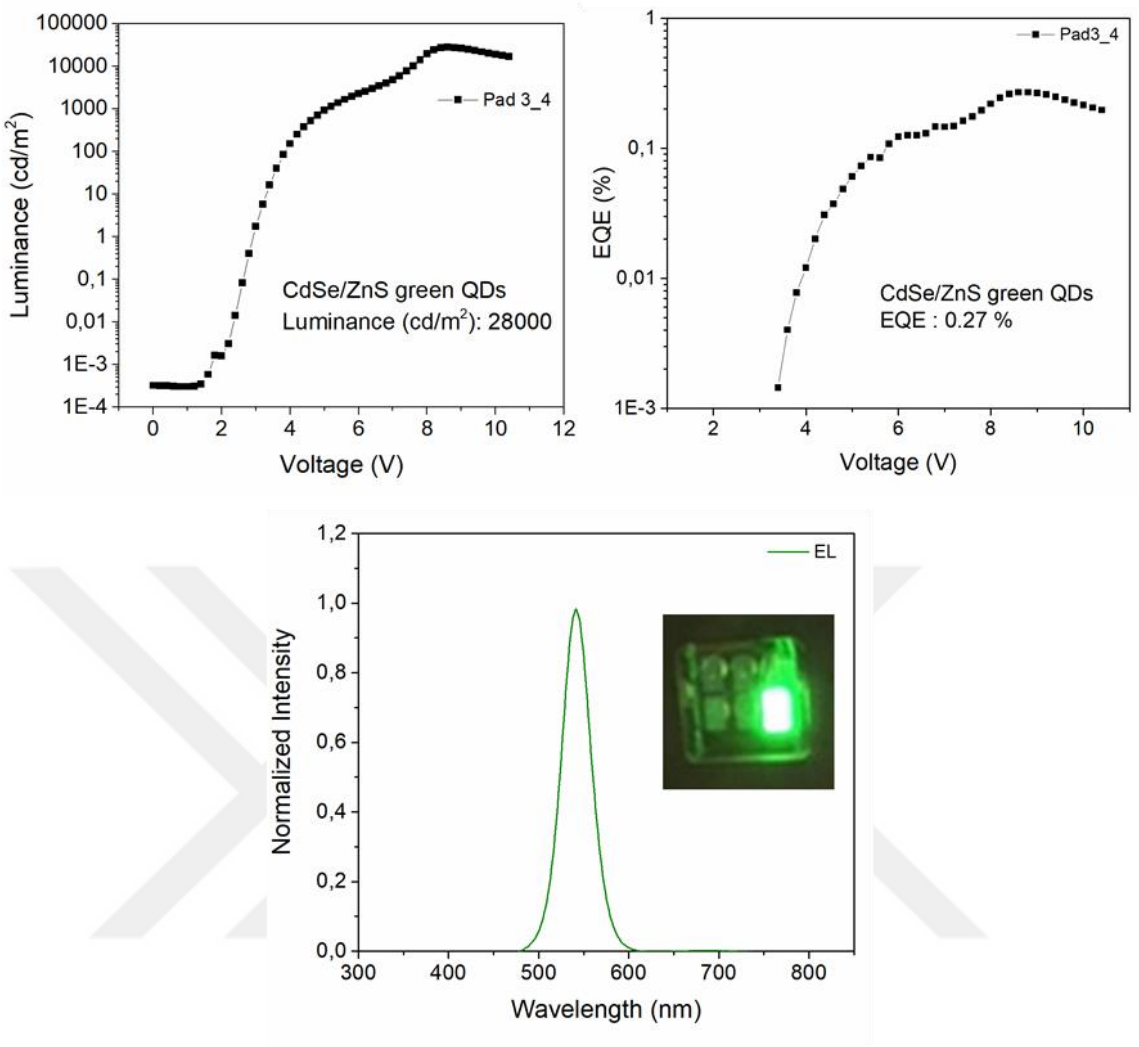

Figure 3.2. 2 All solution processed highly luminescent green emitting CdSe/ZnS QLED device performance. The inset photo in EL spectrum shows illumination of the green emitting CdSe/ZnS QLED at 9 V operation.

Device structure of QLEDs can be summarized as;

Red QLED: ITO/Pedot:PSS/PolyTPD/13mg/mL QD (2x cleaned in hexane)/ZnO /Al

Green QLED: ITO/Pedot:PSS/PolyTPD/28mg/mL QD(2x cleaned in hexane)/ZnO/Al

Maximum EQE and brightness values for green and red emitting CdSe/ZnS QLEDs have been obtained as 0.27 % (EQE), 28000 cd/m^2 (Lum) and 0.4 % (EQE), 3736 cd/m^2 (Lum), respectively. As understood from the presented EL graph of the green and red QLED, pure green and red color emitting QLEDs have been fabricated by using CdSe/ZnS QDs with all solution processed device structure.

Device performance of the red emitting CdSe/ZnS QLED has been improved with the optimization of the layers and concentration of the QDs. Device characterizations optimized red emitting QLED have been given in Figure 3.2.3.

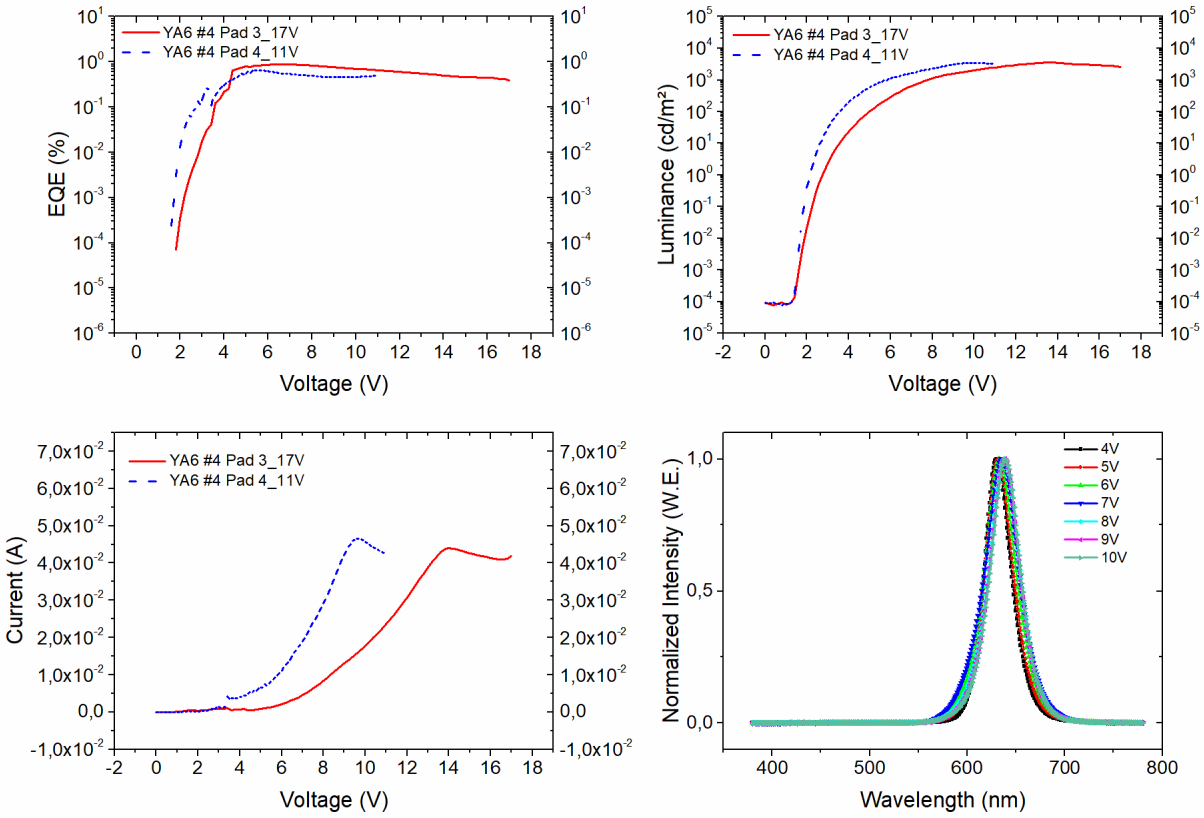

Figure 3.2. 3 Device performance of the red emitting QLED have been presented after optimization of the layers and QD concentration.

The red emitting device has been given as;

ITO/Pedot:PSS/PolyTPD/ 20 mg/mL red CdSe-ZnS QD (2x cleaned in hexane)/ZnO/Al

EQE of the red emitting QLED have been enhanced from 0.4% to 1% by optimizing the concentration of the CdSe/ZnS QDs and film quality of the layers.

To enhance device performance of green emitting QLED, PVK as hole transport layer has been used in the device structure with 20 mg/mL concentration of the QDs. EQE value of the device have enhanced from 0.28% to 1% by changing of the HTL of the device. Owing to the lower hole mobility (100 times) of PVK as compare to the poly-TPD, luminance value of the device have decreased from 28000 cd/m^2 to 1000

cd/m^2. Device characterization of the PVK containing QLED has been presented in Figure 3.2.4.

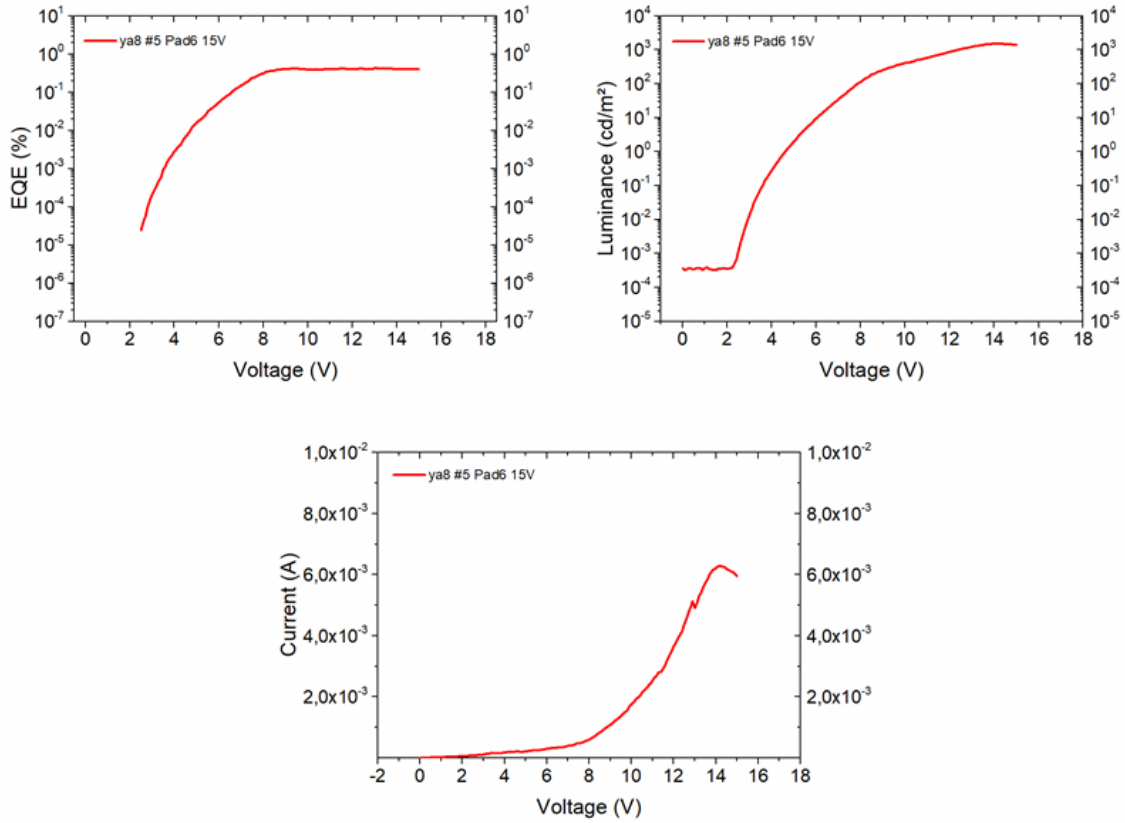

Figure 3.2. 4 Device characterization of the PVK containing QLED.

The ability of the QLED device production have been gained in the group of Dr. Ekaterina Nannen under the supervision of Gerd Bacher and many device fabrication trials have been realized within the three months together with learning and understanding. Both EQE and luminance value of the device can be enhanced optimized device structures.

Chapter 4

4. Highly Efficient Cd-free QDs synthesis

The chapter of this thesis is based on the publication "Highly Efficient Cd-Free Alloyed Core/Shell Quantum Dots with Optimized Precursor Concentrations," **Y. Altıntas**, M. Y. Talpur, M. Ünlü, and E. Mutlugün, *J. Phys. Chem. C*, vol. 120, no. 14, pp. 7885–7892, 2016. Reprinted with permission from [45]. Copyright 2016 American Chemical Society.

4.1 Introduction

The colloidal quantum dots (QD) have been on demand for few decades owing to their applications in light emitting diodes,[37], [41], [47]–[49] solar cells, [50], [51] biological fluorescent probes, imaging, [52]–[54] sensors [55]–[57]. Recently, as the environmental concerns have been raised, the efforts on QDs have also been focused on the synthesis of group III-V, namely InP based QDs. Their tunable emission spectra from blue to red without having intrinsic toxicity compared to the CdSe based ones put them forward as promising candidates for optoelectronics [58]–[60]. Thanks to the quantum confinement effect, semiconductor QDs possesses size dependent optical properties when the size of the nanocrystals is smaller than the exciton Bohr radius. However, InP based quantum dots show poor optical properties due to non-radiative recombination at defect zones and surface traps as compared to Cd based ones [61]. A wide band gap semiconductor ZnS, has become one of the unique shell used for coating of a diversity of group II-VI as well as the III-V QDs [62]–[64]. The wider band gap shell material is being employed as a physical barrier against oxidation, prevents the core from the surrounding medium effects and provide better quantum confinement [13].

In previous reports, several studies demonstrated InP/ZnS QDs with photoluminescence quantum efficiency (QE) of 38% and 68% [65], [66]. Recently, Yang et. al. reported the synthesis of InP/ZnS QDs with tunable emission and obtained the QE as high as 63% with full width at half maximum value (FWHM) of 76 nm [67]. As a multi-shell process of InP based QDs, the authors reported PL QE of 85% in InP/GaP/ZnS and 50-70% in InP/ZnSe/ZnS, respectively [68], [69]. In addition to those studies, size-tunable synthesis of InP QDs with ZnS and ZnSe has been published by Tessier et. al. which showed an impact of indium halide and zinc halide groups on InP QDs possessing the maximum QE and FWHM within the range of 20-60% and 46-63 nm respectively [70].

Although many reports on InP based alloyed or core shell QDs, namely InPZnS, InZnP, InP/ZnS, InP/GaP/ZnS have been investigated till date giving an optimized recipe by the control of a specific precursor/ligand, there is no study till date focusing on the origin of the demonstrated efficiencies with the comprehensive investigation of the precursors (ratio), as well as the effect of the shelling of the alloyed core structure revealing the emission kinetics. In this study we reveal the importance of the alloying core in the starting phase as compared with the conventional core-shell approach. Therefore, for the first time, this work demonstrates an in depth analysis for the optimal route towards achieving highly efficient InPZnS alloy/ZnS shell QDs, tuning the emission wavelength to the desired extent by modifying the precursor ratio and experimental conditions, which is very critical for the applications requiring a targeted peak emission wavelength. In this regard, we demonstrate the synthesis of InPZnS alloy/ZnS shell to obtain high QE and narrow FWHM targeting different peak emission wavelengths and present a detailed investigation through individual control of optimization of precursor concentration and their ratio, along with the discussion of the emission kinetics due to the shelling mechanism.

It is quite well known that the concentration of precursors and ligands are directly related with the nucleation and growth process which are very critical for the optimization of the synthesis conditions [71]. In our protocol, we have systematically varied the precursor concentrations and ratio in order to control the critical position of nucleation and growth process to achieve color tunability and high efficiency. Our recipe for the synthesis of alloyed InPZnS is a modifed recipe from the literature based

on the formation of the indium myristate (In-MA), followed by the addition of Zn and S precursors and injection of the phosphor precursor at high temperature [66]. Unless otherwise stated, the core QDs have been further coated with ZnS shell using a modified recipe in the literature [72]. The details of the synthesis methods used have been outlined in the experimental session. In this respect, in this work we have varied the concentration of the fatty acid ligand, indium, phosphor and the sulfur precursor to achieve color tunability and high efficiency along with the shelling of the alloyed core structure with the aid of the control on the nonraditaive emission channels.

4.2 Result and Discussion

Figure 4.2.1 shows the absorbance and emission spectra of the quantum dots using different ratio of (indium/myristic acid) In/MA. In this process, three different samples were analyzed changing the amount of MA at 0.2, 0.35 and 0.5 mmol while keeping the In amount the same at 0.1 mmol. It is shown that increasing the concentration of MA shifted the excitonic peak and the emission peak to a longer wavelength, allowing for the growth of the core material to a larger size. Varying the In:MA from 1:2 to 1:3.5 and 1:5, the peak emission wavelength has been found to be 483, 490, 515 nm with FWHM of 46, 45, 54 nm and QE of 30%, 52%, 46%. Decreasing the relative ratio of the In in the starting nucleation phase is believed to result in causing more surface defects, which shows wider FWHM value which is also similar to what has been observed in the previous literature [62]. The tunability in the peak emission within the range of 30 nm can be achieved by the systematic tuning of the In:MA ratio. The optimal ratio of In:MA was found to be optimal around 1:3-1:3.5 to possess high quantum efficiency. Extending the In:MA ratio further to less than 1:2 or more than 1:5 results in decreased photoluminescence emission of the quantum dots.

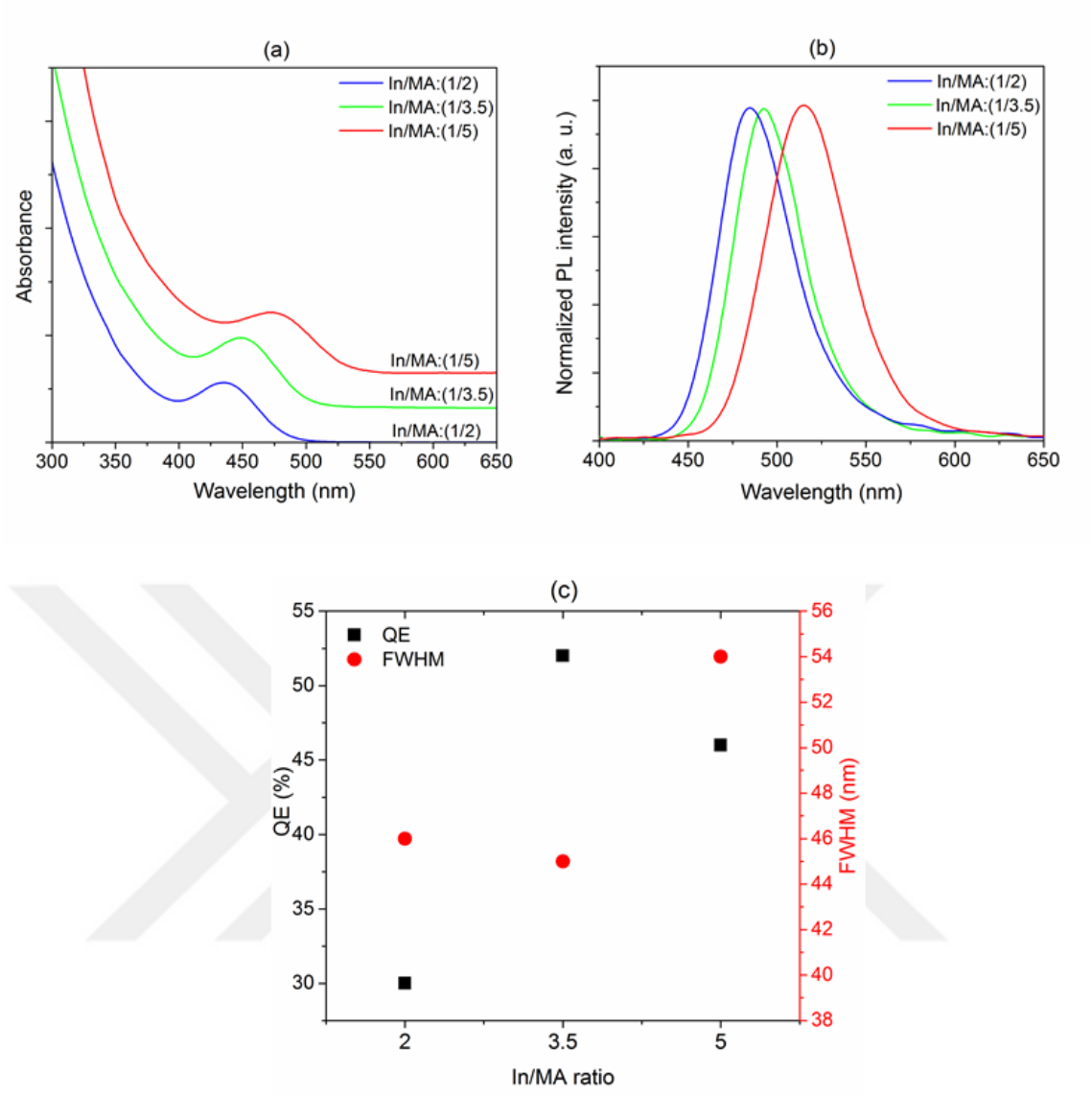

Figure 4.2. 1 (a) Absorption spectrum (b) photoluminescence spectrum (c) quantum efficiency and full width half max. values of InPZnS alloy/ZnS shell QDs with different concentration of fatty myristic acid ligand. (In:P:Zn:S alloy= 1:1:1:1, Zn:S shell= 2:4) (the amount of In is 0.1 mmol). Reprinted with permission from [45]. Copyright 2016 American Chemical Society.

In order to investigate the effect of the P-precursor, we have varied the ratio of the In to P-precursor ratio for the synthesis. Figure 4.2.2 shows the absorbance and PL emission peak of analyzed samples varying the concentration of P-precursor from 0.125, 0.091 and 0.071 mmol by using 0.1 mmol In, and therefore the ratio of In/P is varied as 0.8, 1.1 and 1.4, respectively. In this case the amount of In:MA is kept constant at 1:3, however In/P ratio is varied. It has been shown that reducing the concentration of P-precursor, tristrimethylsilyl phosphine ($(TMS)_3P$) causes red shifting of PL emission peak and increasing the quantum yield from 41%, 50% to 61% (Figure 4.2.2c) with FWHM of 47, 46 and 49 nm, respectively; corresponding to a sufficiently

narrow size distribution for such material systems. As the ratio of In/P is decreased, we observed drop in the QE due to relatively less In-rich surface which results in nonradiative recombination processes to occur.

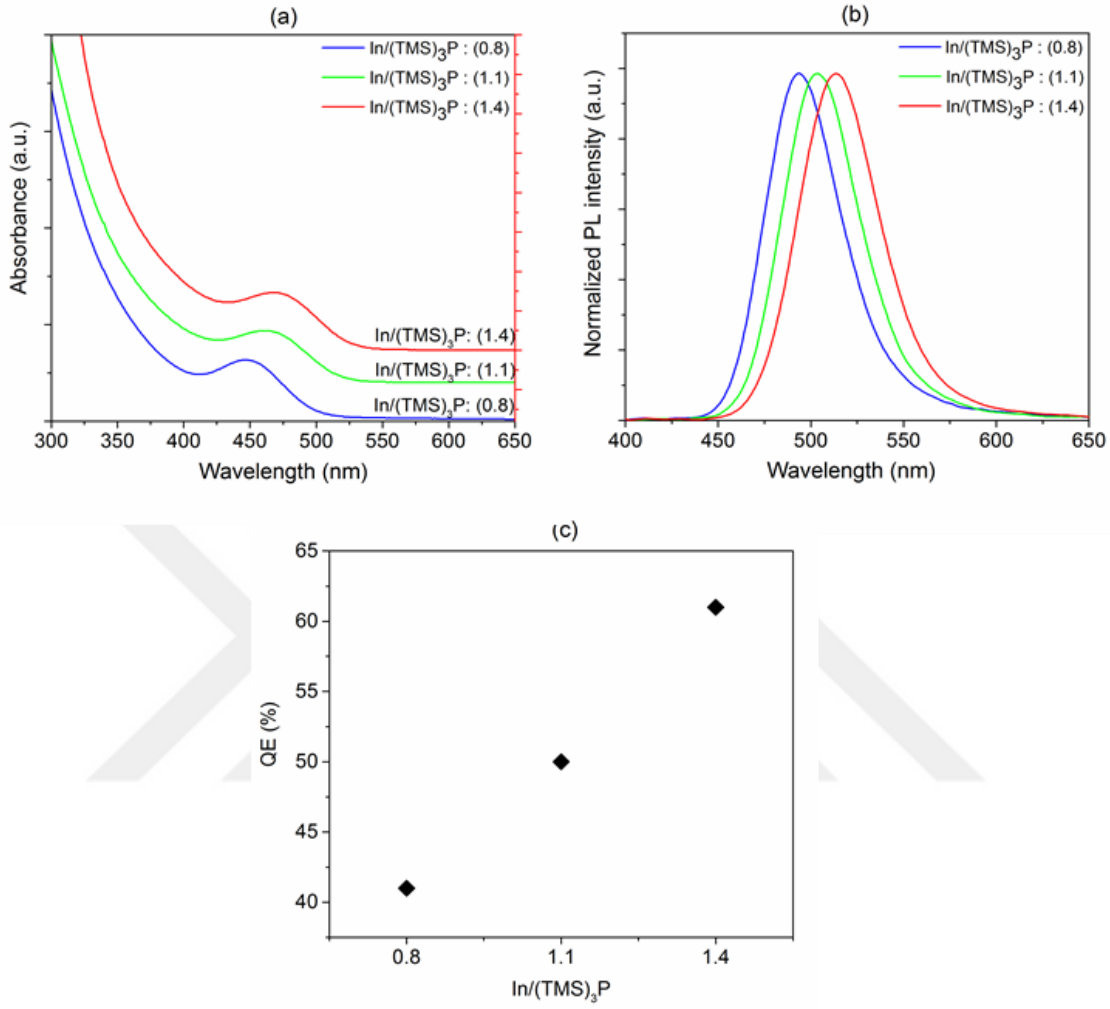

Figure 4.2. 2 (a) Absorption spectrum, (b) photoluminescence spectrum (c) quantum efficiency of InPZnS alloy/ZnS shell QDs using different concentration of (TMS)3P (In:MA:Zn:S alloy= 1:3:1:1, Zn:S shell= 2:4) (the amount of In is 0.1 mmol). Reprinted with permission from [45]. Copyright 2016 American Chemical Society.

The investigation of the ratio of the In:MA and In:(TMS)3P in the synthesis has given us the indication regarding the fine tuning the peak emission wavelength within an acceptable range. However for a full color tunability of the peak emission wavelength we have found out that the S-precursor source dodecanethiol (DDT) plays a critical role in determining the size of the core alloyed structure. When concentration of DDT was tuned from 0.1 to 0.01 mmol, keeping other precursor concentration constant,

the PL emission peak broadens and shifts to longer wavelength region from 506, 522, 548 and 575 nm with PL QE of 64, 78, 78 and 65% with FWHM at 48, 54, 67 and 94 nm, respectively (Figure 4.2.3). The inconsistency in the QE trend for the particles emitting at longer wavelength stems from the further broadening of the FWHM value.

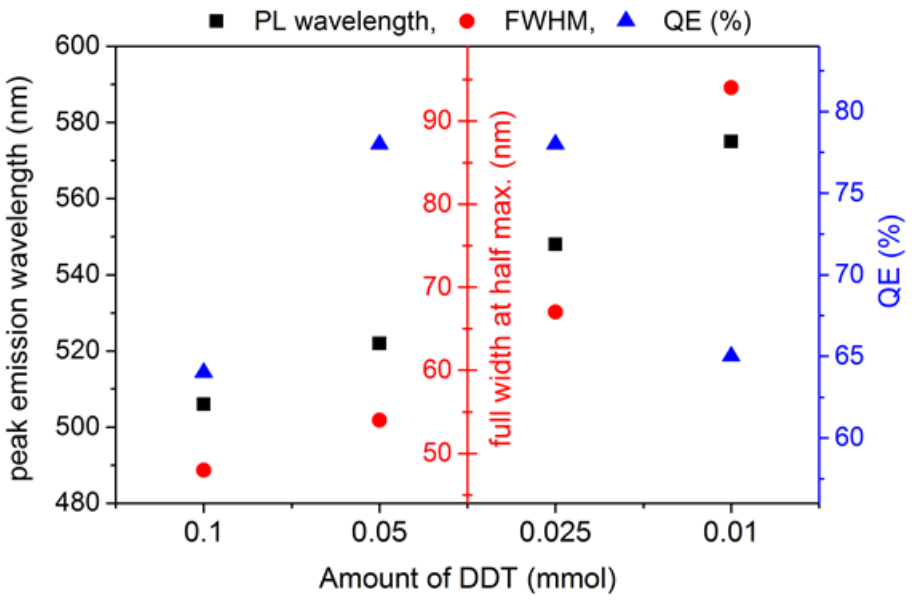

Figure 4.2. 3 Peak emission wavelength, full width at half maximum and quantum efficiency of the InPZnS alloy/ZnS shell QDs with different concentration of DDT (In:MA:P:Zn alloy= 1:4.3:1:1/Zn:S shell= 2:4) (the amount of In is 0.1 mmol). Reprinted with permission from [45]. Copyright 2016 American Chemical Society.

It is also worth noting here that the zinc source, zinc stearate purity has a huge impact on the quality of the QDs synthesized. As the zinc stearate purity is changed from technical grade keeping the other parameters the same, we have seen up to %50 increase in the quantum efficiency of the nanocrystals synthesized. In this regard, using purum grade zinc stearate with the optimized concentration of the precursors involved, we revealed a robust synthesis of highly efficient InPZnS/ZnS alloy/shell QDs by varying synthesis parameters in a single shell process. In this perspective, using the optimal concentrations stemming from the methodological investigation of the ratio of the precursors involved and further shelling process, we obtained the maximum QE in our synthesis approach as 62% (blue), 75% (cyan) and 78% (green) with narrow FWHM values of 46, 47 and 45 nm in InPZnS/ZnS alloy/shell and achieved the full visible spectrum (from blue to red emissions) by single shelling process (Table 4.2.1). Table 4.2.1 shows the emission peak wavelength, QE and FWHM of the synthesized

QDs and Figure 4.2.4 presents the overall absorbance (Figure 4.4.4a), photoluminescence (Figure 4b), FWHM and QE (Figure 4.2.4c) of the synthesized nanocrystals along with their photo under UV light. Here one should also note the broadening of the photoluminescence and decrease in the QE of the particles as the emission peak shifts towards red. The confinement of the electron-hole wave function into the core is a serious issue in the larger size particles as compared to the smaller sized ones, which is believed to be due to poor surface passivation, which becomes remarkably disastrous, as the particle size gets larger.

Table 4.2. 1 PL QE and FWHM as a function of precursors amounts and the ratio from shorter . (blue) to longer (red) emission wavelength. Reprinted with permission from [45]. Copyright 2016 American Chemical Society.

Emission-peak (nm)	484	499	514	545	574	586	612	621
[ǂ]QE	62	75	78	77	65	46	33	28
[#]FWHM	46	47	45	67	94	85	90	94

[ǂ]QE= Quantum efficieny; [#]FWHM= Full width half maximum

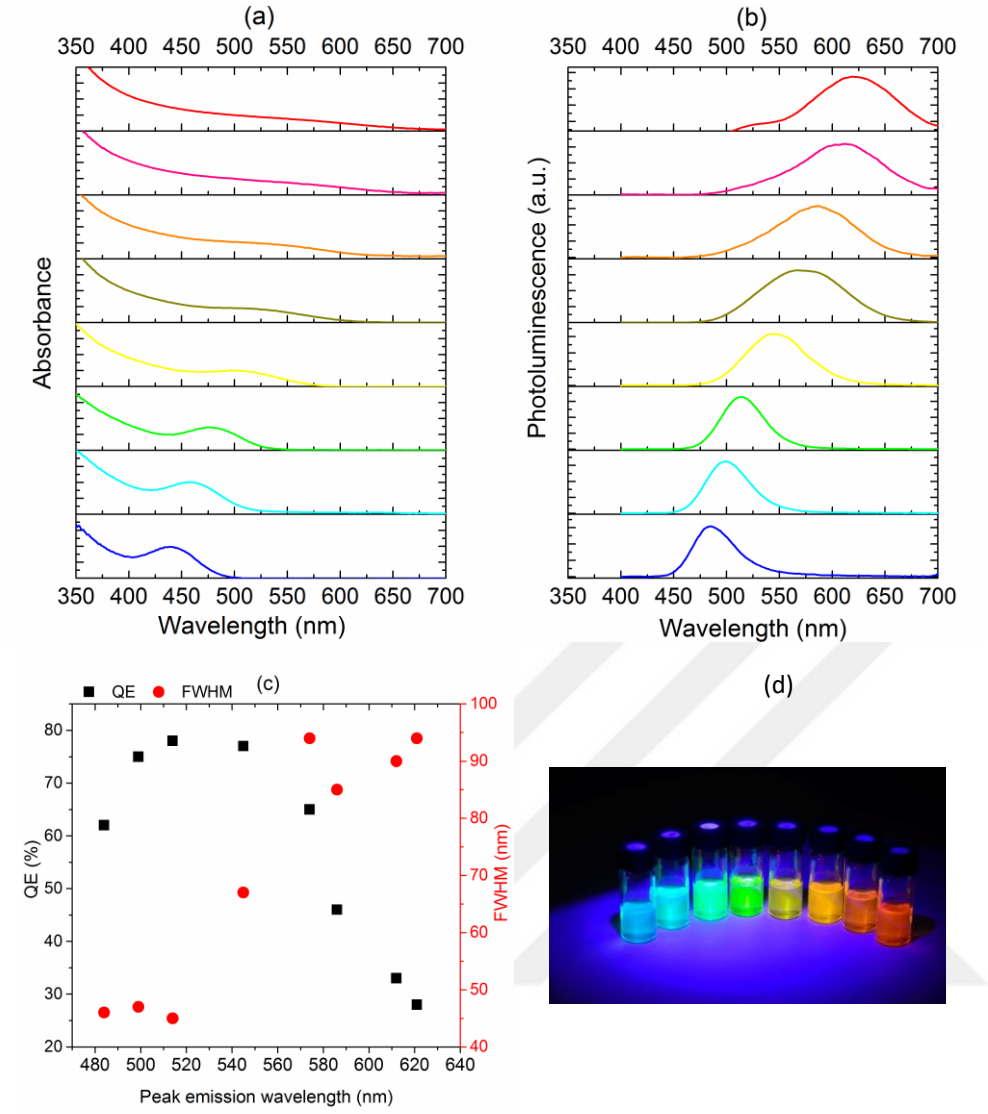

Figure 4.2. 4 (a) The absorbance spectra, (b) photoluminescence spectra, (c) quantum efficiency and FWHM of QDs synthesized, (d) the photo of the QDs investigated under UV illumination (top). Reprinted with permission from [45]. Copyright 2016 American Chemical Society.

We have carried out Fourier Transform Infrared Spectroscopy (FTIR) measurements of the synthesized InPZnS alloy/ZnS shell QDs. Figure 4.2.5a shows the FTIR spectrum for the highly efficient 514 nm emitting InPZnS alloy/ZnS. The band at 1463 cm^{-1} is attributed to methylene (CH_2) bending vibration of long aliphatic chain [71]. The observed bands at 1383 and 1544 cm^{-1}, are originated from asymmetric and symmetric stretching vibrations of carboxylate anions [71]. The band at 1544 cm^{-1} is consistent with the literature, representing the Zinc existence for QDs [71]. The bands at 2850 and 2920 cm^{-1} were illustrated by C-H stretching of methyl ($-CH_3$) and methylene ($-CH_2$) groups of alkyl chain of aliphatic groups [73]. The band at 910 cm^{-1} is

corresponds to vinyl group =C-H [71]. The band at 720 cm^{-1} is related with $–CH_2$ asymmetric rocking mode.

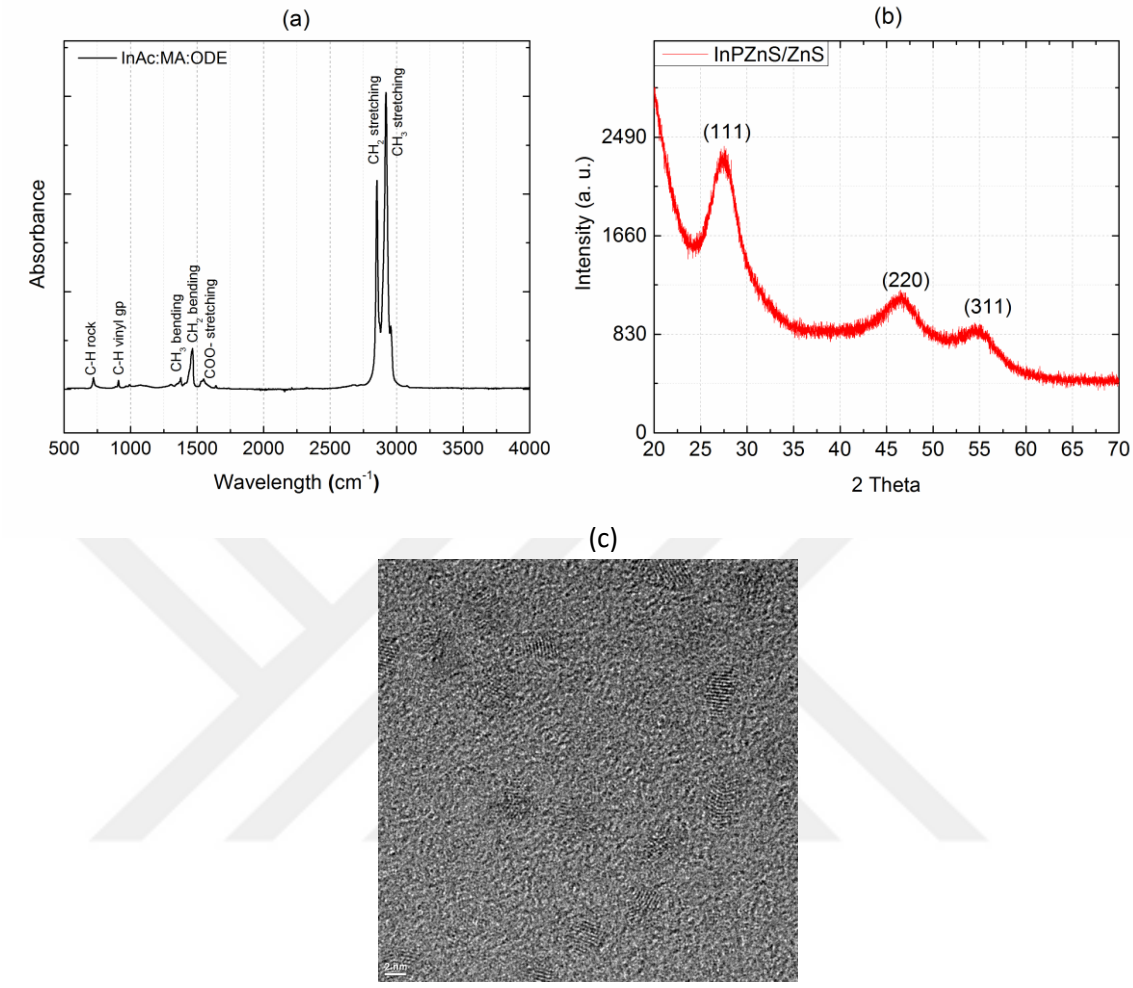

Figure 4.2. 5 (a) FTIR spectra of InPZnS alloy/ZnS shell with Indium Acetate (InAc):Myristic Acid (MA) synthesized in octadecence (ODE). (b) XRD spectra of InPZnS alloy/ZnS shell QDs (c) TEM images of InPZnS alloy/ZnS shell QDs. (the scale bar is 2 nm). Reprinted with permission from [45]. Copyright 2016 American Chemical Society.

The crystalline quality of the same InPZnS alloy/ZnS shell QDs were examined by X-ray Diffraction (XRD). Figure 4.2.5b shows XRD patterns of synthesized QDs, indicating the well-defined peaks at (111), (220) and (311) that assigned to cubic zinc blende structure [66], [72]. Pronounced peaks in InPZnS alloy/ZnS shell indicate the crystal quality attained by having the ZnS shell structures. Figure 4.2.5c presents the transmission electron microscope (TEM) images of alloy/shell InPZnS alloy/ZnS shell QDs (514 nm emitting). The average size of alloy/shell was found to be c.a. 3.5 nm.

In order to understand the origin of the shelling effect of the alloyed core material, we have investigated the step wise steady state and time resolved emission characteristics of the synthesized particles after the alloyed core growth, and during the shell growth process, namely after the Zn precursor addition, sulfur precursor-dodecanethiol addition, and at the final cool down stage. For this set of characterizations, we have reperformed the experiment for the 514 nm emitting quantum dots (see Figure 4.2.4b green emitting dots). The results reveal that we have enhanced the photoluminescence quantum yield systematically, up-to 7 folds, when we systematically grow shell material on the existing core. (Figure 4.2.6c) The quantum efficiency have been found to increase stepwise, from 10% to 39% as the Zinc precursor has been introduced and further up to 73%, when the shelling have been completed with S precursor addition. The first Zn precursor is believed to start the shelling process with the overcoating of the alloyed InPZnS alloyed core and the outermost sulfur precursor completes the shelling process. The quantum efficiency achieved here (%73) is slightly less than that of observed as compared to the previous experiment performed (78%) (see Table 4.2.1 and Table 4.2.2). This is due to the fact that the alequots taken before and during different shelling stages influence the kinetics of the quantum dot growth mechanism. In order to reveal the suppression of the nonradiative decay channels, we have investigated the time resolved photoluminescence decays of the QDs before and during the shelling process. Figure 4.2.6d demonstrates the photoluminescence decay curves of the QDs at different stages of the shelling process along with the Table 4.2.3, which presents the amplitude and decay time from the exponential fits of the decays in Figure 4.2.6d. The amplitude average lifetimes increase from 20.3 to 40.2 ns as the Zn is introduced as the shell material, and further to 54.4 ns with the completion of the shelling. The increase in the lifetime of the alloyed QDs after the shelling is due to the suppression of the nonradiative decay channels. This is also clearly observed when the amplitude and decay lifetimes are investigated. As the Table 4.2.3 depicts, the amplitude of the fastest decay component $\tau 3$ contributes to 53% of the amplitude weighted lifetime of the alloyed core, however as the shelling takes place, the fractional amplitude of the $\tau 3$ accounts to 29% of the overall lifetime with the Zn addition, and to %11 with the S addition, completing the shelling process. In agreement with the steady state emission characteristics, the overall suppression of the $\tau 3$ lifetime fraction is attributed to the suppression of the nonradiative decay channels, giving rise to the enhanced photoluminescence quantum yield.

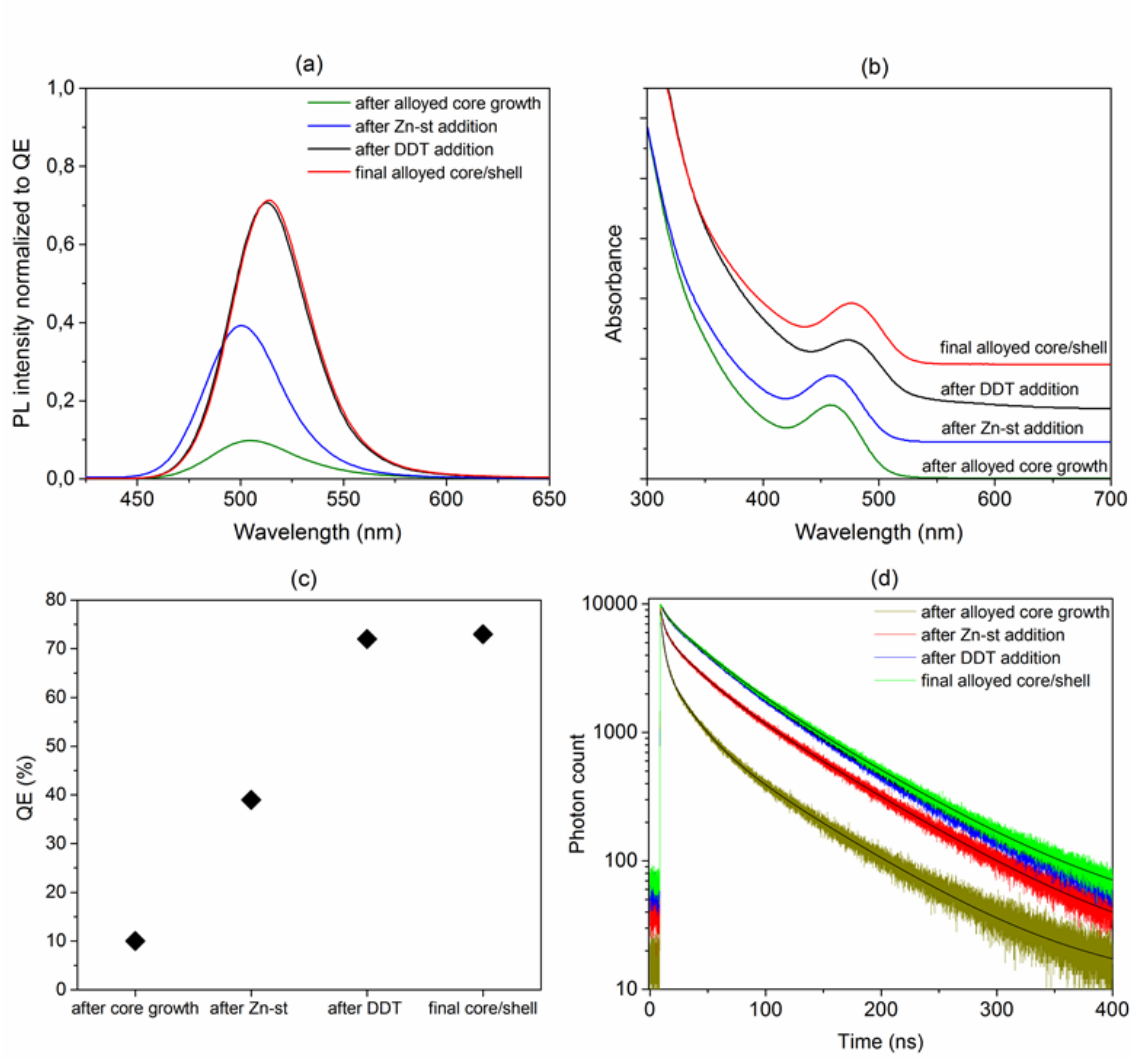

Figure 4.2. 6 (a) Photoluminescence spectra (normalized with respect to QE), (b) absorption spectra (c) the quantum efficiency (d) time resolved photoluminescence decay of InPZnS alloy/ZnS shell before, during and after the shelling process. Reprinted with permission from [45]. Copyright 2016 American Chemical Society.

Table 4.2. 2 Quantum efficiency, photoluminescence peak emission wavelength, absorbance 1st excitonic peak position and FWHM before, during and after shelling process of the alloyed core structure.

Step	Quantum Efficiency (%)	Photoluminescence λ_{max} (nm)	1st excitonic peak (nm)	FWHM (nm)
After alloyed core growth	10	505	459	48
After Zn-st addition	39	500	456	43
After DDT addition	72	513	473	44
Final alloyed core/shell sample	73	514	477	43

Table 4.2. 3 Photoluminescence lifetime components and amplitudes of the exponential fit curves for the before, during and after shelling process of the alloyed core structure. Reprinted with permission from [45]. Copyright 2016 American Chemical Society.

	A_1	τ_1 (ns)	A_2	τ_2 (ns)	A_3	τ_3 (ns)	$\tau_{average}$ (ns) (amplitude)
After alloyed core growth	1176.3 ±15.2	75.716 ±0.686	2227.3 ±52.3	20.020 ±0.448	3779 ±188	3.173 ±0.185	20.279
After Zn-st addition	3388.2 ±23.5	78.471 ±0.381	2649.7 ±60.1	25.833 ±0.634	2497 ±203	3.571 ±0.370	40.218
After DDT addition	4468 ±27.6	79.494 ±0.338	3613.7 ±55.8	35.407 ±0.55	1042 ±188	4.67 ±1.12	53.488
Final alloyed core/shell sample	4801.1 ±27.9	81.396 ±0.322	3549.9 ±59.6	33.332 ±0.575	1098 ±195	4.52 ±1.07	54.406

4.3 Summary

In conclusion, we have shown a full spectrum of InPZnS alloy QDs with color tunability from blue to red, possessing QE up to %78 and FWHM of 45nm with a single ZnS shell over coating, presenting a detailed analysis of the structural, as well as the optical steady state and time resolved photoluminescence characterization to reveal the origin of the high efficiency. The results and efforts on the synthesis of high quality heavy metal free quantum dots will pave the way for sustainable, high-end technological applications of colloidal quantum dots.

4.4 Methods

4.4.1 Materials

Indium acetate ($In(C_2H_3O_2)_3$, 99.99%), myristic acid ($C_{14}H_{28}O_2$, 99%), 1-dodecanethiol ($CH_3(CH_2)_{11}SH$, 98%), zinc stearate ($C_{36}H_{70}O_4Zn$, technical grade), zinc stearate ($C_{36}H_{70}O_4Zn$, purum), tris(trimethylsilyl)phosphine ($[(CH_3)_3Si]_3P$, 95%), 1-octadecene ($C_{18}H_{36}$, 90%), hexane ($C_6H_{14,}$ 95%), acetone ($(CH_3)_2CO$, 99.5%) and methanol (CH_3OH, 99.8%) were purchased from Sigma Aldrich and used without further purification.

4.4.2 Synthesis methods of QDs

The modified methods were used to achieve highly efficient of InPZnS/ZnS alloy/shell QDs with only single shell process [66], [72]. As an exemplary recipe, 0.1 mmol of $InAc_3$ and 0.3 mmol of MA were loaded in 8 mL ODE of three neck flask and solution was heated to 100 ^oC under the vacuum for 1hour (hr) (vacuum level reaching 10^{-3} mbar level). After getting a clear solution, the flask was cooled to room temperature. Following, 0.1 mmol of Zinc Stearate and 0.01 mmol DDT were added into solution and heated at 220 ^oC under the inert atmosphere (Ar gas). When the temperature reached 220 ^oC, 0.1 mmol $(TMS)_3P$ in 1 mL ODE was swiftly injected into hot solution and temperature was quickly increased to 285 ^oC. Once $(TMS)_3P$ was added, the solution color quickly changed to deep, indicating the starting of nucleation process. After waiting for 10 min, alloy growth process was completed and the solution has been cooled to room temperature.

Upon completion of alloy process, 0.2 mmol zinc stearate was added in cooled solution and heated at 230 ^oC under Ar flow. The shell has been started to form within 3 hours and further addition of 0.4 mmol 1-dodecanethiol (DDT) completed the shell process (injection of 0.4 mmol DDT in 1mLODE by syringe pump with rate of 4 mL/h at 230 ^oC for 1 hr) with a thick shell of ZnS. The achieving various emission peak wavelengths of QDs have been obtained by optimization of the precursor as mentioned result and discussion section.

4.4.3 Cleaning process of QDs

The cleaning procedure was carried out the same for all synthesized QDs. The as synthesized QDs were transferred to the centrifuge tube followed by the centrifugation process at 5000 rpm for 10 min. The precipitate including unreacted species of ligands and other precursors were discarded. After repeating the centrifuge procedure for three times using acetone and methanol addition to QD solution, precipitated QDs were dissolved in fresh hexane and kept in vial for further characterization.

4.4.4 Method for calculating the quantum efficiency

The quantum efficiency was measured by comparing the absorbance of standard fluorescent Rhodamine 6G dye (QE: 95% in ethanol) and quantum dot sample followed by the integrated photoluminescence intensity comparison. The excitation of the

samples at the absorbance intersection point and comparison of the integrated fluorescence intensity of standards and samples led us calculate the QE of the QDs using following the equation; [74][40]

$$QE_{QDs}=QE_{Std}\times(I_{QDs}/I_{Std})\times(A_{Std}/A_{QDs})\times(n_{QDs}/n_{Std})^2 \quad (4.4.4.1)$$

Where QE_{Std} and QE_{QDs} are the quantum efficiency of fluorescent standard dye of Rhodamine 6G and synthesized InPZnS/ZnS alloy/shell, I_{QDs} and I_{Std} are the integrated emission peak areas of the synthesized quantum dots and standard, A_{Std} and A_{QDs} are the absorbance values at excitation wavelength (taken to be unity for our experiment, since absorbance curves have been intersected at below absorbance value of 0.1 to prevent reabsorption), $\eta_{ethanol}$ and η_{hexane} are the refractive indexes of the solvents in which the standard and the QDs samples are dissolved, respectively.

Chapter 5

5. Efficient Cd-free FRET Donors

.

The chapter of this thesis is based on the publication “Efficient Förster Resonance Energy Transfer Donors of In(Zn)P/ZnS Quantum Dots”, **Y. Altıntas**, M. Y. Talpur, and E. Mutlugün, *J. Phys. Chem. C*, vol. 121, no. 5, pp. 3034–3043, 2017. Reprinted with permission from [75]. Copyright 2017 American Chemical Society.

5.1 Introduction

Having been a candidate for the billion USD market by 2020, [76] colloidal quantum dots (QDs) have been the focus of the research in optoelectronics along with their exotic optical features they offer for innovative applications for lighting and displays. Since the composition of the QDs have an important side for the environmental concerns, mainly used QDs of CdSe family have started to be challenged by the InP based QDs with the advances in their synthetic chemistry. Although the potential of the InP based QDs have been hindered due to associated trap states, which is a common nature of the III-V material systems, recently, the efforts on the InP based QDs have succeeded in providing high quantum yield particles along with narrow full width at half maximum (FWHM) value [77].

The effect of the individual precursors, their kind and ratio with the other precursors used in the synthesis have a huge impact on determining the optical properties of the QDs, and on achieving the desired tunability in their emission character. In that regards, i.e., the study of the effect of the chain length, [78] the role of the sulfur precursor,[72] the investigation of the ratio of the indium to phosphor precursor and the ligands [45] have all been investigated previously to enhance the photoluminescence quantum yield. Recently, changing the carboxylate ligands with the

phosphine ligands have been demonstrated to control the reactivity of the phosphor precursor during the nucleation phase to possess narrow emission bandwidths [79]. Ramasamy et.al., have reported the influence of trace amount of water to enhance the quality of InP/ZnS, synthesized [80]. As an important step towards the investigation of the single molecular precursors, thiocarbamates have been shown to enhance the optical properties of the synthesized In(Zn)P/ZnS [81]. The suppression of the nonradiative and sub band gap transitions by incorporating Zn into phosphate layer has been investigated by Xi et.al [82]. In their work they have shown that the ratio of 0.5 to 1 for Zn-undecylenate to In, has given the highest quantum yield, above 50% for the particles emitting in the red spectral region.

Apart from the high quantum yield, the emission bandwidth also has a huge impact on the performance evaluation of the quantum dots [83].The narrow FWHM reduces the crosstalk between emitters and provides pure emission characteristics for display applications. With the advances in their size distributions, InP based QDs have started to emerge in monochroatic electroluminescent devices, i.e., QLEDs [62], [74].

As well as the physical processes are involved, the purity of the emitters is also important in order to make them efficient candidates for energy transfer applications. Also known as the nonradiative energy transfer, Förster Resonance Energy Transfer is the energy transfer between donor and acceptor pairs in proximity, based on dipole-dipole interaction. In this sort of arrangement, some critical requirements are to be met in order to generate an efficient FRETing medium. The spectral overlap of the donor emission spectrum with the absorption spectra of the acceptor and the high quantum yield of the donor, both are the factors enhancing the efficiency of the energy transfer. Quantum dots have been used efficiently as energy transferring donors in recent years [41], [84]. In that aspect, one of the important characters of the donor species is that, there should be the minimal overlap between the donor and acceptor emission spectrum. Otherwise, the overlap of the donor emission and acceptor emission prevents the possibility of safe analysis of the emission kinetics and mislead the interpretation. Recently, the potential of the InP QDs as FRET donors have been demonstrated by Thomas et.al. [85]. The recent review by Guzelturk et.al., highlights the importance of utilization of nonradiative energy transfer for the realization of excitonic optoelectronic devices and applications [86].

5.2 Result and Discussion

Within this context, in this work we focus on the study of the synthesis of In(Zn)P/ZnS QDs and in depth investigation of their potential as energy transfer pairs. We have extensively studied the effect of Zn precursor type and ratio for achieving high quantum yield particles along with narrow emission bandwidth for the green emitting donor In(Zn)P/ZnS QDs. For the acceptor species, red emitting InP/ZnS QDs have been synthesized, which we have tuned the emission peak by changing the P precursor concentration used in the synthesis. Upon achieving the high quantum yield particles with narrow emission bandwidth, we have incorporated them into a polymer matrix and have studied the nonradiative energy transfer among them by carefully adjusting their individual ratio to each other. We have demonstrated green emitting In(Zn)P/ZnS at peak emission wavelength of 525 nm, with 81% quantum yield along with 55 nm FWHM as the donor species, and 624 nm emitting red QDs with 43% quantum yield and 56 nm FWHM in our report. The QDs have further been blended with polymer matrix and the emission kinetics upon FRET was extensively studied.

In order to understand the effect of the Zn- precursor on the optical properties of the QDs, we have used elemental Zn, Zinc stearate, Zinc acetate, Zinc acetate dehydrate, and Zinc undecylenate as the Zn precursor. Figure 5.2.1a and Figure 5.2.1b show the evolution of the absorption and photoluminescence spectra of In(Zn)P/ZnS, of which the type of the Zn precursor has been varied, both for the alloyed core growth stage and after the shell coating. Figure 5.2.1c shows the high resolution transmission electron microscopy image of the In(Zn)P/ZnS synthesized with different Zn-precursors. The change in the peak emission wavelength of the colloidal quantum dots has been attributed to the change in their electronic energy levels, rather than a significant change in their physical sizes. In this set of synthesis work, we have used the modified recipe outlined in the literature [45], [87], [88]. The details of the synthesis recipe have been presented in the Methods section. It has been shown that using the elemental Zn possess the lowest quantum yield as compared to the Zn-carboxylates. This is in agreement with the previous studies regarding the demonstration of the enhanced properties of the emission of the InP based QDs with the use of Zn-salts. We have shown that the FWHM, however has not been influenced much by the type of the Zn precursor involved. The color tunability has been observed in the range of 506 to

525 nm with changing the Zn precursor. Regarding the quantum yield, the best performing precursor has been found to be Zinc stearate, a commonly used Zn-carboxylate in the synthesis of InP based quantum dots. Apart from being employed as the Zn source for alloying the InP core and during the shelling process, Zn precursor is being employed to passivate the surface states of the InP based QDs.

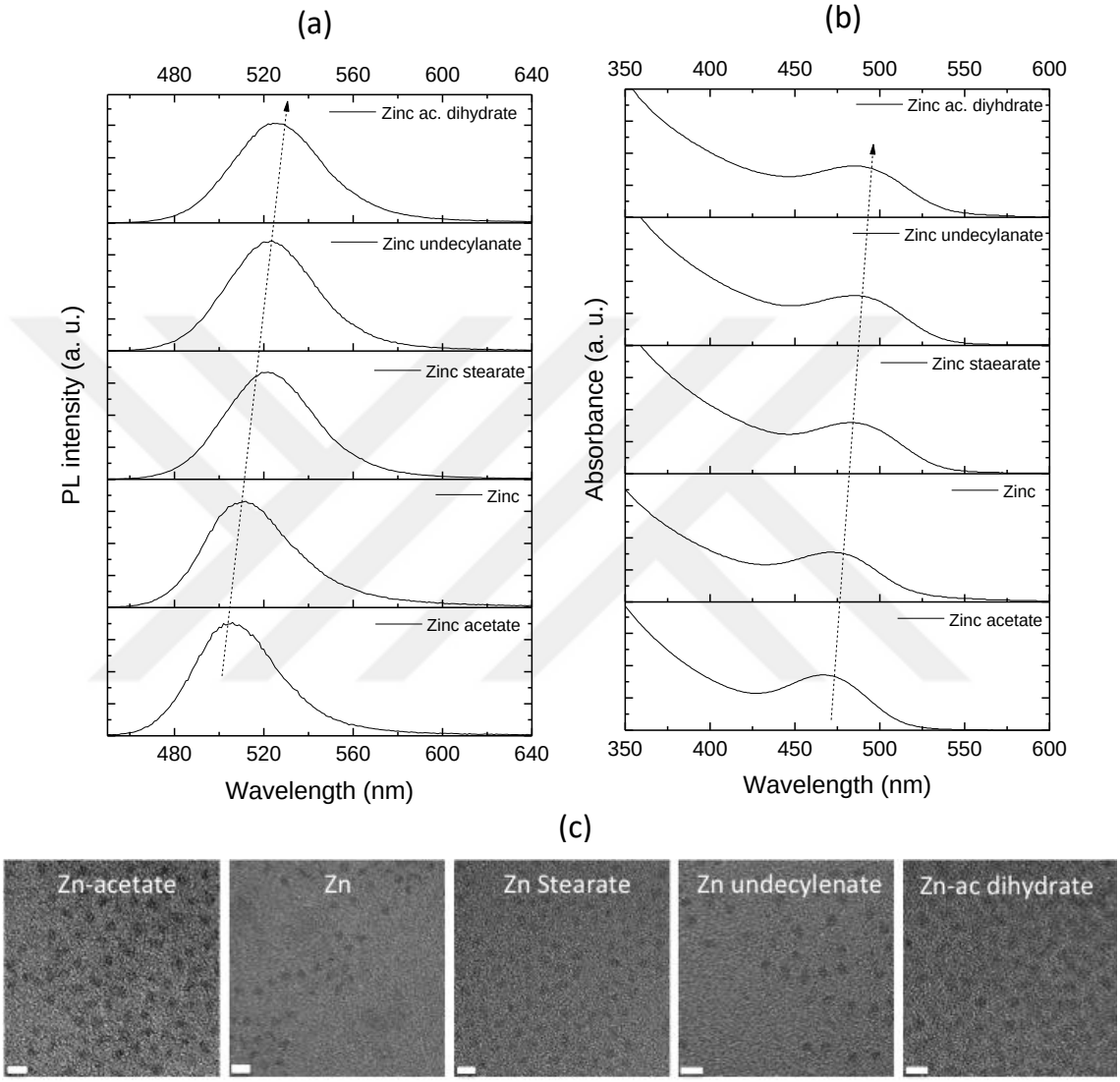

Figure 5.2. 1 (a) Absorption spectrum, (b) photoluminescence spectrum (c) high resolution transmission electron microscopy (HR-TEM) image (scale bar is 5 nm) for In(Zn)P/ZnS QDs using different Zn-precursors. Reprinted with permission from [75]. Copyright 2017 American Chemical Society.

The evolution of the peak emission wavelength and the change in quantum efficiency has been plotted in Figure 5.2.2 and the data for the photoluminescence peak emission wavelength, quantum efficiency, absorbance 1st excitonic peak and full width half maximum value of In(Zn)P/ZnS quantum dots have been given in Table 5.2.1.

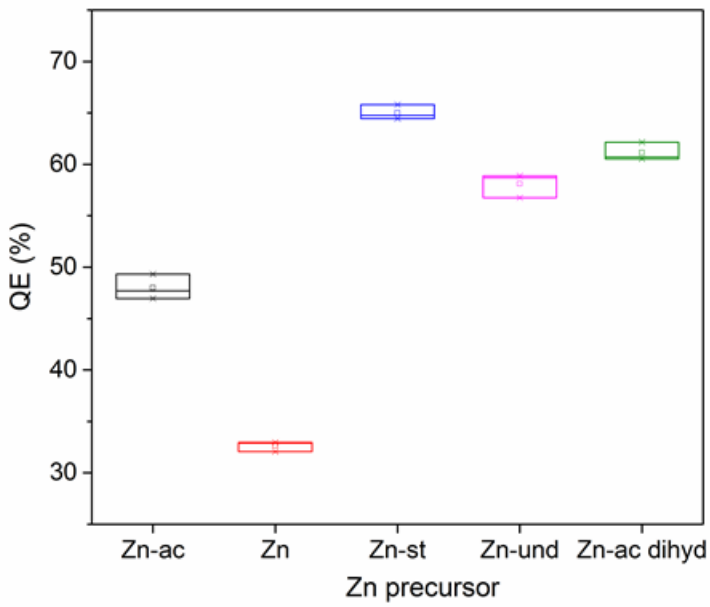

Figure 5.2. 2 Evolution of the quantum yield of QDs using different Zn-precursors. Reprinted with permission from [75]. Copyright 2017 American Chemical Society.

Table 5.2. 1 The Zn-precursor, photoluminescence peak emission wavelength, quantum efficiency (mean), absorbance 1st excitonic peak and full width half maximum value (mean) of In(Zn)P/ZnS quantum dots. Reprinted with permission from [75]. Copyright 2017 American Chemical Society.

Zn-precursor	PL- λ_{max} (nm)	Quantum Efficiency (%)	Absorbance (nm)	FWHM (nm)
Zinc acetate	506	48	466	43
Zinc	511	32	472	46
Zinc stearate	521	65	483	47
Zinc undecylanate	524	58	485	46
Zinc acetate dihydrate	525	61	486	47

As the Zn stearate has been found to be the most optimal source of Zn-precursor for our synthesis work, we have investigated the effect of the concentration of the Zn-stearate at the alloyed core growth stage. In this set of arrangement, we have kept all the concentrations and parameters to be the same during the synthesis (In:0.12 mmol,

Myristic Acid 0.36 mmol, 1-dodecanethiol 0.025 mmol, and tris trimethylsilyl phosphine 0.08 mmol) and modified the ratio of the Zn stearate concentration used in the synthesis. We have found out that increasing the concentration of the Zn during the alloyed core growth stage the quantum yield enhances significantly up to 87% after the ZnS shell growth. We have attributed the increase in the photoluminescence quantum yield to the passivation of the surface defects by using excessive amount of the Zn salt. However, although quantum yield increases with increasing the amount of the Zn-precursor used, the chemical yield of the synthesis does not increase accordingly. The synthesis by-products increase as having higher concentration of the Zn precursor.

In the literature, Park et.al., recently reported 85% photoluminescence yield with InP/GaP/ZnS with FWHM reaching 41 nm [68]. Our result is one of the best reported work with such type of quantum dots of In(Zn)P/ZnS with 55nm of FWHM using a single ZnS shell coating. Further overcoating the alloyed core shell particles, we have calculated the quantum yield increasing to 88% and emission bandwidth reducing to 50 nm. Figure 5.2.3 shows the evolution of the quantum yield with changing the Zn-amount used in the synthesis and Table 5.2.2 presents the optical properties of the synthesized QDs with changing the amount of the Zn precursor from 0.2 mmol to 1.0 mmol.

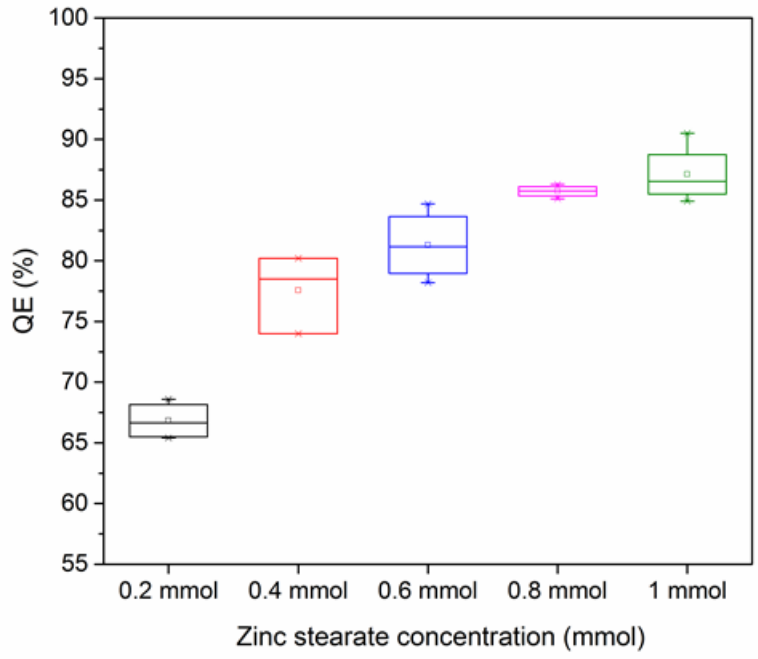

Figure 5.2. 3 Evolution of quantum yield as a function of Zn-stearate concentration. Reprinted with permission from [75]. Copyright 2017 American Chemical Society.

Table 5.2. 2 Photoluminescence peak emission wavelength, quantum efficiency (mean), absorbance 1st excitonic peak and full width half maximum value (mean) of In(Zn)P/ZnS quantum dots with changing the Zn-Stearate concentration. Reprinted with permission from [75]. Copyright 2017 American Chemical Society.

Zinc stearate amount	PL- λ_{max} (nm)	Quantum Efficiency (%)	Absorbance (nm)	FWHM (nm)
0.2 mmol	516	67	474	48
0.4 mmol	515	77	475	47
0.6 mmol	525	81	482	55
0.8 mmol	517	86	474	56
1.0 mmol	515	87	471	54

As for the red emitting QDs, our target is to achieve an efficient FRET acceptor with narrow FWHM, allowing for non-cross talk with the green emitter. In the synthesis work, we have modified the recipe in the literature [70] and by changing the concentration of the dimethylamino phosphine, $(DMA)_3P$, we have tuned the emission properties of the red emitters. Figure 5.2.4a and 5.2.4b presents the absorption and emission profiles of the particles, whereas Figure 5.2.4c and 5.2.4d shows the FWHM and quantum efficiency of colloidal particles as a function of concentration of the P-precursor. We have shown that, decreasing the concentration of the $(DMA)_3P$ red shifts the emission, enhances the quantum yield of the synthesized QDs and possess narrow emitters with 56 nm FWHM. The enhancement of the quantum yield from 29% to 43% and narrowing the FWHM from 63 nm to 56 nm with decreasing the P-precursor ratio has been attributed to the generation of Indium rich surface, which provided better protection against defect states. However, decreasing the $(DMA)_3P$ concentration further have resulted in decreased quantum yield and increased FWHM, which is attributed to P-precursor not being sufficiently enough to provide defect free particles. The optical properties have further been presented in Table 5.2.3 for the red emitting QDs.

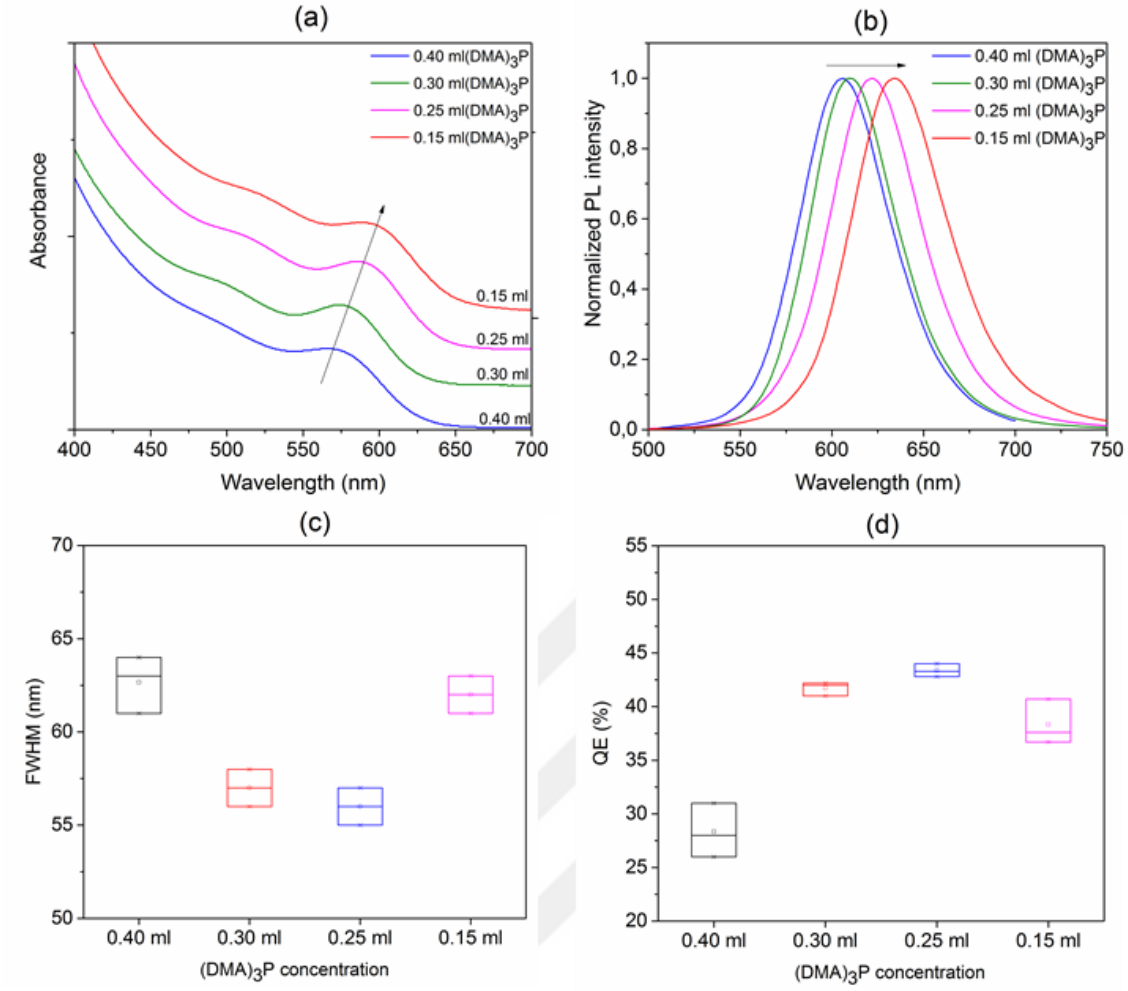

Figure 5.2. 4 (a) The absorbance, (b) emission and (c) FHWM and (d) quantum yield evolution of QDs with changing the $(DMA)_3P$ concentration. Reprinted with permission from [75]. Copyright 2017 American Chemical Society.

Table 5.2. 3 Photoluminescence peak emission wavelength, mean value of the quantum efficiency, absorbance 1st excitonic peak and mean value of the full width half maximum value of red emitting quantum dots with changing the amount of $(DMA)_3P$. Reprinted with permission from [75]. Copyright 2017 American Chemical Society.

Used $(DMA)_3P$	Quantum Efficiency (%)	Photoluminescence $\lambda_{max\ (nm)}$	Absorbance peak value (nm)	FWHM (nm)
0.40 ml	29	605	566	63
0.30 ml	42	615	577	57
0.25 ml	43	624	587	56
0.15 ml	38	634	591	62

In order to investigate the nonradiative energy transfer between the green and red emitters, we have studied the formation of the polymeric films of quantum dots by blending them with polymethylmethacrylate (PMMA) (10% in toluene) for overnight and drop casting on glass slides. We have prepared samples with changing the ratio of the intensities of the green and red emitters in the following ratio of (Red: Green) with (0.25:0), (0.25:1), (0.5:0), (0.5:1), (1:0), (1:1), (2:0), (2:1), and (0:1). By this set of samples we were able to study the effect of the emission kinetics of the acceptor in the presence of donor and the emission kinetics of the donor in the presence of acceptor together with the control groups of donor only and acceptor only samples. Figure 5.2.5a demonstrates the in solution photoluminescence and absorption spectra for the chosen FRET pair. Figure 5.2.5b shows the photoluminescence excitation spectra, which resemble the absorbance curves. The emission kinetics, i.e., the time correlated single photon counting decays of the emitters has been presented in Figure 5.2.5c. Figure 5.2.5d and 5.2.5e shows the images of the green and red quantum dots using high resolution transmission electron microscopy.

During the measurements of time correlated single photon counting, 375 nm emitting diode laser has been used as the pump source with tunable repetition range to cover the whole decay of the emitter (using PicoQuant- FluoTime 200 system equipped with Time Harp 260.) The lifetime of the green emitter has been calculated as 59.45 ns, whereas red emitter lifetime has been found as 53.46 ns, when fit with 2 exponentials (in solution). The amplitude-weighted lifetime is given as,

$$\tau_{amp} = \frac{A_1\tau_1 + A_2\tau_2}{A_1 + A_2} \tag{5.2.1}$$

and intensity-weighted lifetime is given as,

$$\tau_{int} = \frac{A_1\tau_1^2 + A_2\tau_2^2}{A_1\tau_1 + A_2\tau_2} \tag{5.2.2}$$

For the investigation of FRET, we have carried out our discussions through the amplitude-weighted lifetimes, rather than the intensity weighted lifetime [89].

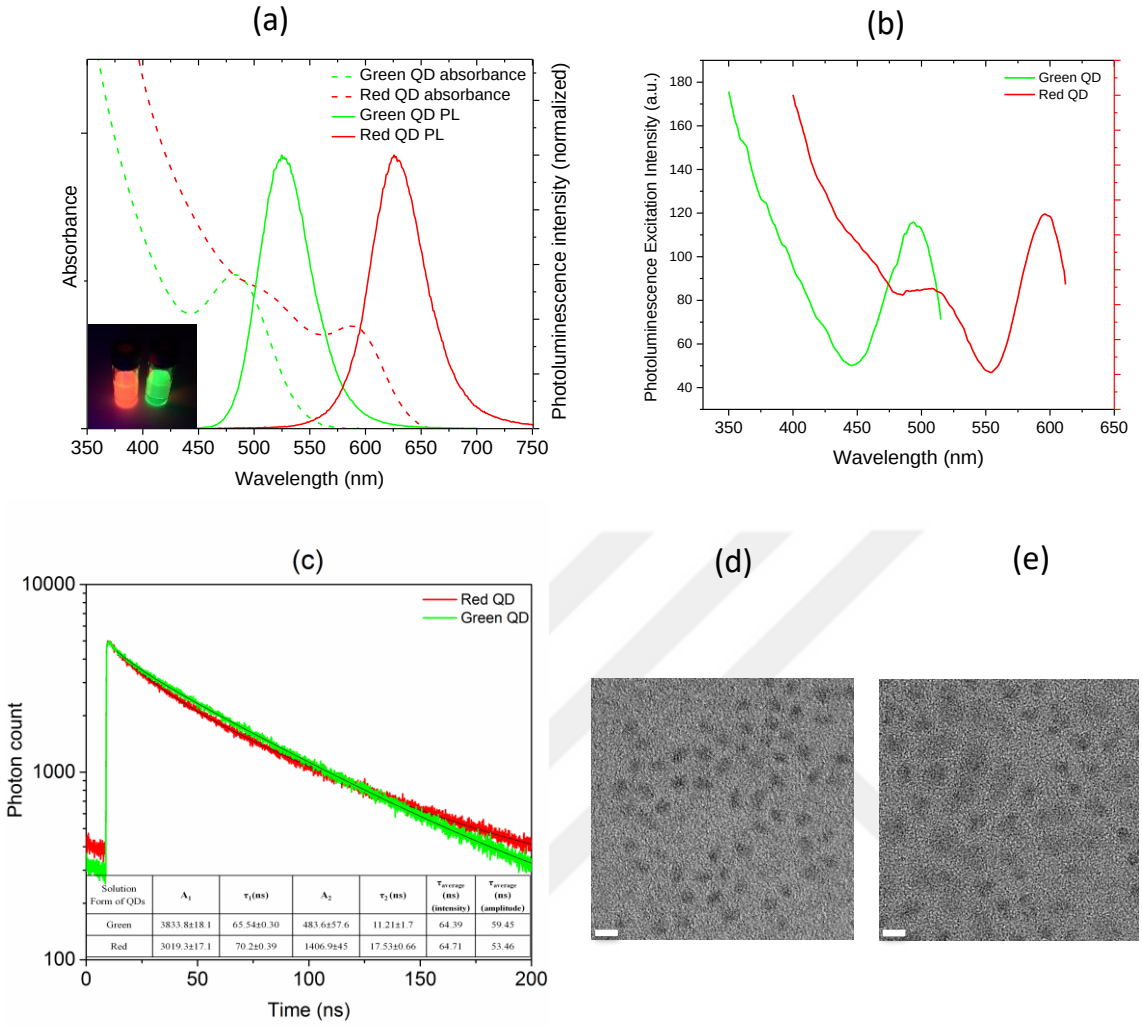

Figure 5.2. 5 (a) Absorbance and photoluminescence spectra, (b) Photoluminescence excitation spectra of the green and red emitting QDs, (c) Time correlated single photon counting decays of green and red emitting QDs along with their lifetime coefficients, lifetime components, intensity weighted and amplitude weighted lifetimes, (d) High resolution transmission electron microscopy image of green QDs, (e) High resolution transmission electron microscopy image of red QDs. (scale bar is 5 nm). Reprinted with permission from [75]. Copyright 2017 American Chemical Society.

We have investigated the effect of acceptor on the emission kinetics of the donor QDs. Figure 5.2.6 presents the time resolved decays of the donor control group (0:1) and with increasing the acceptor in the film sample (analyzed at peak donor emission wavelength). Fitting with the 3-exponentials, the amplitude-weighted lifetime of the only green QD containing sample was found to be 14.77 ns. By introducing acceptor QDs to the medium, the lifetime of the donor decreases to 9.58 ns in the case of (0.25:1), to 9.63 ns in the case of (0.5:1), to 7.48 ns in the case of (1:1), and to 4.39 ns in the case of (2:1) (see Table 5.2.4). The observation of the faster decay for the case of

donor is expected as the green emitter is employed as the energy-transferring agents. The lifetime components get shorter as more and more acceptors per donor are introduced to the medium.

One can calculate the FRET efficiency from the following equation,

$$\eta = 1 - \frac{\tau_{DA}}{\tau_D} \tag{5.2.3}$$

where τ_{DA} is the lifetime of the donor in the presence of acceptor and τ_D is the lifetime of the donor in the absence of the acceptor. From the observed lifetimes, the FRET efficiency has been calculated as 70.3% at the maximum level.

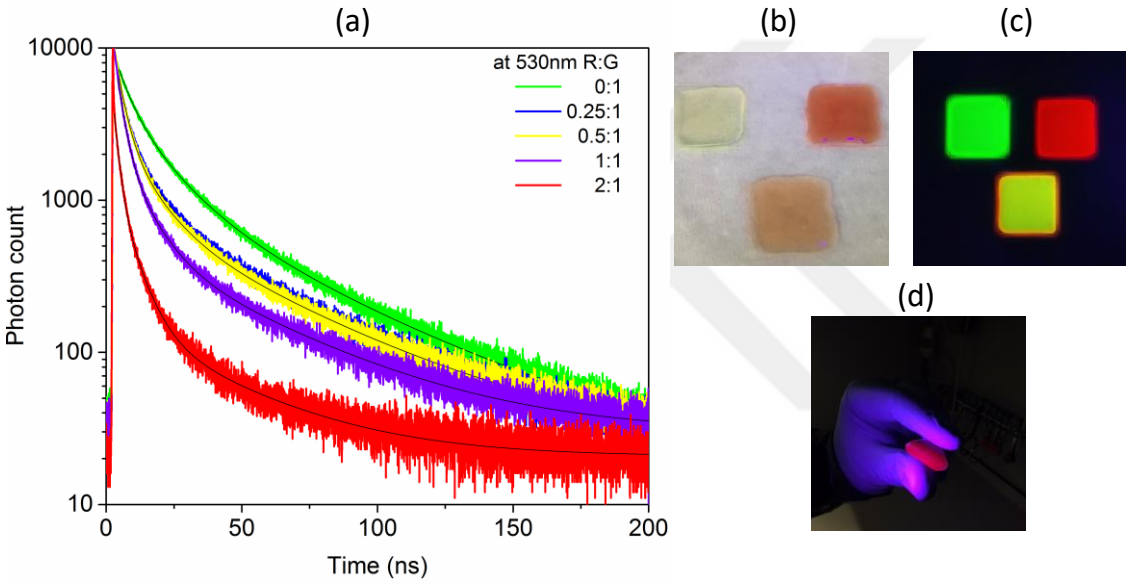

Figure 5.2. 6 a)Time correlated single photon counting decays of FRET mediated system with green and red emitting QDs changing their ratio in film. (at donor peak emission wavelength) b) a photograph of bare donor, bare acceptor, and mixed film under daylight, c) a photograph of bare donor, bare acceptor, and mixed film under UV illumination, c) a photograph of the flexible red emitting film under UV illumination. Reprinted with permission from [75]. Copyright 2017 American Chemical Society.

Table 5.2. 4 The amplitudes, lifetime components and amplitude weighted lifetimes for green and red QD (at donor emission wavelength). Reprinted with permission from [75]. Copyright 2017 American Chemical Society.

Red:Green	A_1	τ_1(ns)	A_2	τ_2 (ns)	A_3	τ_3 (ns)	$\tau_{average}$ (ns) (amplitude)
0:1@530nm	1179.1±14.9	48.37± 0.43	3329.2± 50.1	14.78± 0.19	4080± 112	5.05± 0.15	14.77
0.25:1@530nm	867.1±12.6	44.75± 0.50	2490.7± 56.1	9.851± 0.20	4709± 140	2.97± 0.1	9.58
0.5:1@530nm	756±11.8	45.47± 0.55	1987.5 ± 49.4	10.54± 0.23	4403± 128	3.07± 0.1	9.63
1:1@530nm	471.9±9.86	43.99± 0.72	1702.5± 48	8.89± 0.22	4048± 126	2.63± 0.1	7.48
2:1@530nm	139.58±6.58	36.93± 1.42	1065.8± 40.4	6.32± 0.19	2480± 117	1.74± 0.1	4.39

In order to see the effect of donor QDs on the acceptor QD lifetime, we have analyzed the lifetime of the acceptor at its peak emission wavelength. In this analysis, we have monitored the lifetime of the acceptor sample with and without donor in the proximity. The characterizations have been performed at 4 different concentration regimes with increasing the acceptor amount, however keeping the donor amount the same. In that regards, we have systematically increased the acceptor amount per same amount of donor in the film, together with their control groups. Figure 5.2.7 presents the lifetime decays, monitored at the acceptor emission peak wavelength for different concentrations of acceptor in the medium. As a result of FRET, one expects the increase in the lifetime of the acceptor as a result of energy feeding. However, since the donor amount is the same in the medium, the increase in the acceptor lifetime by introducing donor QDs reduces (see Figure 5.2.7c and Figure 5.2.7d). This is due to the fact that, from the low to high concentration limit of the acceptor, there are less and less donor molecules for each acceptor, which limits the energy transfer. Expressing in terms of the acceptor lifetimes; at red to green ratio of 1:1, compared with the bare acceptor only, the acceptor lifetime increases from 12.97 ns to 19.91 ns. This is also visible from the energy feeding observation in the first few nanoseconds of the decay. As the acceptor concentration is further increased to a ratio level of red:green 2:1, the bare acceptor lifetime increases from 10.87 ns to 14.81 ns.

It is worth noting here that at the low concentration regime, although less acceptor per donor is expected to have a high energy feeding observed from the lifetime, the other consideration is the interparticle distance. Therefore, we have observed that reducing the red: green ratio further to 0.25:1 does not possess large energy feeding to the acceptor (Fig 5.2.7a). Therefore, there is a tradeoff observed with the less acceptor per donor favoring the energy feeding to the acceptor, however since particle to particle distance is now reduced, the effect is being hindered. In our experiments, the maximum energy feeding to the acceptor from the donor is observed in case of red:green ratio of 0.5:1which corresponds to the lifetime modification of 10.68 ns to 20.81 ns.

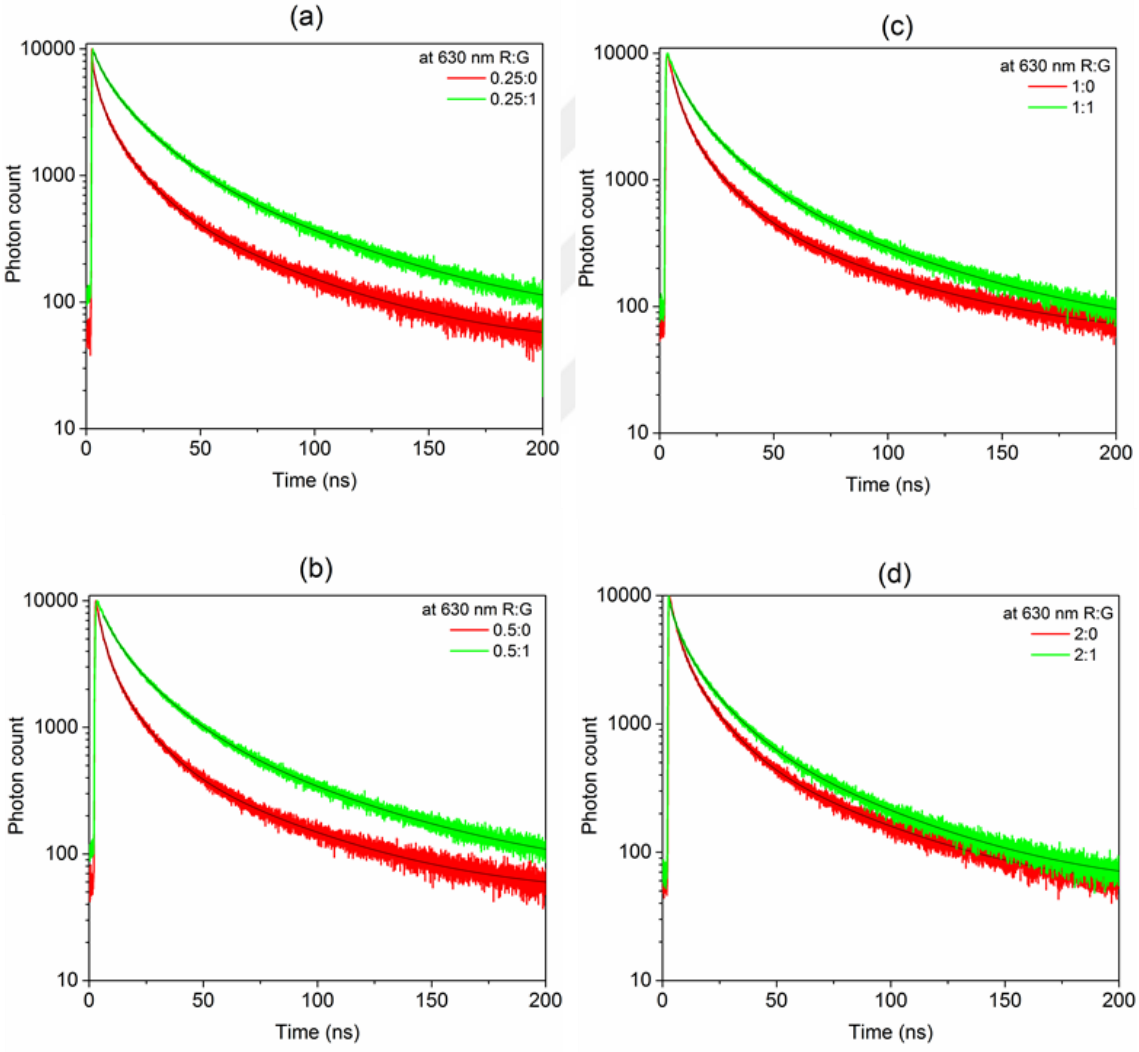

Figure 5.2. 7 Time correlated single photon counting decays of FRET mediated system with green and red emitting QDs changing their ratio in film with red to green ratio of a) 0.25:0 and 0.25:1, b) 0.5:0 and 0.5:1, c) 1:0 and 1:1, d) 2:0 and 2:1. (at acceptor peak emission wavelength). Reprinted with permission from [75]. Copyright 2017 American Chemical Society.

The results of the lifetime analysis have been summarized in Table 5.2.5, along with the amplitude and lifetime components.

Table 5.2. 5 The amplitudes, lifetime components and amplitude weighted lifetimes for green and red QD (at acceptor emission wavelength). Reprinted with permission from [75]. Copyright 2017 American Chemical Society.

Red:Green	A_1	τ_1(ns)	A_2	τ_2 (ns)	A_3	τ_3 (ns)	$\tau_{average}$ (ns) (amplitude)
0.25:0 @630nm	774,3 ±12,6	49,27 ± 0,61	2913,3± 48,5	12,32± 0,19	3076± 132	3,05± 0,15	12.34
0.25:1 @630nm	1689,6 ±17,8	54,77 ± 0,45	4820,3± 55,4	16,63± 0,18	2841± 133	4,65± 0,26	19.88
0.5:0 @630nm	699,5 ±12,1	49,56 ± 0,65	3070,1± 50,5	11,96± 0,17	4190± 135	3,24± 0,12	10.68
0.5:1 @630nm	1300± 14,9	58,24 ± 0,50	3864±4 6,1	17,9± 0,20	2501± 101	5,84± 0,28	20.81
1:0 @630nm	678,4 ± 11,3	54,39 ± 0,69	2681,9± 44	13,56± 0,20	3267± 111	3,88± 0,15	12.97
1:1 @630nm	1041± 13,4	60,30 ± 0,59	3467,5± 43,3	17,85± 0,20	2457,3± 97,2	5,69± 0,26	19.91
2:0 @630nm	811,8 ± 13,1	48,56 ± 0,59	3523,5± 53,3	12,17± 0,16	4642± 142	3,30± 0,11	10.87
2:1 @630nm	1148,5 ±15,2	48,74 ± 0,45	3878,8± 52,4	13,74± 0,17	3165± 130	3,81± 0,18	14.81

Furthermore, we have carried out steady state photoluminescence measurement for the acceptor and donor pair with a predetermined ratio of red:green of 0.5:1. Considering the control groups of bare donor (red:green 0:1) and bare acceptor (red:green 0.5:0), upon excitation with 375 nm monochromatic light, we have seen that the intensity of the red enhances more than two-folds (%107) when prepared in a film structure together with the donor-green emitting species. On the other hand due to energy transfer, the integrated intensity of the green emitting QDs quenches to 27% of its initial intensity (Figure 5.2.8a). In order to reveal the origin of the photoluminescence enhancement, we have carried out the photoluminescence excitation (PLE) measurement of the donor only, acceptor only and the mixed film. Figure 5.2.8b demonstrates the enhanced PLE signal for the acceptor quantum dot. In the low wavelength regime, PLE signal possess around 2 folds enhancement (when

monochromator is set at red emission peak), and is in good agreement with the observed enhancement in steady state photoluminescence.

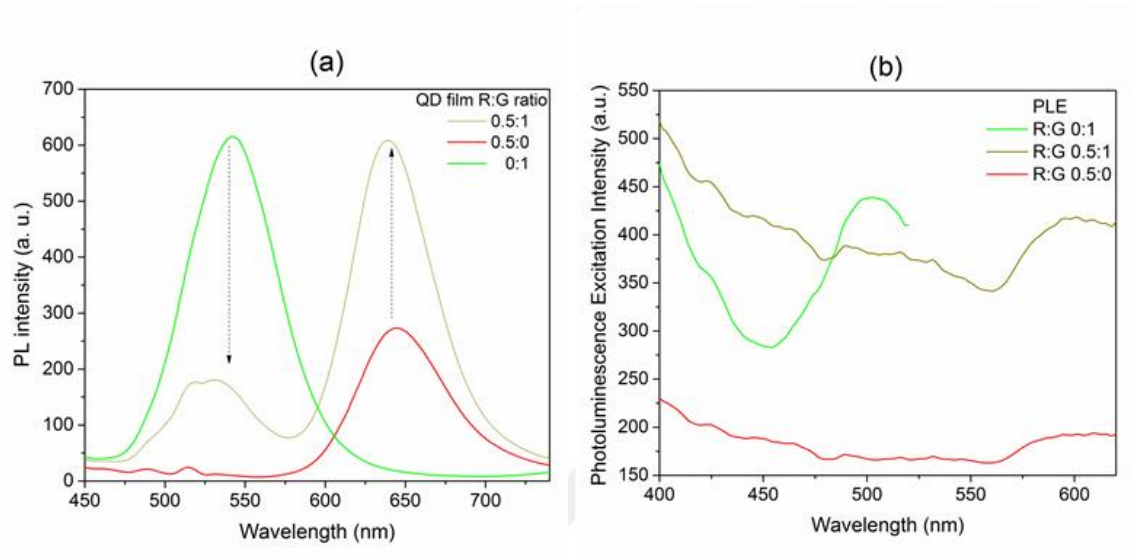

Figure 5.2. 8(a) Steady state photoluminescence enhancement of the mixed film of green and red emitters. (b) Photoluminescence excitation spectra of the bare green (at green peak emission), bare red (at red peak emission) and mixed film (at red peak emission). Reprinted with permission from [75]. Copyright 2017 American Chemical Society.

5.3 Summary

In conclusion we have made an extensive investigation on the effect of Zn-precursor on the quality of the In(ZnP) quantum dots. The type of the Zn-precursor and its concentration has been studied and we achieve over 80% quantum yield for the green emitting colloidal quantum dots. The green emitting donor quantum dots have been mixed with red emitting acceptor quantum dots and Förster type nonradiative energy transfer has been investigated between the QD-QD pairs. We have demonstrated and discussed the effect of donor and acceptor in the presence and absence of the individual and their influence on the emission kinetics. Our results have indicated up to %70.3 FRET efficiency between green and red emitting InP based quantum dots. Furthermore, we have showed over 2 folds enhancement of the acceptor photoluminescence intensity upon FRET. The efforts on investigation of the high efficiency and narrow bandwidth environmentally free component based colloidal particles and the study of excitonic interaction among them will open up new rooms for further research on the subject.

5.4 Methods

All the mentioned chemicals were purchased from Sigma Aldrich and used without further purification.

5.4.1 Synthesis of green emitting QDs

Following the modified recipes outlined in previous works, [45], [87], [88] Indium acetate (0.12 mmol), myristic acid (0.36 mmol) and 6mLof octadecene were added in the three necked flask, heated to 100 ^{o}C and kept under vacuum for 1 hour. The solution was cooled to room temperature, and then, zinc stearate purum (0.1 mmol) (or other Zn sources used) and 1-dodecanethiol (0.025 mmol) was added and flask was heated to 220 ^{o}C and under argon atmosphere and stirring. After that, the solution of tris trimethylsilyl phosphine (0.08 mmol in 1 mL octadecene) was swiftly injected in the hot solution at 220 ^{o}C, and then, increased the temperature at 285 ^{o}C, waited for 10 min. When the synthesis finished, the solution was cooled at room temperature.

For the shell coating process, zinc stearate purum (0.2 mmol) (or other Zn sources used) was added to the reaction flask at room temperature, and heated to 230 ^{o}C for 3 hours. After that, the solution of 1-dodecanethiol (0.4 mmol in 1 mL octadecene) was injected drop by drop into the flask and kept for 1 hour. When the shell synthesis process was finished, the solution was cooled to room temperature. Firstly, the precipitate including unreacted species of ligands and other precursors were removed by 5mLhexane with 5000 rpm for 10 min. Secondly, the supernatant solution was precipitated with 20 mL of acetone and 3 mL methanol, then, centrifuged at 5000 rpm for 10 min by two times . The particles were re-dissolved in hexane.

5.4.2 Synthesis of red emitting QDs

For the synthesis of highly efficient red emitting InP/ZnS QDs, the reported method outlined previously in the literature [70] was modified by using tris dimethylamino phosphine instead of tris diethyl amino phosphine, and modifying the purity of the precursors and other conditions. The InP/ZnS QDs are prepared by hot injection method on a schlenk line with standard air-free route. All chemicals are used without further purification.

$InCl_3$ (99%, 0.45 mmol), $ZnCl_2$ (98%, 2.2 mmol) and 5 mL oleylamine (technical grade, 15mmol) were added in the round bottom flask and heated at room temperature for 5 minutes (min) under vacuum and Argon (Ar) gas sequentially. The temperature was then increased to 120^{o}C under 800 rpm stirring for 1 h under the vacuum. After, solution was heated to 180 ^{o}C under an Ar-gas flow. When the temperature reached to 180 ^{o}C, 250 µL of tris dimethyl amino phosphine (prepared in glove box) is injected and the reaction was allowed to proceed for 20 min with strong agitation continuously. After 20 min, the reaction was continued further for shell process without cooling to room temperature of the reacting mixture.

Initially, a stock solution of sulfur in trioctylphosphine (TOP-S) was prepared in glove box with concentration of S (0.72 g) into TOP (10 mL) and stock solution of zinc stearate (Zn-st, purum) in 1-octadecene (1-ODE, 90%) was prepared by dissolving Zinc stearate purum (4.5 g) into 1-ODE (20 mL) under an Ar-gas atmosphere at 180 ^{o}C in the 50 mL three-necked flask. 1 mL saturated stock solution of TOP-S was injected in the solution of InP QDs at 180 ^{o}C for 40 min (total reaction time completed=60min). The solution was then heated from 180 to 200 ^{o}C and reaction was allowed to proceed for 1 h (total reaction time proceeded=120 min). Later, 4 mL of Zinc stearate-Octadecene (ODE) stock solution was added slowly into mixture and temperature was increased from 200 ^{o}C to 220 ^{o}C and kept there for 30min (total reaction time completed=150 min). Then, 0.7 mL of saturated TOP-S solution was injected slowly and the flask was heated from 220 ^{o}C to 240 ^{o}C for 30 min (total reaction time finished=180 min). 2 mL of Zinc stearate-ODE stock solution was slowly injected in the reaction mixture at 240 ^{o}C and heated to 260 ^{o}C for 30 min (total reaction time completed=210 min). Finally, the reaction was stopped at 210 min and flask was allowed to cool down to room temperature for final purification of synthesized QDs. The final product was transferred into centrifuge tubes and washed with hexane two times at 5000 rpm for 5 min each to eliminate any solid unreactive by products. The supernatant solution was washed using acetone and methanol for 20 min at 5000 rpm, and the final QDs were dispersed in hexane/chloroform for further characterization and use.

The quantum efficiency is calculated by comparing the emission intensity of the QDs with organic dye, Rhodamine 6G (for green emitters), or Sulforhodamine (for red emitters) with quantum efficiency of 95% in absolute ethanol, using the Eqn.5.4.2.1

$$QE_{sample}=QE_{ref.\ dye}\times(I_{sample}/I_{ref.\ dye})\times(n_{sample}/n_{ref.\ dye})^2 \quad (5.4.2.1)$$

Here "I" represent the integrated photoluminescence intensity when the reference dye and sample has been excited at the same excitation wavelength (extracted from the intersection point at the absorbance curves). When measuring the quantum yield, the concentration of the solutions have been adjusted as not to exceed 0.1-0.2 to prevent reabsorption and excitation wavelength (thus the absorbance intersection) has been chosen as to be appropriate range for the excitation of the reference dyes to prevent misleading interpretation.

5.4.3 Characterizations

Photoluminescence characterizations and UV-Vis spectroscopy were performed using Agilent-Cary Eclipse fluorescence spectrophotometer and UV-Vis spectroscopy Thermo Genesys 10S spectrometer respectively. Time correlated single photon counting measurements were carried out using Pico Quant FluoTime 200 equipped with 375 nm pulsed laser diode, TEM images were taken by using FEI Tecnai G2 F30, EDX measurements were collected during the TEM imaging and XPS measurements were conducted using Thermo Scientific K-Alpha X-ray Photoelectron Spectrometer System. Dynamic light scattering measurements were performed using Malvern Zeta Sizer.

Chapter 6

6. Cd-free QDs Salt Pellets for WLED Application

The chapter of this thesis is based on the publication "Excitonic interaction amongst InP/ZnS salt pellets," Y. Altintas, A. Faruk Yazici, M. Unlu, S. Dadi, S. Genc, and E. Mutlugun, *J. Mater. Chem. C*, vol. 5, no. 29, pp. 7328–7336, 2017. Reprinted with permission from [90]. Copyright 2017 Royal Society of Chemistry.

6.1 Introduction

Semiconductor nanocrystals known as quantum dots (QDs) have acquired the title of yielding distinctive optical properties by offering full tunability of excitation wavelength through particle size alteration, greater color purity given to narrow-band emission and high photoluminescence quantum yields. The syntheses of colloidal quantum dots have been studied widely since it was first published in early 1980s [91]–[94]. CdSe used to be an unmatchable QD compound in terms of high photoluminescence quantum yield (PL-QY), narrow full width at half maximum (FWHM) and long term stability [93], [95], [96]. Being a heavy metal, cadmium had to face environmental concerns and evoked researchers to develop safer alternatives [97]. Among several candidates, InP-based QDs has drawn the most attention [45], [75], [98]–[100].

Recent research efforts are concentrated on the implementation of QDs into various applications, e.g., photonics, optoelectronics, energy harvesting, displays, or biological labeling. Colloidal quantum dots have been gaining grounds as a promising candidate for replacing current display technologies. In 2015, Samsung has managed to successfully implement QDs into a commercially available TV following their success

in lab scale introduction of a QD integrated electroluminescent displays [37]. The demand for QD TV panels is projected to exceed 10 million units in 2017 in market forecasts [101]. Moreover, LEDs attract researchers by providing up to 75% energy saving compared to conventional lightning methods and are projected to dominate lightning industry in the near future [102]. Currently, the most common white LEDs mainly consist of a phosphorus layer on top of a readily optimized blue LED. Due to the degradation of phosphorus layer, the inconsistency of the white light still remains as an issue [103]. On the other hand, integration of quantum dots into LEDs provides enhanced luminous efficiency, color purity and color temperature [96], [104], [105].

Although QDs offer aforementioned advantages over their counterparts, the decrease in the quantum efficiency over time remains as a problem to overcome. Hence, utilization of QDs in such applications is strongly bound to a proper stabilization medium. Polymers have been used to encapsulate QDs to provide a protection from oxygen and moisture. However, a reliable protection method that is easily processable but does not degrade photoluminescence performance keeping high stability is still under research. Otto et al. accomplished this task by incorporating QD nanoparticles into common salt crystals without compromising the merits to a large extent [106]. Yet, satisfying crystallization process is only achieved under room temperature which takes up to several weeks. Benad et al. conceived a less time consuming and versatile method for protection, which employed the suspension of QDs onto salt crystals by a process called cold flow. This method provides direct implementation of various QDs into a salt matrix without the need of ligand exchange, high QD loadings and decent conservation of solution phase PL-QYs [107].

Encapsulation of QDs within polymer matrix paves the way for many challenging issues such as moisture and oxygen leading decrease in quantum yield. As an alternative method, incorporation of QD into appropriate matrix including milled salt makes these nanoparticles more stable in long term, preservation of initial photoluminescence capability and non-aggregated in ionic plane. Embedding procedure of QD into milled salt is followed by evaporation of solvent under vacuum. Inorganic salt loaded with nanoparticles turns into transparent pellet with high visual quality. This approach is applicable to overcome thermal, chemical and photochemical degradation issues in the proof of concept tests [108], [109]. Colloidal stability feature of QD capping ligand is

essential in the course of incorporation of nanocrystals into salt matrices homogeneously. Proper ligand selection during QD syntheses ensures high QY, prevention of undesirable agglomeration. Deterioration of QD could be precluded by optimizing conditions, selecting appropriate salt solution (NaCI, KCI, KBr) maintaining electrostatic forces in balance during crystallization. A robust etching of QDs could be concluded with undesired shifting of PL spectrum in crystallization procedure [110].

The importance of non-radiative energy transfer at nanoscale, known as Förster Resonance Energy Transfer (FRET), for optoelectronic and photovoltaic applications has been substantiated [111]. This excitonic interaction takes place via dipole-dipole coupling when a donor and an acceptor nanoparticle are confined in a critical spatial proximity, along with some other requirements such as overlap of their spectrum. In addition to being used as a characterization tool in biology and chemistry, FRET has also been shown to be a vital phenomenon for light harvesting, [112], [113] bio-imaging[114] and sensing[115] applications. In addition, color rendering properties of light can be modified based on energy transfer [32]. Emission and reabsorption of a photon referring to radiative energy does not clarify this electrodynamic phenomenon. A reliable energy transfer is presumed not necessarily requiring a physical contact but a particular Förster distance (10 nm or less) by overlapping spectral region between donor (D) emitting spectrum with the acceptor (A) absorption spectrum at longer wavelength. The behavior of coupled oscillators assists to understand the working principle of non-radiative energy transfer mechanism. Near field electromagnetic effect of dipole transition in donor triggers the acceptor transition dipole. As FRET efficiency is particularly related to D-A distance and oscillating strength of acceptor, the FRET rate depends upon D-A spectrum overlap, donor quantum efficiency and dipole transition orientation of D-A pair. Recently, colloidal QD based FRET has been studied for CdSe based nanocrystals within LiCl salt matrix with FRET efficiency level reaching 53.9% [116]. Although a variety of Cd based material systems have been studied in their pellet form, an investigation of excitonic interactions amongst Cd-free pellets and the generation of white light based on such material system have not been studied thus far. In this regards, in this work we demonstrate InP/ZnS colloidal QDs embedded in salt crystal and study excitonic interactions by changing the donor and acceptor pairs with FRET efficiency level of 65% calculated from the modification of the donor lifetime before and after introducing the acceptor in close proximity. By optimizing the donor

acceptor ratio within the pellet structure, we demonstrate an efficient white light emitting device with 82.5 color rendering index and correlated color temperature of 3014.2 K and high luminous efficacy of optical radiation value of 368.5 lm/Wopt

6.2 Result and Discussion

In this study, we synthesized highly luminescent Cd-free red and green quantum dots (QDs) by using modified recipe in the literature [66], [70], [72], [75] given in Methods section. Absorbance and photoluminescence spectra of synthesized green and red QDs have been given in Figure 6.2.1 with their quantum efficiencies as 90%, 52% and full width half maximum values as 52 nm, 62 nm, respectively. These colloidal QDs have further been employed as donor and acceptor pairs.

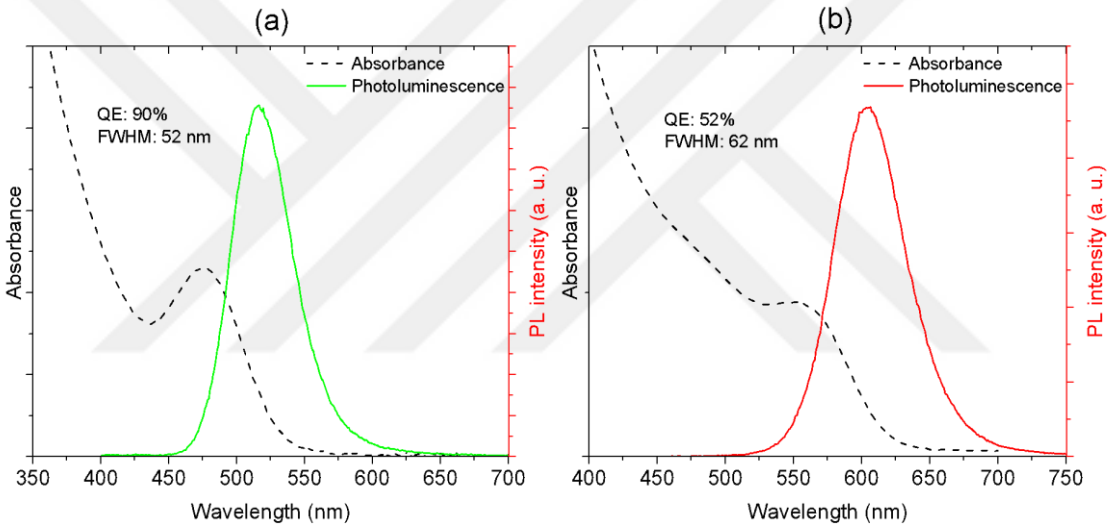

Figure 6.2. 1 Absorbance and photoluminescence spectra of synthesized (a) green emitting and (b) red emitting InP/ZnS quantum dots. Reprinted with permission from [90]. Copyright 2017 Royal Society of Chemistry.

Synthesized QDs have been embedded in KCl salt which is more convenient compared to other salts in terms of its less moisture retention capability [107]. The images of the red and green QD-salt have been presented with and without UV-illumination in Figure 6.2.2a and Figure 6.2.2b. Cd-free QDs-salt powder has been formed in its pellet form under pressure by hydraulic pressure equipment and the QD-pellet form has been presented under UV-illumination in Figure 6.2.2c.

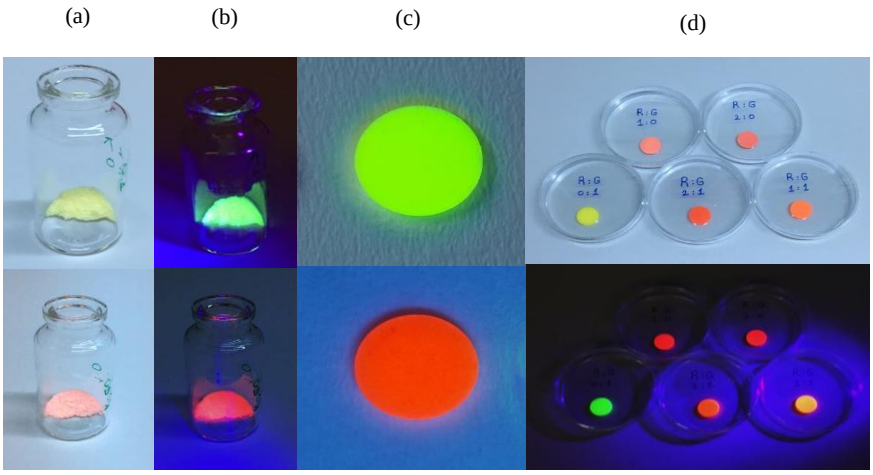

Figure 6.2. 2 Green and red quantum dot salt powder (a) without UV illumination, (b) with UV-illumination, (c) Cd-free only green and red QD-pellet under UV-illumination and (d) prepared mix pellet with different red and green QDs concentration without and with UV-illumination. Reprinted with permission from [90]. Copyright 2017 Royal Society of Chemistry.

Colloidal quantum dots suffer from a decrease in their quantum yield in their solid form. Keeping QDs' in solution optical properties as high as in the solid state is a very important step towards the realization and spread of future optoelectronics. In order to show the effectiveness of salt crystals as a protective medium, a degradation study was carried out. A pellet with a definite composition was prepared by following the same procedure explained throughout this study. For comparison, the same amount of QD solution was drop-casted on a glass microscope slide and the solvent was allowed to evaporate at room temperature. The pellet and drop-casted samples were placed and kept in fluorescence spectrometer for 72 hours in separate sessions to monitor the change in emission characteristics at ambient conditions, without continuous excitation. The spectrometer was equipped with a Xenon lamp as a steady state excitation source, coupled with a monochromator. The samples were excited at 375 nm and emitted photons were collected by a detector for every 30 minutes for the first 8 hours to inspect the expected initial sharp decrease in PL performance, followed by a 4 hour check for the rest of the test. As shown in Figure 6.2.3a, QDs embedded in pellets preserved the 75% of their initial PL intensity at the end of 72 hours. Drop-casted QDs, on the other hand, suffered a dramatic decrease down to 52% of the initial peak intensity.

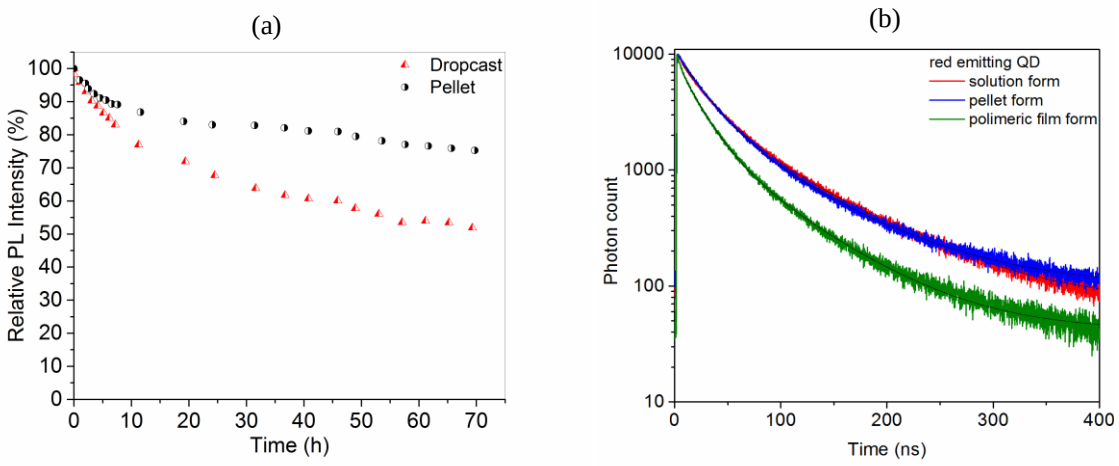

Figure 6.2. 3 (a) Change in PL peak intensity as a function of time for pellet and dropcasted samples (b) TRPL measurement of red emitting QD in different form. Reprinted with permission from [90]. Copyright 2017 Royal Society of Chemistry.

In addition to steady state photoluminescence intensity evolution with respect to time, we also characterized the lifetime of the QDs in solution form, same amount of QDs incorporated with KCl salt in the pellet form and in polymeric film (PMMA 10% in toluene) form. Figure 6.2.3b shows the emission kinetics of different forms of red emitting QDs. As compared with the in solution form of the QDs, the emission kinetics of the pellet form of red QDs did not change much. However, the lifetime of solution form of QDs changed from 45.88 ns to 32.59 ns in polymeric film form of QDs. The decline in the lifetime of the solution form in a way demonstrates the reduction in quantum efficiency with incorporation of polymer. The lifetimes and lifetime's parameters of different form of red emitting QDs are given in Table 6.2.1.

Tablo 6.2. 1 The lifetime analysis of red emitting QDs in their different forms. Reprinted with permission from [90]. Copyright 2017 Royal Society of Chemistry.

Red emitting QD	A_1	τ_1(ns)	A_2	τ_2 (ns)	$\tau_{average}$ (ns) (intensity)	$\tau_{average}$ (ns) (amplitude)
Solution form	3039.2±25.1	81.30±0.50	5122.1±70	24.87±0.35	62.10	45.88
Pellet form	2564.6±24.1	80.19±0.56	5407.5±66.1	25.45±0.31	58.25	43.06
Film form	1863±23.5	66.84±0.59	5026.9±72.2	19.89±0.28	45.93	32.59

Following the photo stability tests, in order to reveal emission kinetics and FRET energy transfer between donor and acceptor, we have blended green and red quantum dots as donor and acceptor pair in pellet form. With R:G defining the ratio of the red

and green emitting particles, the donor acceptor ratio has been defined as (0:1), (0.25:1), (0.35:1), (0.5:1), (1:1), (2:1), (0.25:0), 0.35:0), (0.5:0), (1:0), (2:0) for the investigation of the energy transfer among the pellet structure.

Emission kinetics of only donor and donor-acceptor pairs has been compared in Figure 6.2.4a by using time correlated single photon counting (TSCPC) decays. The lifetime of only donor and donor-acceptor pairs are given in Figure 6.2.4a and have been presented in Table 6.2.2. Average amplitude-weighted lifetime of only donor has been fit with two exponential fit parameters, calculated as 63.53 ns, whereas acceptor-donor pairs at donor emission wavelength have been calculated as 45.00 ns for R:G (0.25:1), 40.99 ns for R:G (0.35:1), 33.48 ns for R:G (0.5:1), 27.12 ns for R:G (1:1), 22.35 ns R:G (2:1). The maximum FRET efficiency, η, was calculated from Equation 6.2.1 as 65 % with and representing the lifetime of the donor with and without acceptor, respectively.

$$\eta = 1 - \frac{\tau_{DA}}{\tau_D} \tag{6.2.1}$$

The lifetime of acceptor with and without donor in the case of given acceptor concentrations from 0.25x to 2x have been demonstrated in Figure 6.2.4b. The largest increase of acceptor lifetime has been obtained by using 0.35x acceptor concentration. Emission kinetics of this sample in the presence of donor and absence of donor have been shown in Figure 6.2.4c. Figure 6.2.4d presents the measurement of steady state photoluminescence for only acceptor, only donor and donor-acceptor pair in the case of the ratio of (0.35:1) R:G. The photo of QD-pellet samples in case of (0:1), (0.35:1), (0.35:0) R:G ratio under UV-illumination was included in Figure 6.2.3d as an inset. The increase of intensity in the acceptor and the decrease in the steady state photoluminescence spectrum of the donor in Figure 6.2.4d result from FRET amongst donor and acceptor pair.

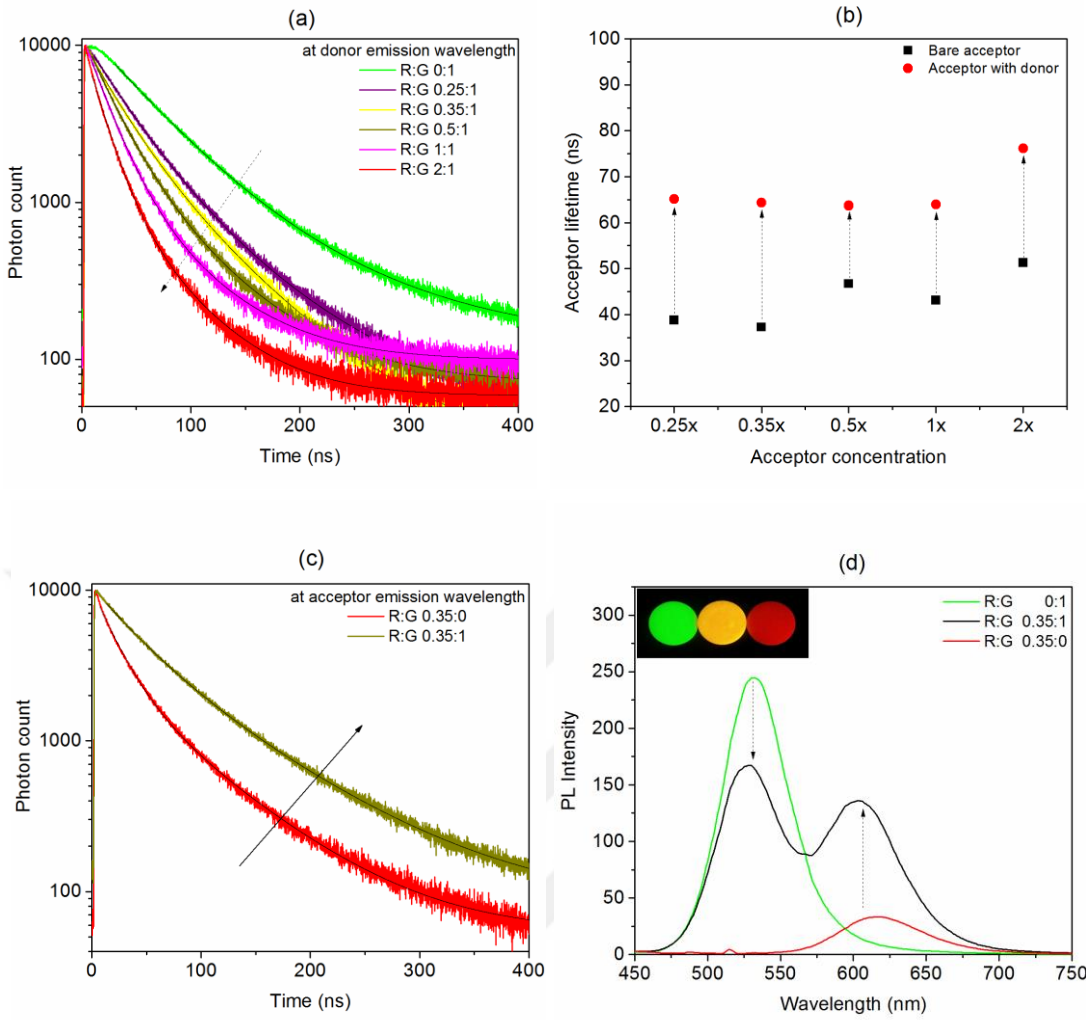

Figure 6.2. 4 (a) TSCPC decays of FRET analysis in pellet form with different changing green and red concentration ratio at donor emission wavelength, (b) The change of acceptor lifetime with respect to acceptor concentration, (c) Emission kinetics of R:G (0.35:0) and (0.35:1) concentration (without and with donor) at acceptor emission wavelength, (d) The steady state photoluminescence spectra of only donor, only acceptor and donor with acceptor. Reprinted with permission from [90]. Copyright 2017 Royal Society of Chemistry.

Tablo 6.2. 2 The lifetime components (amplitudes, lifetime coefficient and amplitude weighted lifetimes) for donor only pellet and donor with acceptor pellet at donor emission wavelength. Reprinted with permission from [90]. Copyright 2017 Royal Society of Chemistry.

At donor emission wavelength Red:Green	A_1	τ_1(ns)	A_2	τ_2 (ns)	$\tau_{average}$ (ns) (intensity)	$\tau_{average}$ (ns) (amplitude)
0:1	1345.4±17.8	119.61±1.23	6103.3±39.7	51.17±0.31	74.44	63.53
0.25:1	2051.1±23.3	80.28±0.60	6745±53.7	34.43±0.25	53.45	45.12
0.35:1	2747.7±28	68.05±0.45	6262.9±63.4	29.13±0.28	48.83	40.99

0.50:1	1866.2±25.1	64.90±0.61	6606.4±64.4	24.61±0.23	41.81	33.48
1:1	1407.4±24.7	58.97±0.73	6536.9±69.6	20.26±0.20	35.17	27.12
2:1	1117.1±23.4	51.57±0.75	5244.4±73.1	16.16±0.21	30.49	22.35

Tablo 6.2. 3 The lifetime components (amplitudes, lifetime coefficient and amplitude weighted lifetimes) for acceptor only pellet and donor with acceptor pellet at acceptor emission wavelength. Reprinted with permission from [90]. Copyright 2017 Royal Society of Chemistry.

At acceptor emission wavelength Red:Green	A_1	τ_1(ns)	A_2	τ_2 (ns)	$\tau_{average}$ (ns) (intensity)	$\tau_{average}$ (ns) (amplitude)
0.35:0	2425.7±25	72.82±0.54	5286.6±75.9	20.94±0.30	52.83	37.25
0.35:1	3801.2±25.1	92.93±0.47	4267.2±52.9	38.84±0.49	75.65	64.32

In order to study the potential of our QD pellets for white light generation, we used a commercially available InGaN blue LED as an excitation source, emitting at 450 nm. Each pellet was placed on the blue LED and the transmitted light was collected from the surface by using a fiber to inspect and calculate the spectral properties of generated white light.

For varying amounts of red QD with respect to constant green QD content, figure of merits of the generated white light are given in Table 6.2.4. The most prominent pellet was determined as having 0.35:1 red to green ratio with color coordinates (x,y) (0.4559, 0.4452), along with a 82.5 CRI value. The CCT and LER complies with the high quality white light parameters with <4000K (3014.2 K), and >300 (368.5) values, respectively. All color coordinates listed in Table 6.2.4 are shown on CIE 1931 color space chromaticity diagram in Figure 5.

Tablo 6.2. 4 Characterization results of the generated white light with various pellets. Reprinted with permission from [90]. Copyright 2017 Royal Society of Chemistry.

Red	Green	Amp	x	y	LER	CCT (K)	CRI
0.25	1	10mA	0.3846	0.4712	424.1	4406	66.2
0.35	1	10mA	0.4559	0.4452	368.5	3014.2	82.5
0.50	1	10mA	0.4926	0.3852	318.0	2120.9	76.9

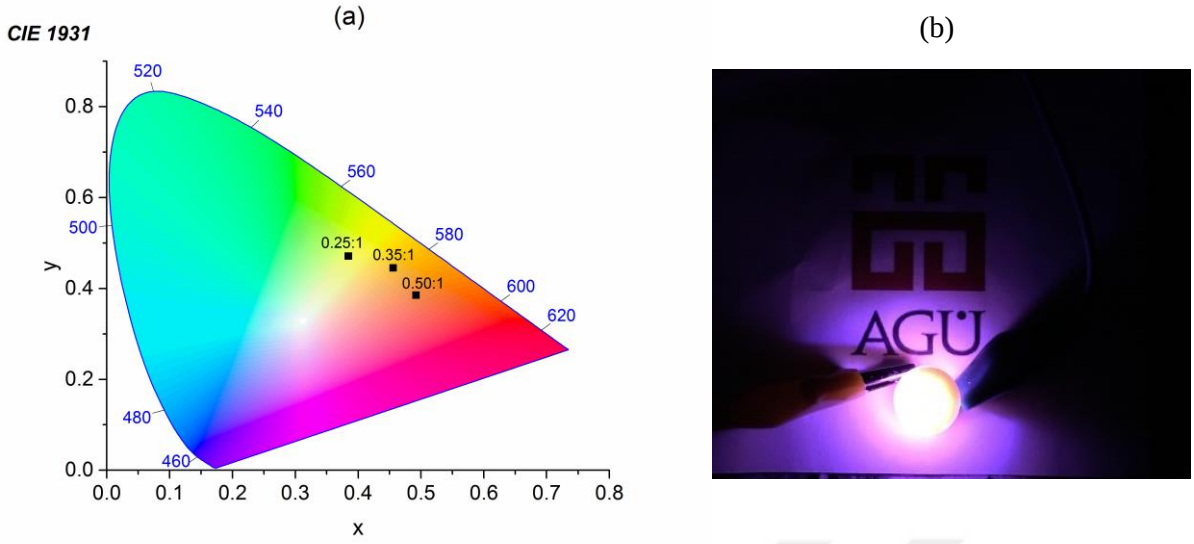

Figure 6.2. 5 (a) Color coordinates of prepared pellets on CIE 1931 color space chromaticity diagram (b) Generation of white light by stacking the 0.35:1 pellet on blue-LED. Reprinted with permission from [90]. Copyright 2017 Royal Society of Chemistry.

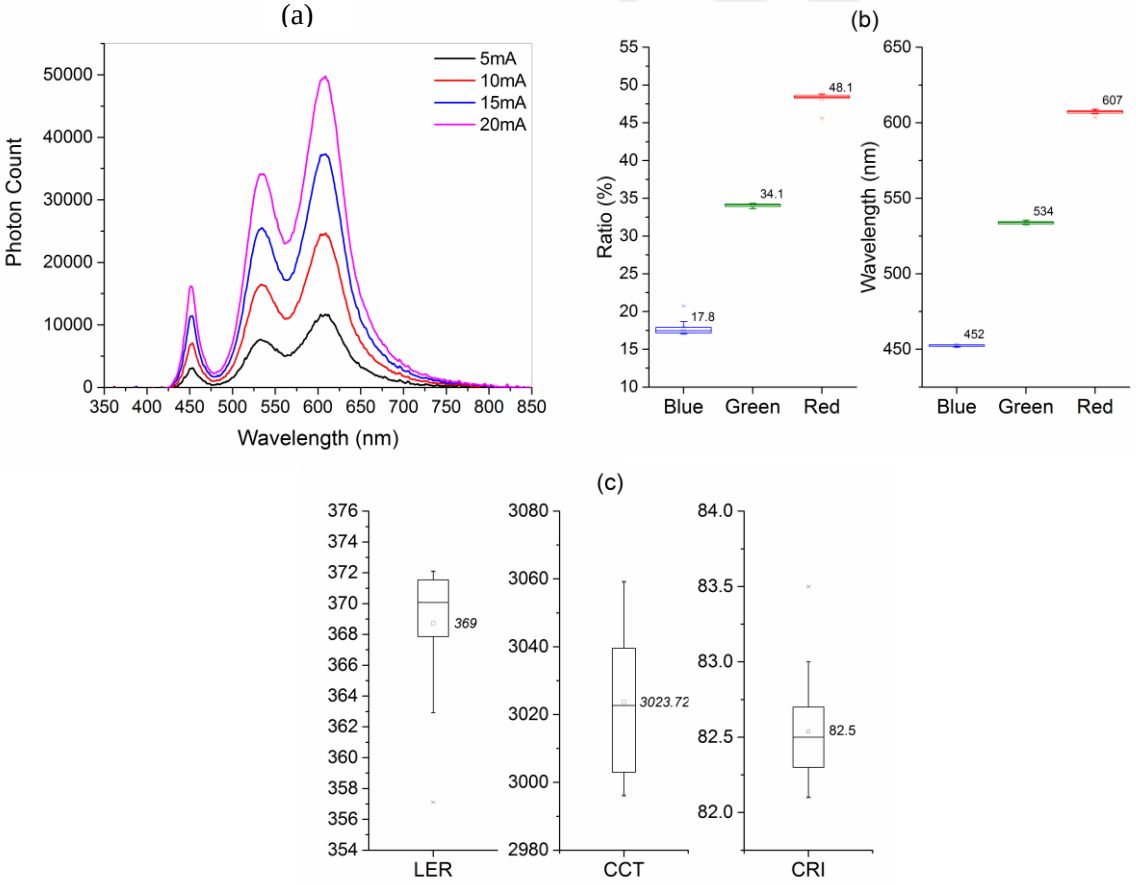

Figure 6.2. 6 (a) White light spectra at various blue-LED current levels (b) The deviation of relative color ratios and peak emission wavelengths with varying backlight brightness (c) The deviation of LER, CCT, and CRI with varying the backlight brightness. Reprinted with permission from [90]. Copyright 2017 Royal Society of Chemistry.

In order to determine the effect of the back-illumination on the best performed 0.35:1 pellet, we varied the brightness of the blue LED by driving a current from 3 to 20 mA via Keithley-2400 source-meter and collected the transmitted light with a fiber to generate the spectral output. Figure 6.2.6a shows the generated white light spectrums for various blue-LED luminosity values, with an elevating intensity versus increasing brightness pattern. However, relative color ratio and peak emission wavelengths remained unchanged with respect to increasing brightness. The deviations and mean values are presented as a box plot in Figure 6.2.6b. Two of the high quality white light requirements, CCT and LER, remained in acceptable boundaries. Minute variations in the performance of light in terms of CRI, CCT and LER are exhibited in Figure 6.2.6c.

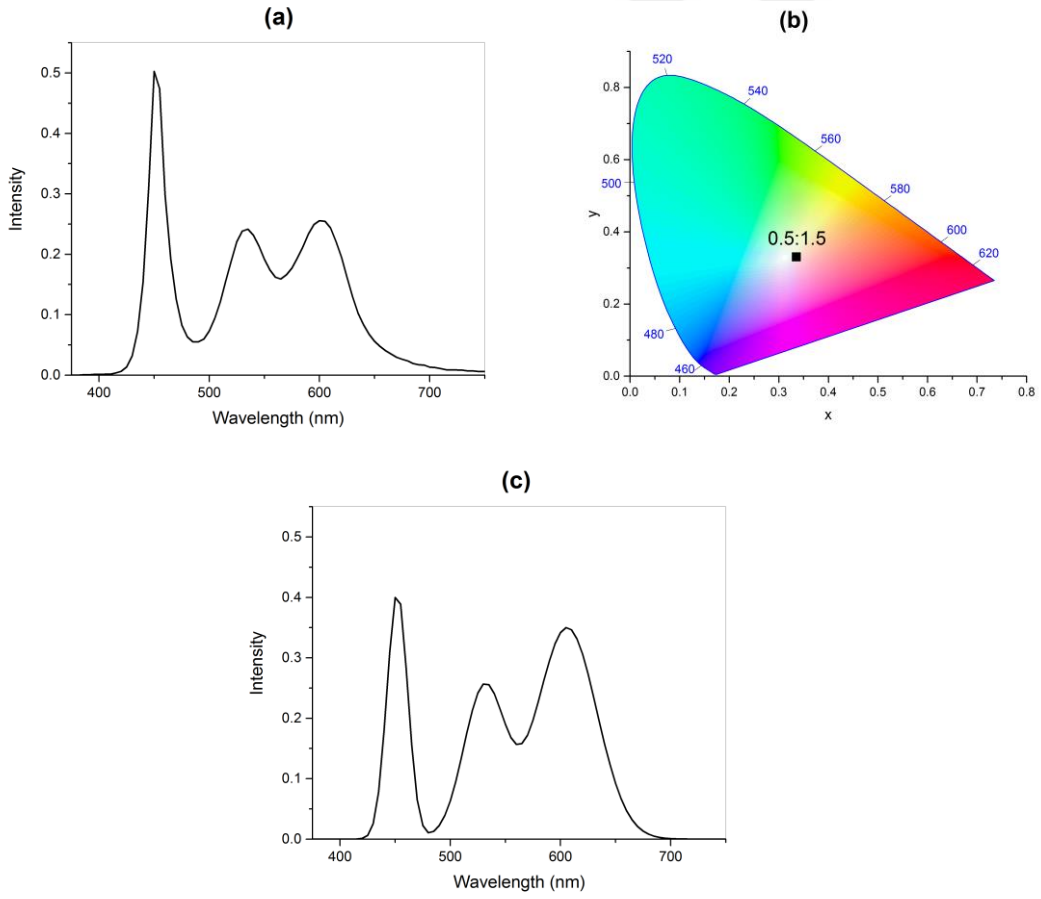

Figure 6.2. 7 (a) The spectrum of our pellet (0.5:1.5) (b) The white light coordinate of our pellet on CIE 1931 color space (c) The spectrum of maximum achievable CRI based on simulation. Reprinted with permission from [90]. Copyright 2017 Royal Society of Chemistry.

In order to determine the maximum possible performance of the white light that can be generated in this study, we conducted a theoretical calculation by modifying spectral parameters in compliance with experimental boundaries. The variation in peak emission wavelengths (and intervals) were 451-453 nm (0.5 nm), 531-537 nm (0.5 nm), and 600-606 nm (1 nm) for blue, green, and red, respectively. FWHM values were 20.5-22.0 nm, 44.0-45.5 nm, and 63.5-65.5 nm with 0.5 nm intervals for blue, green, and red, respectively. Relative color ratios were allowed to take any set of values, except zero, with 5% increments, which adds up to 100. The permutation of these variables created 6 million scenarios. By applying one of the conditions of high quality white light requirements (CCT<4000K) to filter the results, the maximum achievable CRI value was found to be 88.0. The peak emission wavelength, FWHM, and relative intensity ratios were 453 nm, 22 nm, 40% for blue, 531 nm, 44 nm, 25% for green and 606 nm, 63.5 nm and 35% for red component. Figure 6.2.7c shows the spectrum of the simulated case. The LER and CCT values for the same parameter set were 346.4 lm/W_{opt} and 3725.3K, respectively.

In the light of simulation results, a new pellet composition was determined as (0.5:1.5) R:G ratio, which maximizes the white light performance. The spectrum of this pellet excited by the same blue LED in this study is given in Figure 6.2.7a. The color quality parameters of generated white light are 84.7 for CRI, 5347.5 K for CCT, and 324.3 lm/W_{opt} for LER. Also, for the potential use of this pellet in display applications we calculated the ratio of color gamut of our pellet to NTSC area to be 85.6% with x=0.3356 and y=0.3312 color coordinates. The white light coordinates of this pellet is marked on CIE 1931 in Figure 6.2.7b.

6.3 Summary

In summary, we study the synthesis of highly efficient and narrow emission bandwidth InP/ZnS quantum dots and demonstrate their pellet form, and reveal the excitonic interaction amongst these Cd-free pellets for the first time. A FRET efficiency level of 65% has been achieved from the donor to acceptor pairs and optimizing the donor acceptor ratio within the pellet structure, an efficient white light emitting diode possessing CRI level of 84.7, CCT of 5347.5 K and luminous efficacy of optical radiation value of 324.3 lm/Wopt has been presented. The utilization of these pellets

and understanding excitonic interactions within them will pave the way for next generation advanced optoelectronics.

6.4 Methods

The green and red QDs have been synthesized following the modified recipes in literature [45], [66], [70], [72], [75]. All reagents were purchased from Sigma Aldrich with their highest purity available.

6.4.1 Synthesis of green emitting QDs

Initially, alloyed core was prepared by addition of 0.12 mmol $InAc_3$, 0.36 mmol myristic acid (MA), 6mLoctadecene (ODE) and loaded into three-necked flask fitted with valves and a septum. Under vigorous stirring and vacuum, solution was heated to 95 °C and held at this temperature for 1 hour. After getting clear solution, the system was cooled down to room temperature. In the next step, 0.5 mmol Zn-stearate and 0.025 mmol (1-dodecanethiol) DDT were added to solution and the obtained mixture was heated to 220 °C under argon atmosphere. At the precise moment of solution reaches to 220 °C, 0.085 mmol Tris(trimethylsilyl)phosphine (TMSP) was rapidly injected into flask. Temperature was set to 285 °C and growing of nanocrystals occurred at 285 °C for 10 min. Then, solution was cooled down to 230 °C in ambient temperature and 1mLof mixture from stock solution (1.2 mmol Zn-stearate and 2.4 mmol DDT and 6mLODE in a different neck under Ar gase at 180 °C) was slowly injected into the solution including core QDs. After 15 min at 230 °C, 1mLof mixture was added again and this step was repeated for three times. Totally, 4mLinjection of stock solution was completed, followed by addition of 2.8mLmixture of stock solution. After 30 min, the system was allowed to cool down to room temperature and cleaning procedure was carried out to remove excess ligands on the newly synthesized QDs. Hexane by half volume of QD solution was added to a centrifuge tube to get rid of by-products with the help of centrifugation at 5000 rpm for 15 min. Following, acetone and methanol were added to the QD solution to precipitate the nanoparticles (centrifugation at 5000 rpm for 10 min). The obtained precipitate was dried at room temperature, dissolved in fresh hexane and kept at +4 °C in solution.

6.4.2 Synthesis of red emiting QDs

Trioctylphosphine (TOP) capped InP/ZnS nanocrystals were synthesized by using hot injection method modified from literature. 0.45 mmol $InCI_3$, 2.2 mmol $ZnCI_2$, 0.033 mmol DDT and 5mLoleylamine were loaded into triple neck flask. Under vacuum, the mixture was heated up to 120 °C and held at this temperature for 1 hour. Then, system was filled up with Ar gas and heated up to 180 °C. Once the system reached to specified temperature, 250 μL tris dimethylamino phosphine was quickly injected into solution. 20 min at 180 °C was efficient for the formation of nanoparticles (first stage). After generation of the core QD (main solution), next steps were followed to create shell structure which passivates and protects the core QD. At first, 1 mL TOP-S from 2.2 M stock solution (0.72 g Sulfur in 10mLTOP prepared in glovebox) was injected into triple neck and waited for 40 min. Subsequently, the system was heated up to 200 °C. 1 hour later, 4mLof Zn-Ste/ODE stock solution (2g Zn-Ste in 6mLODE in triple neck under Ar gas) was injected into main solution and heated up to 220 °C. After 30 min, 1 mL TOP-S from 2.2 M stock solution was injected into main solution again and temperature was increased to 240 °C and kept for 20 min. Next, 2 mL Zn-Ste/ODE from stock solution was added into main solution and kept for 20 min at 260 °C. After loading 0.7 mL TOP-S (2.2 M), mixture was stirred at 280 °C for 20 min. At last, 2 mL Zn-Ste/ODE was injected and after 15 min the system was cooled down to room temperature. The cleaning procedure was applied as the same in green QD synthesis without using methanol.

6.4.3 Preparation of Quantum Dot-Salt Pellet

Proportions of green and red quantum dot solutions were determined with maximum peak of PL intensities. And according to this ratio of red and green QDs were adjusted as 0:1, 1:1, 1:0, 2:1, 2:0, 0.25:0, 0.25:1, 0.35:0, 0.35:1, 0.5:0, 0.5:1.

0.5 g KCl was mixed with 1.5mLn-hexane and determined amount of QDs were added to this mixture. Suspension of KCl and QDs were mixed for 30 minutes and followed by solvent evaporation under vacuum. As a result, QDs are spatially positioned on KCl crystals. Prepared mixtures were later exposed to 10 tons of pressure via hydraulic press to form the pellets.

6.4.4 Characterizations

Photoluminescence and absorption characterizations were carried out with using Agilent-Cary Eclipse fluorescence spectrophotometer and UV-Vis spectroscopy Thermo Genesys 10S spectrometer respectively. TSCPC measurements were performed by Pico Quant FluoTime 200 equipped with 375 nm pulsed laser diode.

Chapter 7

7. CdSe/ZnS Core/Shell Nanoplatelets

The sub-chapter of this thesis is based on the publication "Highly Stable, Near-Unity Efficiency Atomically Flat Semiconductor Nanocrystals of CdSe/ZnS Hetero-Nanoplatelets enabled by ZnS-Shell Hot-Injection Growth," **Y. Altintas,** U. Quliyeva, K. Gungor, O. Erdem, Y. Kelestemur, E. Mutlugun, M. V. Kovalenko, and H. V. Demir, *Small*, DOI: 10.1002/smll.201804854, 2019. Reprinted with permission from [117]. Copyright 2019 WILEY-VCH Verlag GmbH & Co. KGaA, Weinheim.

7.1 Introduction

Nowadays, chemically synthesized semiconductor nanocrystals (NCs) have become an important and exciting class of nanomaterials. These free-standing NCs are obtained with the colloidal synthesis, enabling unique opportunities to precisely control their size, shape, structure and composition [118]. To this end, in the development of NC syntheses, a major breakthrough came in the middle of 90's when the hot-injection (HI) crystal growth technique was demonstrated colloidally to produce monodisperse Cd-based NCs [12]. Thus far, such NCs of spherical quantum dots (QDs) have been extensively studied and exploited [96], [119]–[122]. Previously, different than being spherical in shape, a new family of NCs that are atomically-flat and of only few monolayers in thickness was obtained with excellent control over their quasi two-dimensional (2D) structure [123]. This type of flat NCs as commonly known as semiconductor nanoplatelets (NPLs), or alternatively as colloidal quantum wells (QWs), offer new possibilities based on their one-dimensional tight quantum confinement characteristics in colloidal optoelectronics [124]. For example, these NPLs having magic-sized vertical thickness exhibit ultra-narrow emission with none (or reduced)

inhomogeneous broadening, accompanied with giant oscillator strengths, large absorption cross-sections and molar extinction coefficients when compared to QDs [124]–[126]. All these properties make NPLs highly promising candidates for high-performance colloidal lasing as well as possibly other colloidal optoelectronic applications [127]–[129]. Nevertheless, there are important and challenging problems that need to be resolved related with their stability to ensure extended shelf-lifetime, efficient light emission and lasing, which involves high operating temperatures and high photon energy excitations [130].

An effective method for tackling the stability issue is the growth of a semiconductor layer around the core NPLs. This approach generally helps to reduce the surface nonradiative recombination sites by passivating surface traps, leading to increased quantum yield and decreased emission blinking at a single particle level [131]–[135]. Among the shell structures used for CdSe-core NPLs, the most notable ones demonstrated thus far include CdS[131], [136]–[138] and ZnS[135], [138] which result in quasi type-II and type-I band alignment structures, respectively. In the past few years, research on the core/shell NPLs has concentrated mostly on the colloidal synthesis of CdSe/CdS core/shell NPLs owing to the smaller lattice mismatch between these materials and the resulting quasi-type II nature of electronic structure enabling highly tunable excitonic features [134], [136]–[138]. For example, Rossinelli et al. have recently reported the uniform growth CdS shell on CdSe NPLs at higher temperatures resulting in narrower emission linewidth (~20 nm) with suppressed blinking and moderately high photoluminescence quantum yield (QY) of 55-60% [137]. However, the little band-offset for electrons in CdS shell necessitates a new shell structure with a large band-offset, thus providing enhanced environmental stability and high stability under high-temperature working conditions [139].

Such a large band-offset can be achieved with the growth of ZnS shell, which can substantially reduce trap sites. The previous studies on the ZnS shell growth commonly relied on the so-called colloidal atomic layer deposition (c-ALD) and these CdSe/ZnS core/shell NPLs possess very low QY levels in the range of 1 to 4% [135], [138]. In addition to the lower QY, conventional c-ALD approach is time-consuming and a large amount of precursor is wasted during its tedious synthesis protocol. Also, an undesirable homogenous nucleation of shell material is easily induced if the cleaning

process is not performed several times after each semi-layer. Moreover, the resulting core/shell NPLs suffer from the poor colloidal stability after multiple cleaning steps. In this context, hot-injection shell growth approach potentially offers solutions to synthesize highly uniform and crystalline CdSe/ZnS core/shell NPLs together with narrow emission bandwidth, improved QY and enhanced thermal stability if performed high enough temperatures. The most recent work on these NPLs has been reported by Polovitsyn et al., employing the ZnS shell growth at moderate temperatures of 373-423 K. The reported QY of that previous work is 50-60%, which has thus far been the highest value attained in the literature for CdSe/ZnS core/shell NPLs [135]. However, there had been no report on the growth on the ZnS shell beyond 500 K to date, which would enable much further improved efficiency and enhanced stability at the same time, which is desired for high-performance colloidal optoelectronic applications.

Here we present the synthesis of CdSe/ZnS core/shell NPLs with QY close to unity (98%), enabled by the ZnS shell hot-injection growth at a high temperature of 573 K, reaching unprecedented levels of stability and achieving superior optical gain performance. These CdSe/ZnS core/HI-shell NPLs are synthesized without any side-product and with the benefit of a facile purification and isolation procedure, as compared to those of the c-ALD technique. In this work, the resulting QY of the core/HI-shell NPLs ranges from 85% to a record level of 98% depending on the shell precursors as well as the reaction conditions, which is attained reproducibly.

In addition, we observe that the thermal stability is greatly enhanced by using the HI shell growth approach beyond 500 K. By systematically conducting thermal tests under ambient air conditions which induce additional degradation, we observe that the thick-shell CdSe/ZnS core/shell NPLs completely recover their initial PL intensity (100% PL recovery) during a heating cycle from 300 to 400 K while exhibiting 76% PL recovery for the range of 300 to 525 K. These HI thick-shell sample also exhibits the best performance in UV stability tests and preserves their higher QY even after multiple cleaning steps. Previously, the thermal stability of different NPLs was reported by Rowland et al. for CdSe/CdS core/shell NPLs under vacuum [134]. In this previous study, as a benchmark, the heating cycle up to 450 K yields fully reversible PL intensity under vacuum for CdSe/CdS core/shell NPLs with 6 monolayers of CdS shell that was produced using the c-ALD method, however, the PL intensity was found to drop to 60%

at the end of heating cycle up to 500 K. These results show that the CdSe/ZnS heteronanoplatelets synthesized herein exhibit superior thermal stability compared to their predecessors.

Finally, we have studied the optical gain performances of HI CdSe/ZnS core/shell heteronanoplatelets. With their enhanced optical properties and superior thermal stability, we achieve low gain threshold values as low as 6.7 μJ cm^{-2} under femtosecond-pulsed excitation. Superior thermal stability is also observed in optical measurements for HI NPLs. Films of HI NPLs annealed at 400-500 K showed significantly lower ASE threshold values. Being a major limitation for practical lasing applications, the substantially improved thermal stability of HI CdSe/ZnS core/shell NPLs will be an important step for the realization of lasers with colloidal nanocrystals as active gain medium.

7.2 Result and Discussion

We utilized and modified the hot injection shell growth recipe reported by Rossinelli et al. for quasi-type-II CdSe/CdS core/shell NPLs [137]. In our study, Zn-acetate and octanethiol were used as Zn and S precursors for ZnS shell coating, respectively. The shell growth was carried out at 300 ˚C due to the effective utilization of octanethiol, which has relatively low reactivity at low temperature. During the synthesis, aliquots were taken at regular intervals to characterize the resulting optical properties. The PL and absorbance spectra of CdSe/ZnS core/shell NPLs using different shell growth time are presented in Figure 7.2.1a.

With the formation of ZnS shell, strongly red-shifted excitonic features are observed. The red shift in PL emission is recorded as 75 nm at 5 min, 98 nm at 30 min, 112 nm at 60 min, 116 nm at 120 min, and 120 nm at 180 min with respect to the peak emission wavelength of core NPLs (~513 nm). In addition to the delocalization of electron and hole wavefunctions to the whole core/shell structure, the change in the effective dielectric constant contributed to the observed strongly red-shifted PL behavior, which is not common for semiconductor NCs having Type-I electronic structure [135]. The full-width-half-maximum (FWHM) of the PL emission during the shell growth first increased to 22 nm during the first 30 min growth time, then increased to 26 nm at 90 min, and finally reached 29 nm at 180 min.

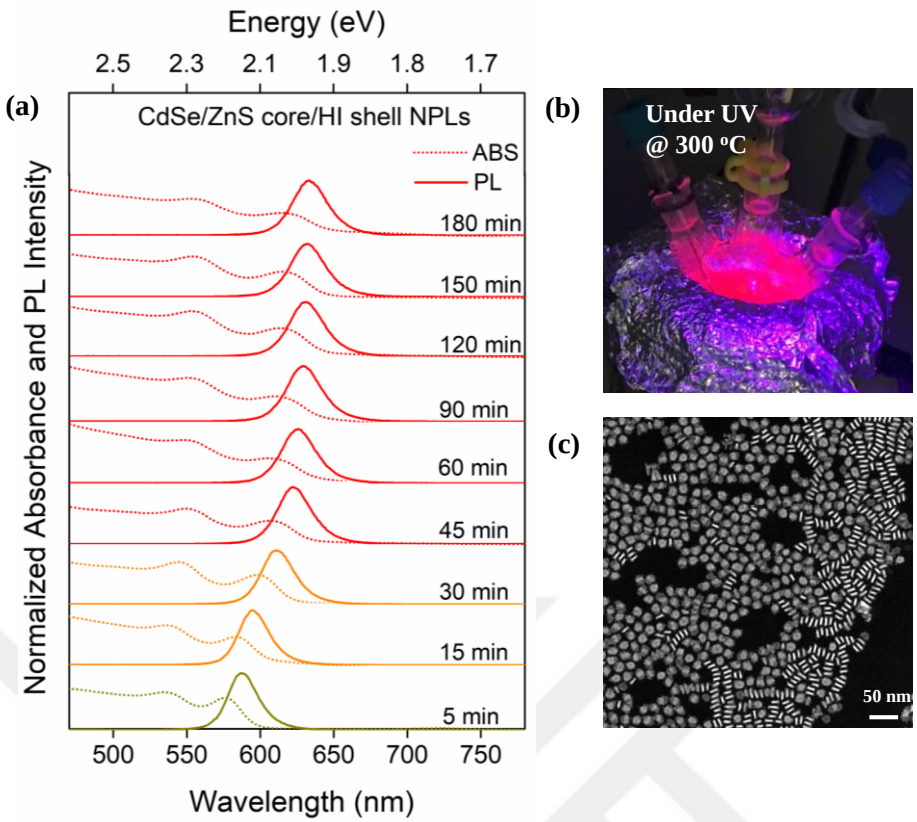

Figure 7.2. 1(a) Normalized absorbance and photoluminescence spectra of CdSe/ZnS core/hot injection shell nanoplatelets (core/HI shell NPL) samples parametrized with respect to the shell growth time (b) photographs of a core/HI shell NPL sample at 300 ˚C with UV illumination during the synthesis. This unique continuous emission of the synthesized NPL well at 300 ˚C indicates their high thermal stability unlike standard NPL growth where the emission fully quenches at high temperature. (c) TEM image of the synthesized core/HIS NPL (scale bar: 50 nm). Reprinted with permission from [117]. Copyright 2019 WILEY-VCH Verlag GmbH & Co. KGaA, Weinheim.

This broadening in the emission linewidth is attributed to the enhanced exciton-phonon coupling within these core/shell heterostructures, increased strain with the formation ZnS shell having large lattice mismatch between the CdSe core and possibly slight thickness variation within the NPLs.[135], [140] We have also measured the QY of the core/shell NPLs depending on the shell growth time. In the first 30 min of the growth time, QY of sample increased dramatically from 4% (2.5 min) to 60% (30 min), suggesting the effective passivation of surface trap sites with the ZnS shell. Then, QY of the sample reached a maximum value of 70% at 60 min, and from 60 min to 180 min of the shell growth time, QY of the sample decreased from 70% to 50%, which is expected due to increased strain and/or defect sites with the formation of thicker ZnS shell. Figure 7.2.1b shows the photographs of CdSe/ZnS core/HI shell NPL monitored at 300 ˚C, with PL emission under UV illumination, indicating the thermal stability of as-synthesized HI-shell NPLs. TEM image of the hot injection sample is given in Figure

7.2.1c. The thickness of the synthesized NPLs is approximately 4.35 ± 0.56 nm, measured from TEM images.

To further improve the quality of the synthesized CdSe/ZnS core/HI-shell NPLs, we studied the synthesis conditions by systematically tuning the shell growth time, precursors and ligand concentrations. For the synthesis, we employed oleic acid (OA) and oleylamine (OLA) as the ligand. OA was added at the beginning of the synthesis together with Zn precursor, octadecene (ODE) and CdSe core NPL. First, we investigated the effect of OA on the resulting optical and structural properties of core/shell NPLs by using three different amounts of OA (100 µL, 500 µL, and 1000 µL) with the constant volume (500 µL) of the OLA. The absorbance, PL, time-resolved fluorescence (TRF) decay curves and TEM images of the samples are given in Figures 7.2.2 and 7.2.3.

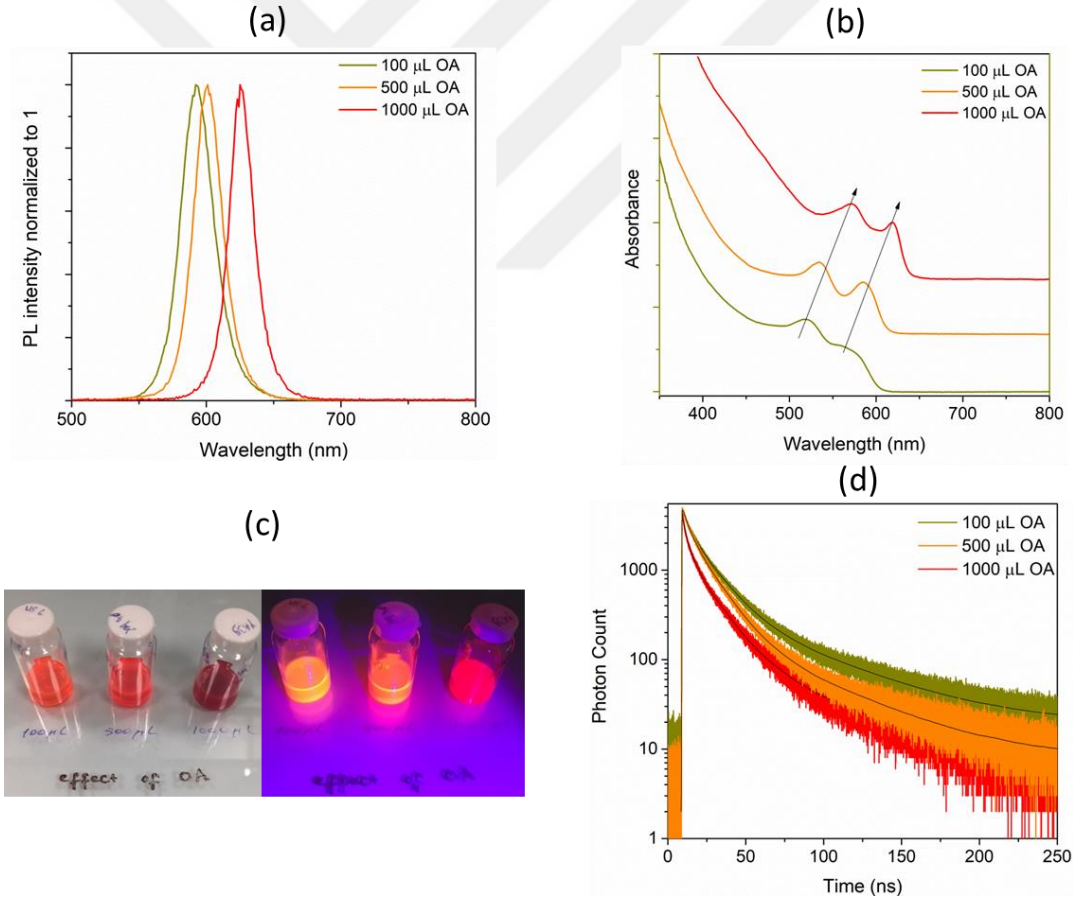

Figure 7.2. 2 a) PL Intensity, b) Absorbance spectra of the samples according to the different amount of oleic acid. c) Photographs of the samples which are obtained by varying amount of the OA are presented with and without UV illumination d) Time resolved photoluminescence decays of samples which are synthesized by using 100 µL, 500 µL and 1000 µL of OA. Reprinted with permission from [117]. Copyright 2019 WILEY-VCH Verlag GmbH & Co. KGaA, Weinheim.

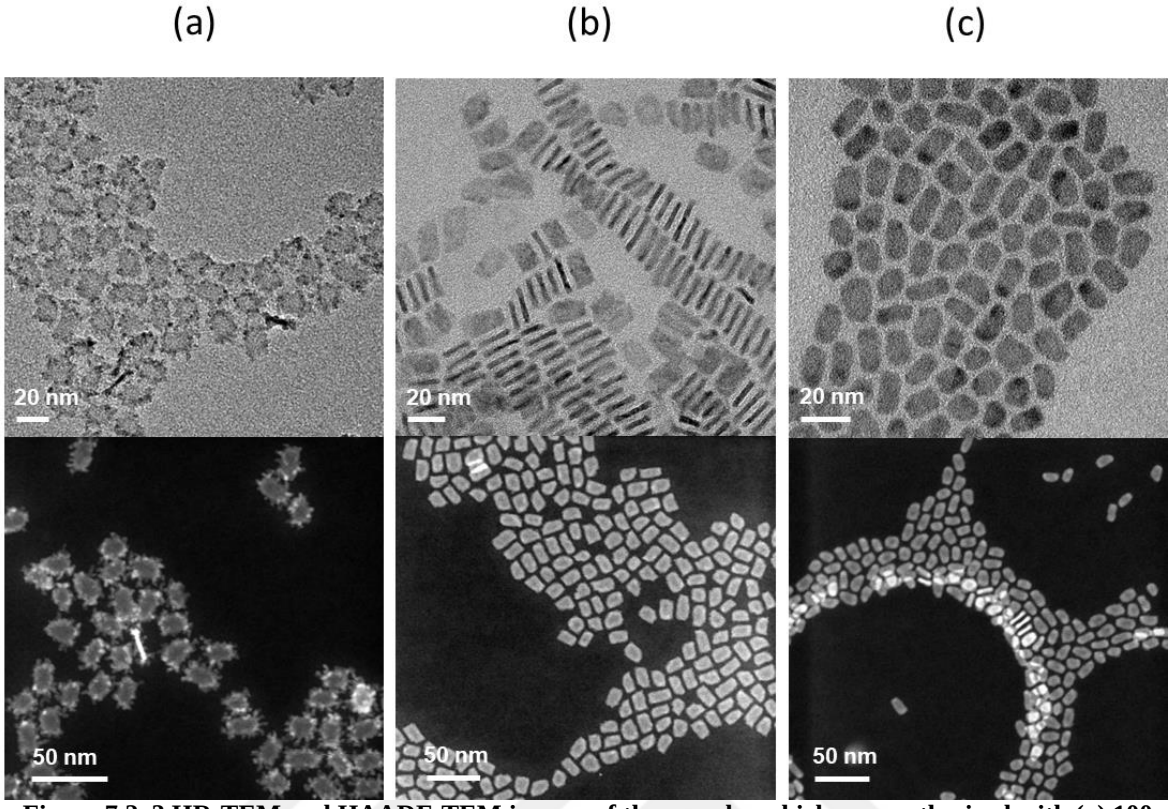

Figure 7.2. 3 HR-TEM and HAADF-TEM images of the samples which are synthesized with (a) 100 µL, (b) 500 µL and (c) 1000 µL of OA. Reprinted with permission from [117]. Copyright 2019 WILEY-VCH Verlag GmbH & Co. KGaA, Weinheim.

The excitonic features of the resulting core/shell NPLs are further redshifted with the increased amount of OA, suggesting the preferential growth in the vertical direction and resulting in further red-shifted excitonic features. This is also verified with the measured thicknesses from TEM images and the thickness of the NPLs increased with increasing the amount of OA from 2.66 ± 0.26 nm (for the case of 100 µL OA) to 4.07 ± 0.38 nm (for the case of 1000 µL OA). The PL emission peak changed from 592 to 602 nm and finally to 625 nm with respect to the used amount of OA, while the QYs of the samples are 75%, 85% and 56%, respectively, as presented in Table 7.2.1.

Table 7.2. 1 . Quantum yield, peak emission wavelength and full-width-at-half-maximum (FWHM) values depending on the OA amount. Reprinted with permission from [117]. Copyright 2019 WILEY-VCH Verlag GmbH & Co. KGaA, Weinheim.

Amount of OA	QY (%)	Wavelength (nm)	FWHM (nm)
100 µL	75	592	28
500 µL	85	602	24
1000 µL	56	625	21

From the analyses of the HR-TEM and HAADF-TEM images of these samples, uniform and homogeneous shell growth was found to be achieved using 500 µL amount of OA. From the TRF measurements, the amplitude-averaged fluorescence lifetimes (τ_{av}) of core/shell NPLs are calculated by fitting with multi-exponential decay functions due to their complex decay kinetics. We observed continuously decreased lifetimes from ~13.9 to 6.0 ns with increasing the amount of OA (Table 7.2.2).

Table 7.2. 2 Time resolved fluorescence measurement fit data of the samples which are synthesized by using 100 µL, 500 µL and 1000 µL of OA. Reprinted with permission from [117]. Copyright 2019 WILEY-VCH Verlag GmbH & Co. KGaA, Weinheim.

	τ_1 (ns)	Fractional intensity	τ_2 (ns)	Fractional intensity	τ_3 (ns)	Fractional intensity	τ_4 (ns)	Fractional intensity	τ_{avg} (ns)
100 µL OA	46.9	37.0%	13.2	57.6%	2.59	5.33%	-	-	13.9
500 µL OA	39.4	27.8%	12.1	65.9%	2.63	6.33%	-	-	11.7
1000 µL OA	39.5	28.0%	12.2	55.7%	2.91	12.8%	0.49	3.46%	5.96

The fluorescence decay curves are mainly composed of two exponential decays with lifetimes of 46-40 and 13-12 ns. For the case of the core/shell NPLs synthesized with 1000 µL of OA, we observed an additional lifetime component of 0.5 ns. This component might be attributed to nonradiative decay processes and explained the observed lower QY of the sample [141].

Etching of the CdSe core NPLs at higher temperatures within the presence of OLA has been already reported [137]. Therefore, during our synthesis, we introduced OLA at later stages to reduce the effect of etching. Also, we observe the formation of rough surfaces from the TEM images having thicker shell at the edges and thinner shell at the center parts (Figure 7.2.3 and 7.2.5). This might imply a distinct growth mechanism for the shell layers, starting mainly from the sides and covering the larger surfaces.

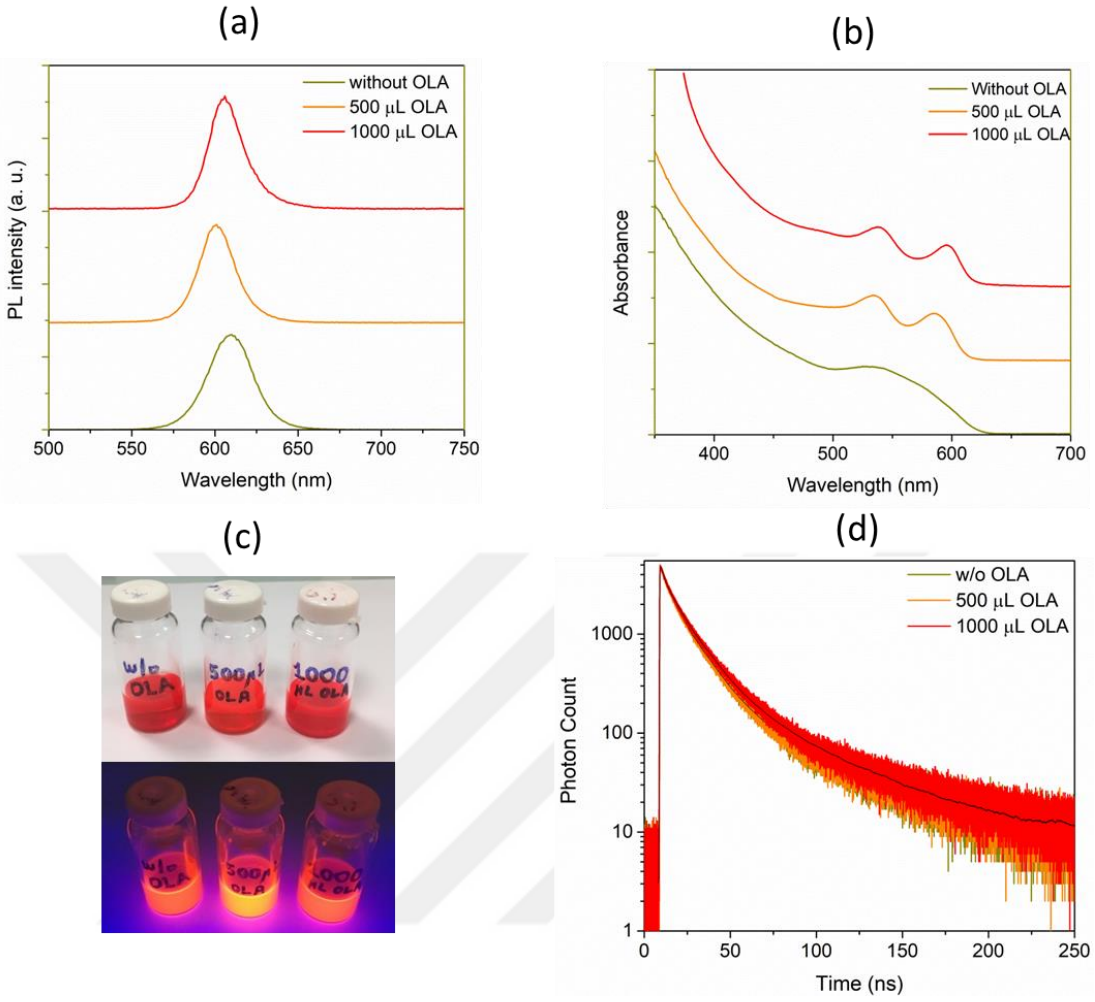

Figure 7.2. 4 . a) PL Intensity, b) Absorbance graphs obtained for various amount of oleylamine (OLA), c) with and without UV illumination photographs of the samples which are synthesized with different OLA volumes, d) Time resolved photoluminescence decays of samples which are synthesized by using without, 500 µL and 1000 µL of OLA. Reprinted with permission from [117]. Copyright 2019 WILEY-VCH Verlag GmbH & Co. KGaA, Weinheim.

This might imply a distinct growth mechanism for the shell layers, starting mainly from the sides. In our experiments we observed that the etching of the core NPLs does not only result from the OLA, but also due to the high temperature. Three different amounts of OLA were used in the synthesis as none, 500 µL and 1000 µL of OLA together with 500 µL of a constant amount of OA. The absorbance, PL and TRF decay curves are given in Figure 7.2.4. In the absence of OLA, QY of the sample decreased to 69% and FWHM of the sample increases to 31 nm. The heavy- and light-hole transitions in absorbance spectra do not resolve clearly when OLA is absent in the reaction, suggesting the non-uniform growth of ZnS layers. With the addition of OLA,

the resulting core/shell NPLs exhibit enhanced QY with well-resolved excitonic features (Table 7.2.3). While QY of the sample synthesized using 500 µL of OLA (~85%) is slightly higher than that synthesized with 1000 µL of OLA (~82%), FWHM of both the samples are the same as 24 nm.

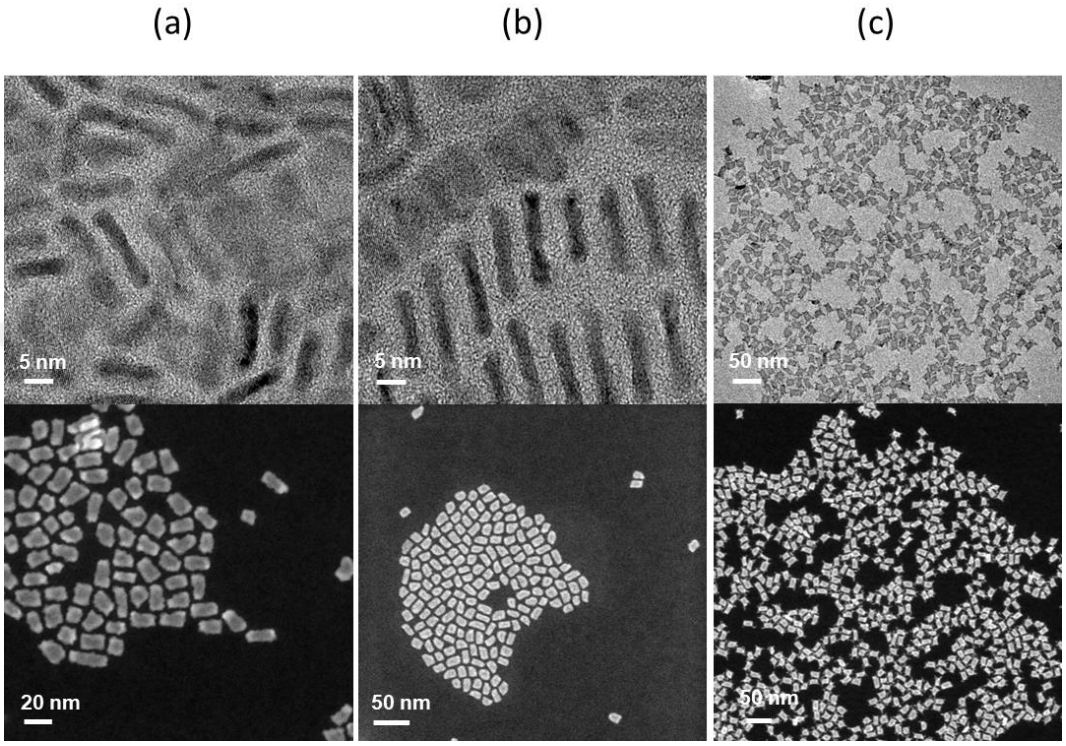

Figure 7.2. 5 HR-TEM and HAADF-TEM images of the samples which are synthesized (a) without, (b) 500 µL, (c) 1000 µL of OLA. Reprinted with permission from [117]. Copyright 2019 WILEY-VCH Verlag GmbH & Co. KGaA, Weinheim.

Table 7.2. 3 Quantum yield, peak emission wavelength and FWHM values depending on the OLA amount. Reprinted with permission from [117]. Copyright 2019 WILEY-VCH Verlag GmbH & Co. KGaA, Weinheim.

Amount of OLA	QY (%)	Wavelength (nm)	FWHM (nm)
without	69	610	31
500 µL	85	602	24
1000 µL	82	605	24

The uniform shell formation in the NPL synthesis is obtained by using 500 µL of OLA as shown in Figure 7.2.5. PL decays of all three samples are nearly identical with

~% 95 of the contribution coming from two exponential components having lifetimes of ~40-38 and ~12 ns (Table 7.2.4). However, due to the nonradiative decay processes such as charge trapping, the fast lifetime component of the sample synthesized without using OLA is stronger than the others. These experimental findings have shown the importance of the addition of OLA for the synthesis of highly efficient NPLs, which can be explained with the Covalent Bond Classification (CBC) method developed by Green [142], [143]. According the CBC method describing the interaction of the ligands with the surface of NCs, while cation rich surfaces can be effectively passivated by using X-type ligands such as carboxylates providing charge neutrality,[144] the cations on the neutral surfaces acting as a Lewis acid can be passivated with L-type ligands such as amines known as a Lewis base. Thus, the synthesis of core/shell NPLs using both OLA and OA would result in the proper passivation of surfaces, enabling higher QY as compared to the core/shell NPLs synthesized without OLA. The proper passivation of the surfaces is also further verified from the TRF measurements with the decreased contribution of the fastest lifetime component.

Table 7.2. 4 Time resolved fluorescence measurement fit data of the samples which are synthesized by using without, 500 µL and 1000 µL of OLA. Reprinted with permission from [117]. Copyright 2019 WILEY-VCH Verlag GmbH & Co. KGaA, Weinheim.

	τ_1 (ns)	Fractional intensity	τ_2 (ns)	Fractional intensity	τ_3 (ns)	Fractional intensity	τ_{avg} (ns)
w/o OLA	40.4	26.6%	12.4	66.7%	2.89	6.78%	11.9
500 µL OLA	39.4	27.8%	12.1	65.9%	2.63	6.33%	11.7
1000 µL OLA	37.6	33.4%	11.5	61.7%	1.50	4.84%	10.6

The best result in the CdSe/ZnS core/HI shell synthesis was obtained by using the combination of 500 µL of OLA and 500 µL of OA in accordance with their shape, QY and uniformity of the synthesized NPLs. This recipe is referred to as HI thin-shell recipe. The absorbance and PL spectra of the synthesized CdSe/ZnS core/HI thin-shell sample are given in Figure7.2.6a.

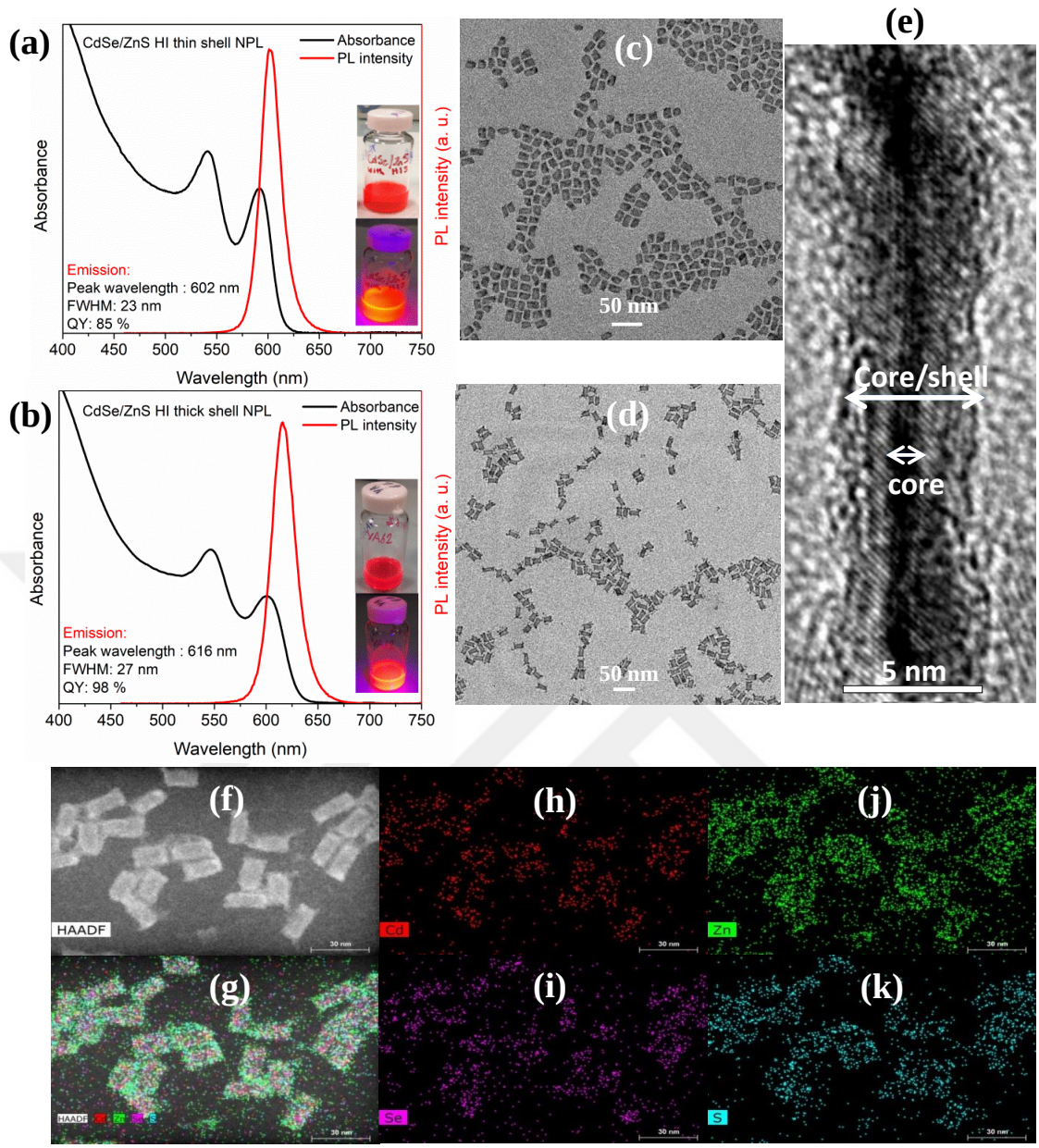

Figure 7.2. 6 Absorbance and PL spectra of the synthesized CdSe/ZnS core/hot-injection (HI) a) thin-shell and (b) thick-shell NPL samples, accompanied with their respective sample photographs presented in (a) and (b) under daylight and UV light. HI thin-shell growth reproducibly allows for narrow emission while HI thick-shell growth consistently enables high QY. TEM images of CdSe/ZnS core/HI (c) thin-shell and (d, e) the thick-shell NPL samples, (f) HAADF-TEM images of the CdSe/ZnS HI thick-shell NPL sample and (g) corresponding to EDS mapping with Cd, Se, Zn and S elements while (h-k) show single element analysis of CdSe/ZnS HI shell NPL sample. Reprinted with permission from [117]. Copyright 2019 WILEY-VCH Verlag GmbH & Co. KGaA, Weinheim.

The FWHM, peak emission wavelength and QY of this sample are 23 nm, 602 nm and 85%, respectively. From TEM images in Figure 7.2.6c, the vertical thickness of the CdSe/ZnS core/HI thin-shell sample is measured as 3.04 ± 0.3 nm. Using thick-shell (or additional shell coating) is well known to improve the stability, as reported in many earlier works, due to the effective protection from the surrounding environment [132]–

[137]. Here CdSe/ZnS core/HI thick-shell sample was synthesized with some modifications and using extra shell precursor in the HI thin-shell recipe presented in Methods section. The absorbance, PL and high-resolution TEM image of the as-synthesized CdSe/ZnS core/HI thick-shell sample are presented in Figures 7.2.6b and 7.2.6d. The QY, FWHM and peak emission wavelength of the sample are 98%, 27 nm and 616 nm, respectively. The core/shell structure is clearly seen from the cross-sectional TEM image of the HI thick-shell sample in Figure 7.2.6e thanks to the contrast difference between the CdSe core and the ZnS shell. The thickness of the HI thick shell NPLs increased to 4.03 ± 0.43 nm. A narrow emission bandwidth as low as 21 nm can be obtained using the thin-shell structure, while a near-unity QY is reproducibly using the HI thick-shell. The reproducibility of the synthesis results including the QY and FWHM values in the synthesis of HI thin- and thick-shell NPLs is shown in Table 7.2.5, which contains 10 different successive experiments to demonstrate the reproducible syntheses.

Table 7.2. 5 . Quantum yield, FWHM values of successive synthesis of 10 hot injection thin and thick shell samples which are synthesized with the same HI thin and same HI thick shell recipe, separately. Reprinted with permission from [117]. Copyright 2019 WILEY-VCH Verlag GmbH & Co. KGaA, Weinheim.

	HI thin shell		**HI thick shell**	
Number of synthesis	QY (%)	FWHM (nm)	QY (%)	FWHM (nm)
# 1	88	22	92	24
# 2	87	23	95	25
# 3	82	26	98	23
# 4	86	24	98	27
# 5	92	26	91	28
# 6	83	24	93	25
# 7	81	25	98	24
# 8	81	27	90	25
# 9	80	24	95	23
# 10	85	23	98	26

Furthermore, the uniform coating of ZnS shell layers on CdSe core NPL were verified with EDS mapping for HI thick-shell sample in Figures 7.2.6f-k. For further structural characterizations of the HI thin- and thick-shell NPLs, we synthesized both thin and thick samples by using the same 4mLCdSe core NPLs. Detailed lateral and cross-sectional TEM images of HI thin- and thick-shells grown on the same 4ML core NPLs are presented in Figure 7.2.7, along with EDS analyses in Table 7.2.6. The atomic ratio of Cd and Se in the CdSe/ZnS HI thin-shell NPL is 11.2% and 19.1%, while the ratios of Cd and Se in the HI thick-shell NPLs are 4.1% and 6.9%. Due to the additional shell coating in the HI thick-shell NPLs, the atomic ratio of the ZnS shell material was found as 47.8% for Zn and 41.1% for S, while that in the HI thin-shell sample was measured as 35.6% for Zn and 34.0% for S.

Table 7.2. 6 Energy dispersive X-ray analysis of hot injection thin and thick shell samples of CdSe/ZnS core/shell NPLs. Reprinted with permission from [117]. Copyright 2019 WILEY-VCH Verlag GmbH & Co. KGaA, Weinheim.

	Thin Shell		Thick Shell	
Element	Weight %	Atomic %	Weight %	Atomic %
Cd(K)	20.34	11.20	8.52	4.13
Se(K)	24.41	19.14	9.95	6.87
Zn(K)	37.62	35.63	57.32	47.82
S(K)	17.61	34.01	24.18	41.15

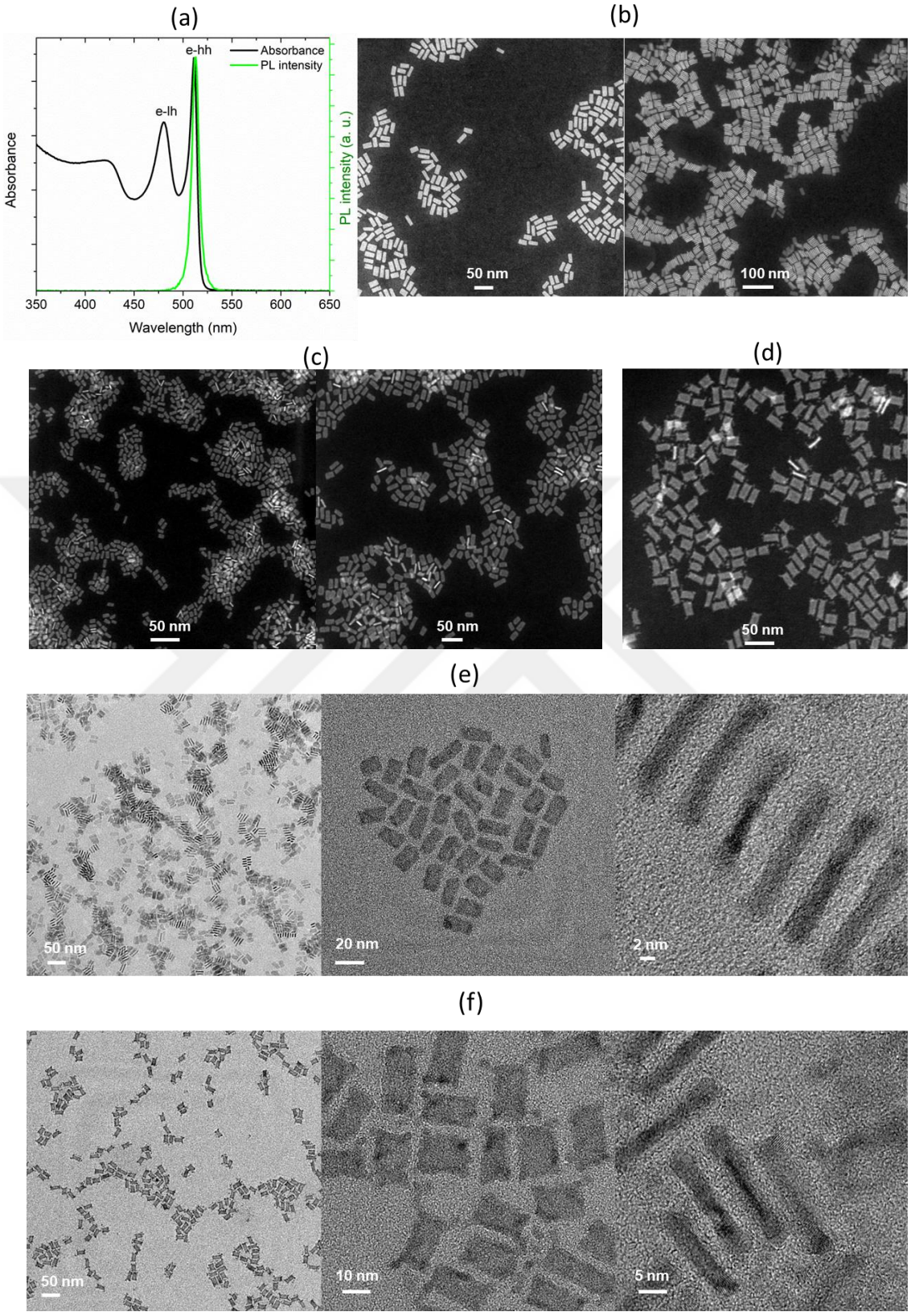

Figure 7.2. 7. (a) Abs and PL spectra of 4ML CdSe core-only NPL, HAADF-TEM images of (b) CdSe core-only, (c) CdSe/ZnS core/HI thin shell, (d) CdSe/ZnS core/HI thick shell NPLs . HR-TEM images of (e) hot injection thin shell, (f) hot injection thick shell samples, both are synthesized with same 4mLCdSe core NPLs that are given (a) and (b). Reprinted with permission from [117]. Copyright 2019 WILEY-VCH Verlag GmbH & Co. KGaA, Weinheim.

To investigate the in-solution stability of the HI thin- and thick-shell samples, we performed thermal stability, UV-exposure and repetitive purification tests. The thermal stability test was conducted monitoring the PL intensity of the sample, which was cleaned and dispersed in 10mLof ODE, as a function of the temperature from 300 to 525 K with 25 K increments. L intensity of the HI thin- and thick-shell samples decreases and their FWHM increases with the increasing temperature as shown in Figure 7.2.8a.

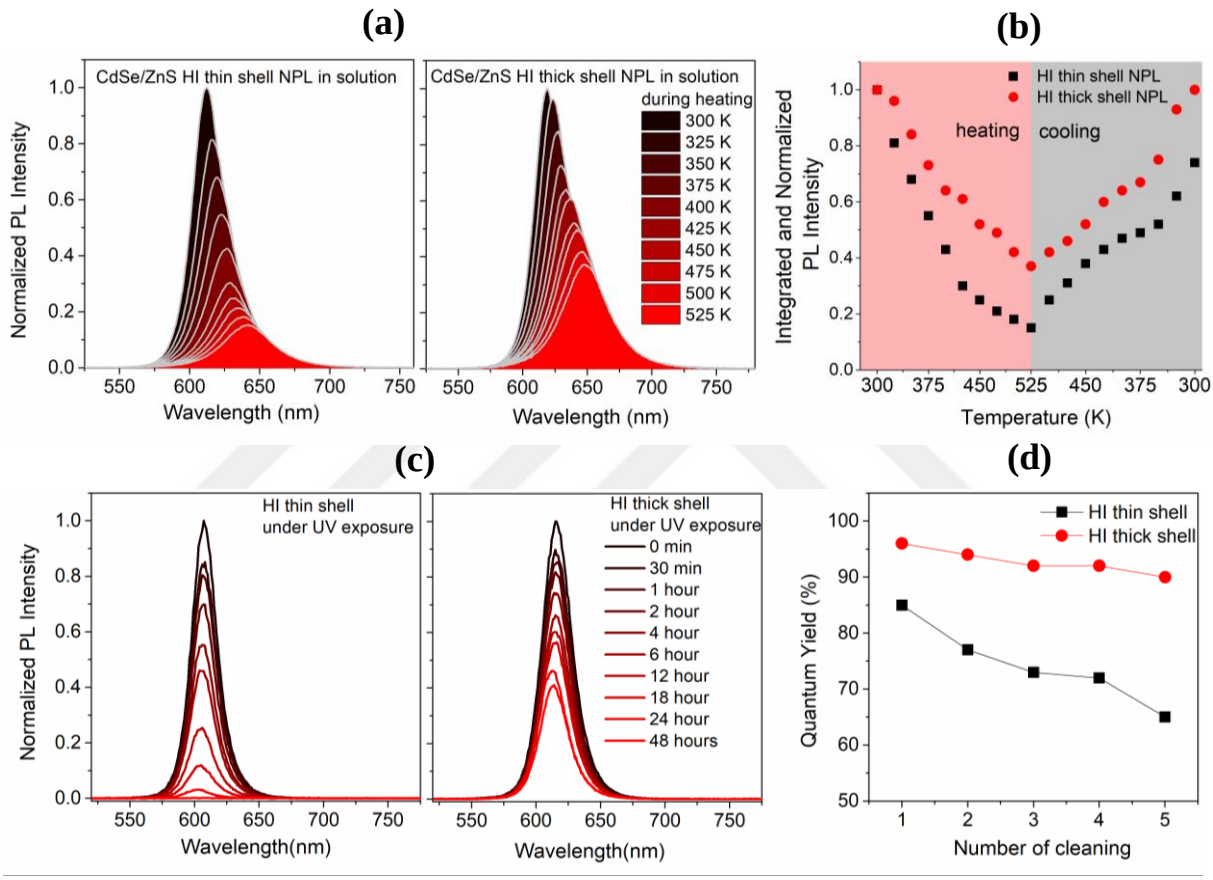

Figure 7.2. 8 Normalized PL intensity of (a) CdSe/ZnS HI thin- and HI thick-shell NPL in solution (cleaned and precipitated with ethanol, then dissolved in 10mLof octadecene) during heating from 300 K to 525 K under argon flow with respect to emission wavelength. (b) Integrated PL intensity of CdSe/ZnS HI thin- and thick-shell NPL samples during temperature elevation. HI thin-shell NPL sample in solution restored 100 % of its initial integrated and normalized PL intensity, while HI thin-shell NPL sample recovered 70 %. (c) UV-stability test of CdSe/ZnS HI thin- and thick-shell NPL samples which are synthesized with HIS method, (d) purification test of the CdSe/ZnS HI thin- and thick-shells. Reprinted with permission from [117]. Copyright 2019 WILEY-VCH Verlag GmbH & Co. KGaA, Weinheim.

Furthermore, the PL emission spectra of the samples red-shift by about 30 nm in the case of thin-shell sample and by 29 nm in the case of thick-shell at the elevated temperatures. At 400 K, our HI thin- and thick-shell samples unprecedentedly sustain

42% and 65% of their initial PL intensities, respectively, which indicates that these HI shell NPLs are very promising candidates for laser and LED applications since the operating temperature can be as high as 400 K. With further increasing the temperature to 525 K, the HI thin-shell sample preserves 15% of its initial PL intensity, whereas the HI thick-shell sample maintains 37% of its initial PL intensity at the same temperature. The PL emission of the HI thick-shell sample has almost fully recovered its initial emission at 300 K, whereas the thin-shell sample preserved 74% of its spectrally integrated emission during the thermal cycling up to 525 K as shown in Figure 7.2.8b. As far as the thermal stability is concerned, this is the best stability level for this type of colloidal materials within the scope of all high-temperature PL measurements and thermal cycling experiments reported in the literature, to the best of our knowledge. Secondly, the photostability of the HI thin- and thick-shell samples was examined by UV-test, which is shown in Figure 7.2.8c, by exposure to continuous UV light for 48 hours with a UV-lamp having a peak emission wavelength of 354 nm. After 48-hour continuous UV-exposure, the HI thick-shell sample maintained 40% of its emission. Finally, the purification test was carried out for the stability of the synthesized HI thin- and thick-shell samples and the QY of the HI thick-shell sample was measured to be more than 91% even after 5 times cleaning with ethanol, while the QY of the HI thin-shell dropped to 62%. It is hard to preserve the stability of the NCs in organic phase typically after more than three times cleaning due to the separation of the excess ligand.

Colloidal NCs have been widely investigated for use in solid thin films in numerous colloidal optoelectronic devices such as LEDs,[96], [129], [145] photodetectors,[146] solar cells[147] and lasers [127], [128], [148]. For these applications, thermally stable NCs are highly desirable for long-term use and commercial deployment. Therefore, we systematically studied the thermal stability of our HI thin- and thick-shell samples at high temperature in comparison to c-ALD shell grown and no-shell NPL samples. Thermal test study was carried out using five different NPL samples, namely CdSe only-core, CdSe/ZnS core/c-ALD thin-shell, CdSe/ZnS core/c-ALD thick-shell, CdSe/ZnS core/HI thin-shell and CdSe/ZnS core/HI thick-shell NPLs. Here 2mLshell coated NPLs using c-ALD technique is referred to as thin-shell, while 5mLcoated sample is, as the c-ALD thick-shell the PL emission peaks of these c-ALD samples match those of the HI thin- and thick-shell samples,

respectively, as shown in Figure 7.2.9. The structural and optical characterizations of these samples are given in Figures 7.2.9-10 and Tables 7.2.7-8.

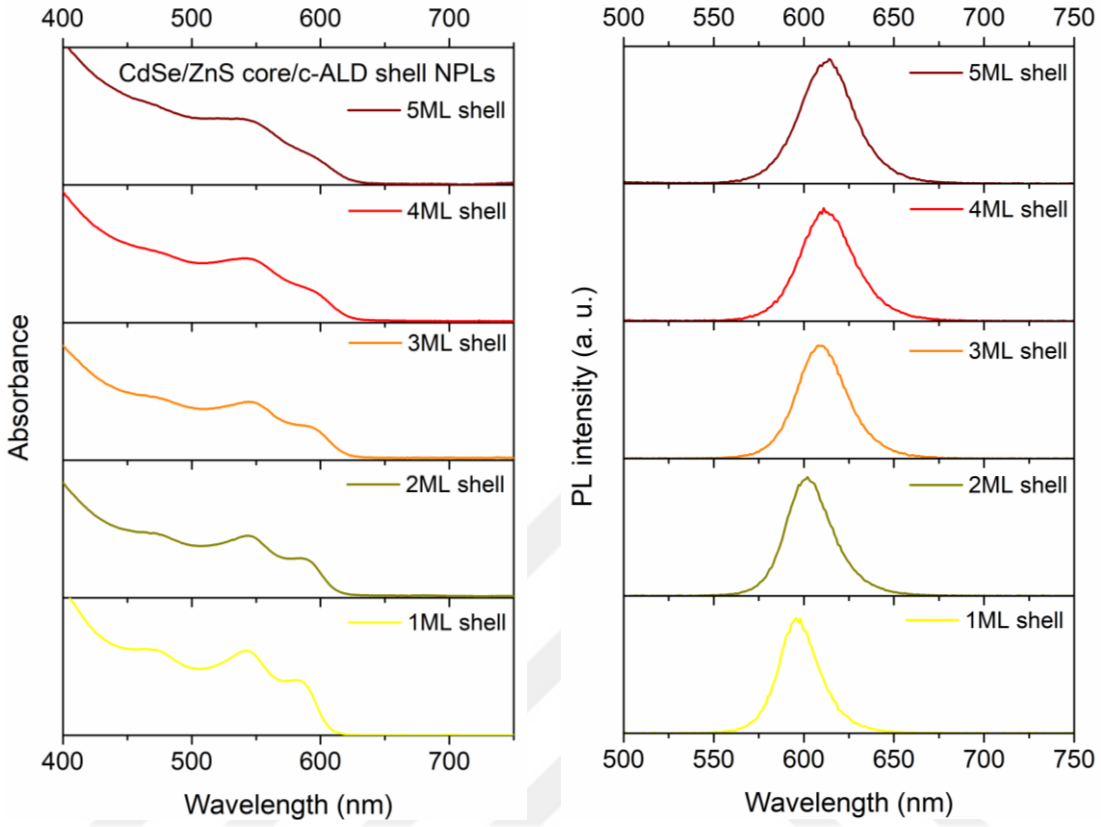

Figure 7.2. 9 (a) Absorbance and (b) PL graphs of CdSe/ZnS Core/shell heteronanoplatelets based on the number of coated ZnS shell layers with c-ALD technique. Reprinted with permission from [117]. Copyright 2019 WILEY-VCH Verlag GmbH & Co. KGaA, Weinheim.

Table 7.2. 7 Wavelength and FWHM of the CdSe/ZnS core/shell NPLs which are synthesized with c-ALD technique. Reprinted with permission from [117]. Copyright 2019 WILEY-VCH Verlag GmbH & Co. KGaA, Weinheim.

c-ALD ZnS shell	Wavelength (nm)	FWHM (nm)
1ML	595	25
2ML	602	29
3ML	609	32
4ML	612	33
5ML	614	35

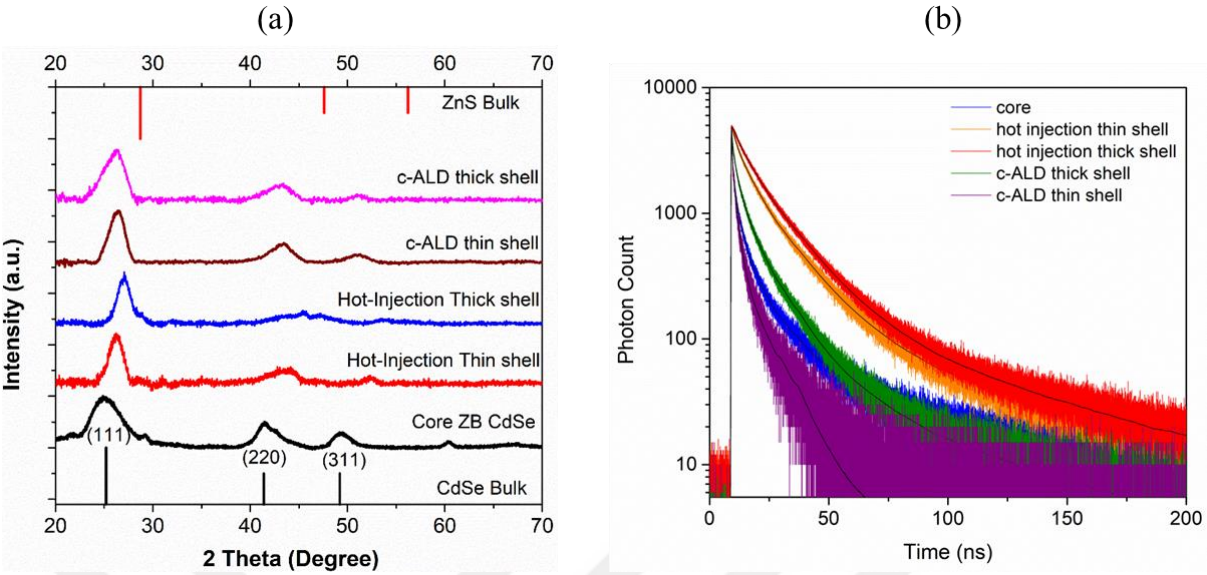

Figure 7.2. 10 (a) XRD patterns of the CdSe core with zinc blende crystal structure and the corresponding core/shell nanoplatelets with different ZnS shell layers. The XRD peaks of zinc blende bulk CdSe (black vertical lines at the bottom) and ZnS (red vertical lines at the top) are included as references. Here the XRD peaks of the 2Θ degree were fitted for the CdSe bulk material and, with the addition of ZnS shell material, the peaks shifted to characteristic XRD peaks of the ZnS bulk material. It is inferred that the largest shift in this figure is observed in the CdSe/ZnS HI thick-shell NPL sample due to the higher concentration of shell materials. (b) TCSPS analysis of core, core/thin and thick shells with c-ALD technique, core/ hot injection thin and thick shells samples. PL decays of the core and core/shell NPLs are plotted. The decays of core/HI shell samples are much slower than core and core/c-ALD shell NPLs, in accordance with their higher QY. The decays are fitted with multiple exponentials convolved with the instrument response function as listed. About %95 of the emission of core/HI shell NPLs from two dominant exponential components with the lifetimes of 38-40 and 12 ns, which are attributed to the radiative processes. The core and core/c-ALD shell NPLs have an additional fast lifetime component of about 0.25 ns, which is possibly due to the nonradiative decay processes such as charge trapping. This is in accordance with the much higher QYs of the core/HI shell samples compared to the core-only and core/c-ALD shell NPLs. The absence of such a fast component in the HI shell samples verify that the shells grown via HI technique achieves effective surface passivation and eliminates most of the surface trapping sites. Reprinted with permission from [117]. Copyright 2019 WILEY-VCH Verlag GmbH & Co. KGaA, Weinheim.

Table 7.2. 8 Lifetime component of the only-core, core/thin and thick shells with c-ALD technique, core/ hot injection thin and thick shells samples. Reprinted with permission from [117]. Copyright 2019 WILEY-VCH Verlag GmbH & Co. KGaA, Weinheim.

	τ_1 (ns)	Fractional intensity	τ_2 (ns)	Fractional intensity	τ_3 (ns)	Fractional intensity	τ_4 (ns)	Fractional intensity	τ_{avg} (ns)
Only-core	45.2	30.3%	8.43	40.7%	1.91	20.0%	0.23	9.06%	1.81

HI thin shell	37.8	30.1%	11.4	63.3%	1.89	6.60%	-	-	10.1
HI thick shell	40.4	27.6%	12.9	67.5%	2.77	4.90%	-	-	13.0
c-ALD thin	10.6	43.8%	1.99	42.4%	0.25	13.8%			1.24
c-ALD thick	33.9	20.8%	9.39	56.1%	2.23	18.6%	0.31	4.46%	3.38

For the thermal stability test, we have used home-made setup, which is presented in Figure 7.2.11. The temperature of the film was measured with FLIR type thermal camera, which features 0.1°C temperature precision. The PL spectrum was simultaneously taken by using MAYA 2000 model spectrophotometer. All measurements were performed in ambient conditions and the films were prepared without any protective medium and/or sealant.

Figure 7.2. 11 Thermal test measurement setup photographs for film form of the samples. Reprinted with permission from [117]. Copyright 2019 WILEY-VCH Verlag GmbH & Co. KGaA, Weinheim.

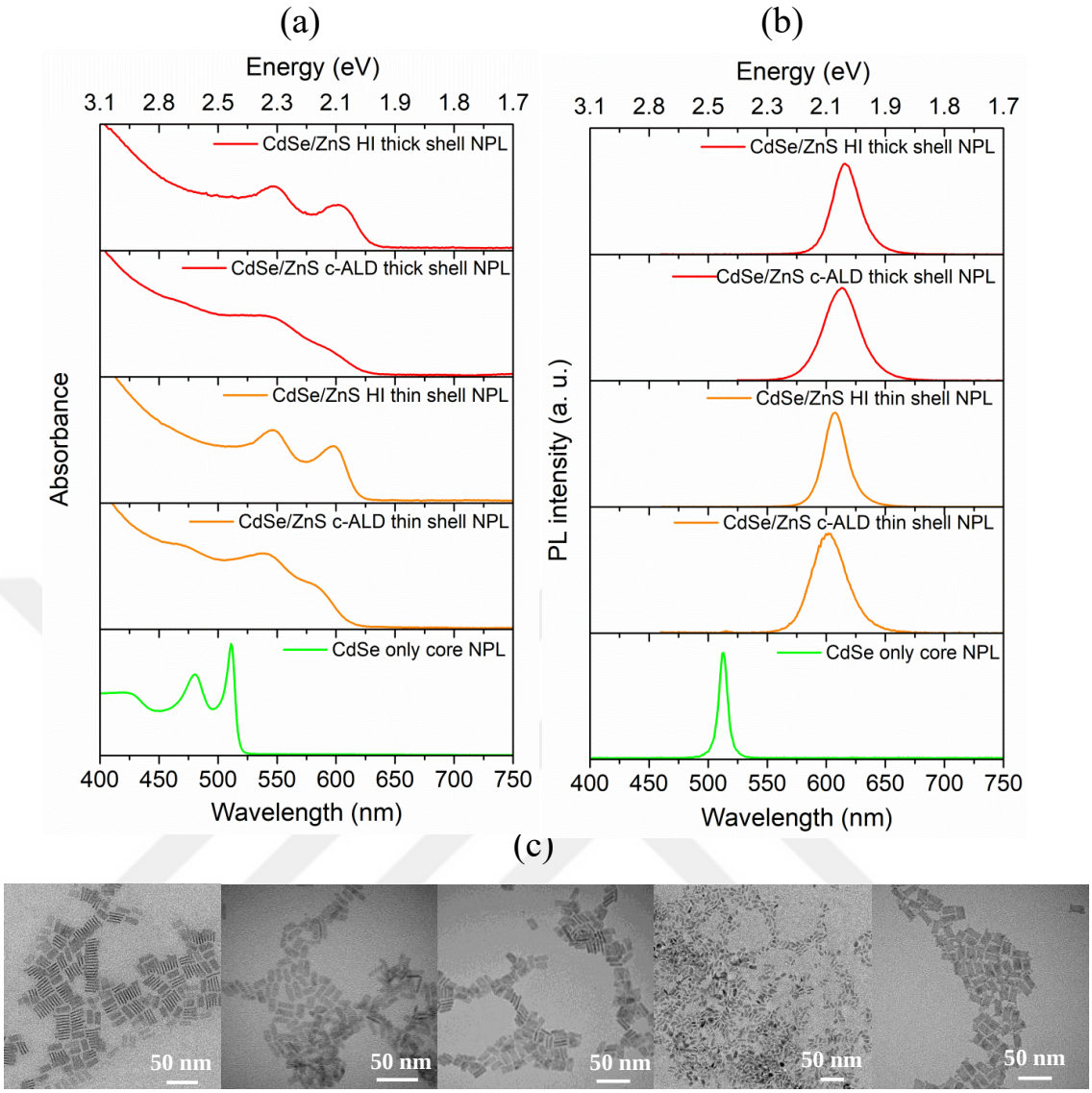

Figure 7.2. 12 (a) Absorbance and (a) photoluminescence spectra and (c) TEM images of the CdSe only core NPL, c-ALD thin shell, HI thin shell, c-ALD thick shell and HI thick shell CdSe/ZnS NPL samples. FWHM of core/shell NPLs with hot injection method are narrower than samples synthesized by c-ALD method. Reprinted with permission from [117]. Copyright 2019 WILEY-VCH Verlag GmbH & Co. KGaA, Weinheim.

The temperature of the samples was increased from 300 to 525 K, while the PL spectrum of the samples was collected with spectrophotometer every 25 K temperature change. With the increasing temperature, we observed red-shifted and decreased PL intensity from the prepared solid films with increased FWHM as shown in Figures 7.2.13a and 7.2.13b. Initial PL intensity of the only-core, c-ALD thin- and thick-shell samples dramatically decreased during heating from 300 to 400 K. At 400 K, the PL intensity of the only-core, c-ALD thin- and thick-shell samples decreased to 4%, 2% and 10% of their initial intensities, respectively, while the HI thin- and thick-shell

samples preserved 40% and 52% of their initial PL intensities. PL spectra of the only-core, c-ALD thin- and thick-shell samples were not detectable easily at and above 450 K. However, HI thin- and thick-shell samples preserved 20% and 35% of their initial intensity values at 450 K and 6% and 20% at 500 K, respectively. Due to the correlation between the integrated PL spectra and QY, we also integrated and normalized PL spectra of the samples in Figure 7.2.13b. The deceleration rate in the PL spectra of the HI thin- and thick-shell samples linearly change with the increased temperature. Also, the thermal stability and PL recovery with thermal cycling for NPLs were demonstrated in ambient condition in Figure 7.2.13c.

CdSe core-only NPLs exhibit the lowest thermal stability as compared to the CdSe/ZnS core/shell NPLs regardless of the ZnS shell thickness and growth approach. The similar behavior has been also reported extensively in many studies that the core/shell NCs exhibit better thermal stability than their core-only counterparts [149]–[151]. According to the study reported by Diroll et al., another important factor affecting the thermal stability of the core/shell NCs is the growth temperature of the shell [152]. When the growth temperature of the shell was performed at higher temperatures (as high as 300 ˚C and above), these core/shell NCs exhibit higher thermal stability than similar core/shell NCs that were synthesized with highly reactive precursors at lower temperatures below 200 ˚C. This finding also verifies the significantly improved thermal stability of the CdSe/ZnS core/shell NPLs synthesized with hot-injection shell growth approach.

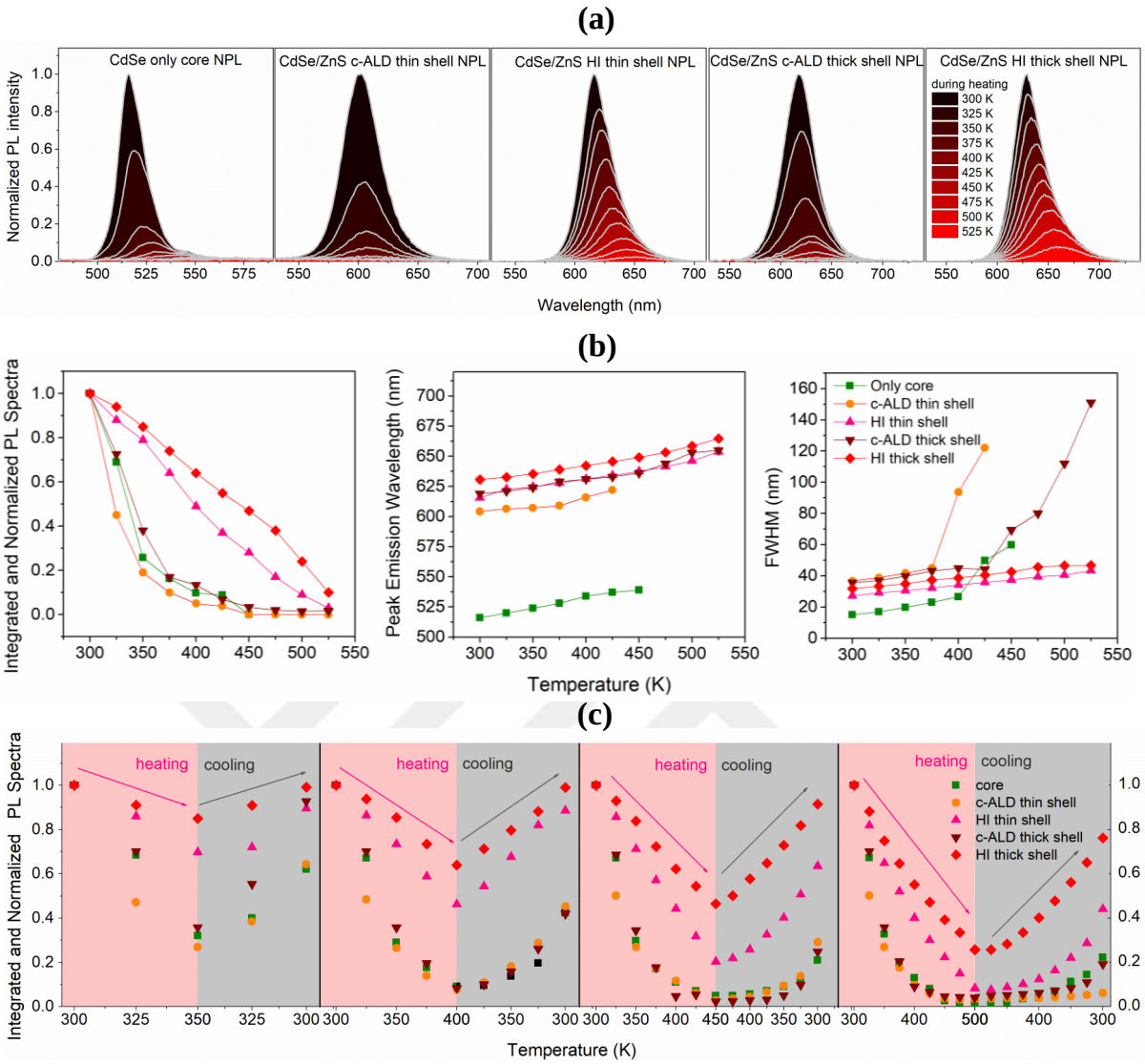

Figure 7.2. 13 (a) Normalized PL intensity (b) Variation of the normalized and integrated PL spectra, peak emission wavelength and FWHM of the CdSe only core NPL, CdSe/ZnS c-ALD thin-shell NPL, CdSe/ZnS HI thin-shell NPL, CdSe/ZnS c-ALD thick-shell NPL and CdSe/ZnS HI thick-shell NPL film samples during heating from 300 to 525 K under ambient condition. (c) Variation of the integrated and normalized PL spectra of all samples during heating and cooling cycles from 300 to 350 K; from 300 to 400 K; from 300 to 450 K; from 300 to 500 K. CdSe/ZnS HI thick-shell NPLs outperformed all other NPLs by realizing unprecedented level of thermal stability and their initial PL intensity is fully recovered up to 450 K in air condition. Reprinted with permission from [117]. Copyright 2019 WILEY-VCH Verlag GmbH & Co. KGaA, Weinheim.

Also, the reversibility of PL emission was investigated by using thermal cycling at the elevated temperatures of 350, 400, 450 and 500 K such that the samples were first heated from 300 K to a specific elevated temperature and then cooled back to 300 K for the only-core, core/c-ALD thin-shell, core/c-ALD thick-shell, core/HI thin-shell and core/HI thick-shell NPLs. The results are shown in Figure 7.2.13c. The loss in the PL emission of only-core, core/c-ALD thin-shell, and core/c-ALD thick-shell at 350 K is

more than 70% and the loss at 400 K is 90%. At 350 K, the losses in the PL emission of HI thin- and thick-shell samples are only 30% and 15%, and the loss at 400 K is 55% and 35%. However, after thermal cycling, the PL emission of HI thick-shell NPLs at 350 K and 400 K fully recovered its initial PL intensity when cooled to 300 K, while at the same temperature HI thin-shell NPL recovered 90% and 88% of the initial PL intensity. The recovery of the loss in the integrated PL emission of the only-core, core/c-ALD thin-shell and core/c-ALD thick-shell samples is approximately 40% at 400 K. At 450 K and 500 K cycling, the PL emission reversibility of HI thick-shell NPLs is 92% and 77%, respectively. The HI thick-shell sample in cycling experiment exhibited the best performance in terms of PL reversibility, showing the effective passivation of NPLs with the growth highly crystalline ZnS shell at higher reaction temperatures.

Previous report by Diroll et al.[152] indicates that reversibility and stability of the PL emission correlates with electron and hole trap states, which are formed during the thermal cycling. Furthermore, in that study, reversibility of the loss in PL emission during the thermal cycling was investigated with different size and shape of CdSe core and CdSe/CdS core/shell NCs and it was found that thermal stability of rod-like core-only and core/thin-shell structured samples is the best among all studied samples. In our study, owing to the effective protection of the core surface with thick ZnS shell, trap states are passivated and hence HI thick-shell NPLs not only exhibit the best performance among the reported NPL samples, but also outperforms previously reported colloidal 0D quantum dots in terms of the thermal stability [149]–[151]. Optical properties and stability test results of the HI shell samples show that HI shell NPL synthesis method is superior to c-ALD shell synthesis in terms of making highly stable and efficient NPLs (Figure 7.2.14).

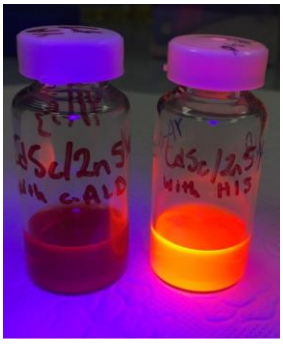

Figure 7.2. 14 The photograph of c-ALD shell sample and HI shell sample under UV illumination. Reprinted with permission from [117]. Copyright 2019 WILEY-VCH Verlag GmbH & Co. KGaA, Weinheim.

All these advantages of core/HI shell synthesis imply that the resulting CdSe/ZnS heteronanoplatelets with substantially enhanced QY and improved thermal stability enables the utilization of those NPLs in high power density applications, e.g., lasing. For this purpose, tremendous research efforts were aimed at synthesizing particles with optimized structure and composition to obtain the lowest gain threshold values with high gain coefficients [153]–[155]. Among various loss mechanisms, being the most effective, Auger recombination prohibits high performance optical gain in QDs. Three-dimensional confinement of QDs increases the uncertainty in momentum which boosts Auger recombination strictly obeying universal volume scaling law [156]. Owing to one-dimensional confinement in NPLs, momentum conservation is more pronounced and Auger recombination rate is significantly diminished [148], [154], [157]. In addition to suppressed Auger recombination, large absorption cross-section and giant oscillator strength of NPLs resulted in exceptional low amplified spontaneous emission (ASE) threshold values reaching 6 μJ cm^{-2} [127]. Deposition of CdS shell layer over CdSe core allows electron wave function to spread over the whole structure further reducing Auger recombination probability. Additionally, CdS shell layer contributes an increase in the absorption cross-section and the photoluminescence quantum yield which are effective in this observed record low ASE threshold. Surrounding the periphery of the NPL with a crown layer also have been shown effective in the reduction of ASE threshold for lasing applications [128], [158], [159]. Nonetheless, high temperature stability of the NPLs for optical gain applications still remains as a limitation that needs to be addressed.

To address this problem, near-unity QY and high-temperature stability of CdSe/ZnS core/HI shell NPLs make them perfect candidates for lasing applications. We studied optical gain performance of the HI shell NPL samples using 5 different film samples: the only-core NPLs, HI thin-shell NPLs, HI thick-shell NPLs and two set of annealed HI thin-shell NPLs, one at 400 K and the other at 500 K. The samples were cleaned three times and concentrated solutions were dispersed in toluene. The films were prepared via spin-casting in glovebox and sealed between two fused silica wafers with epoxy-resin. The annealed samples were sealed after annealing. Highly uniform films of the NPLs were obtained, as shown under ambient lighting and UV-excitation in Figure 7.2.15. 400 K annealed films under UV-illumination are pictured in Figure 7.2.16.

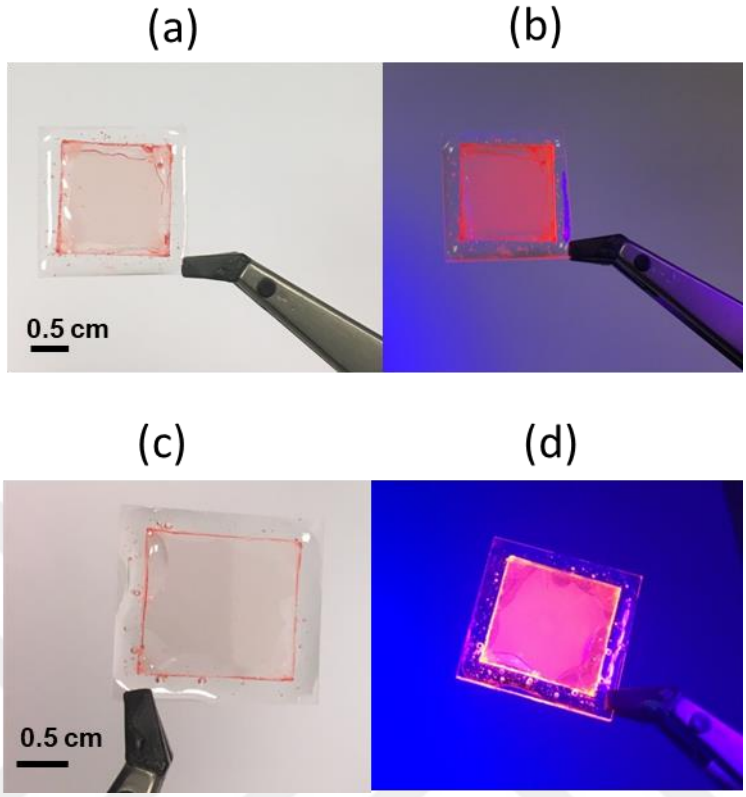

Figure 7.2. 15 The photograph of spin-coated and sealed HI shell NPL film samples (a) and (c) without UV illumination, (b) and (d) under UV illumination. Reprinted with permission from [117]. Copyright 2019 WILEY-VCH Verlag GmbH & Co. KGaA, Weinheim.

Figure 7.2. 16 HI shell NPL sample is spin-coated on quartz glass and annealed at 120 ˚C for 10 min in glovebox. These photos are taken at the end of this time with UV laser illumination. Reprinted with permission from [117]. Copyright 2019 WILEY-VCH Verlag GmbH & Co. KGaA, Weinheim.

Figure 7.2.17a-b and their insets present ASE of the spin-coated HI thin-shell and HI thick-shell NPLs under one photon absorption (1PA) excitation. 1PA pumping ASE characterization of the HI NPL films annealed at 400 and 500 K is also given in Figures

7.2.17c, d. Narrow ASE peaks are clearly observed in the PL spectra, which are redshifted compared to their spontaneous emission peak. This red-shift is 12 nm for the core-only NPL film, 15 nm for the HI thin-shell NPL film, 8 nm for HI thick-shell NPL film, 9 nm for 400 K-annealed NPL film and 11 nm for 500 K-annealed NPL film. This red-shift observed in ASE peaks is characteristic to Type-I structure of the core/HI shell NPLs indicating the attractive biexciton interactions.

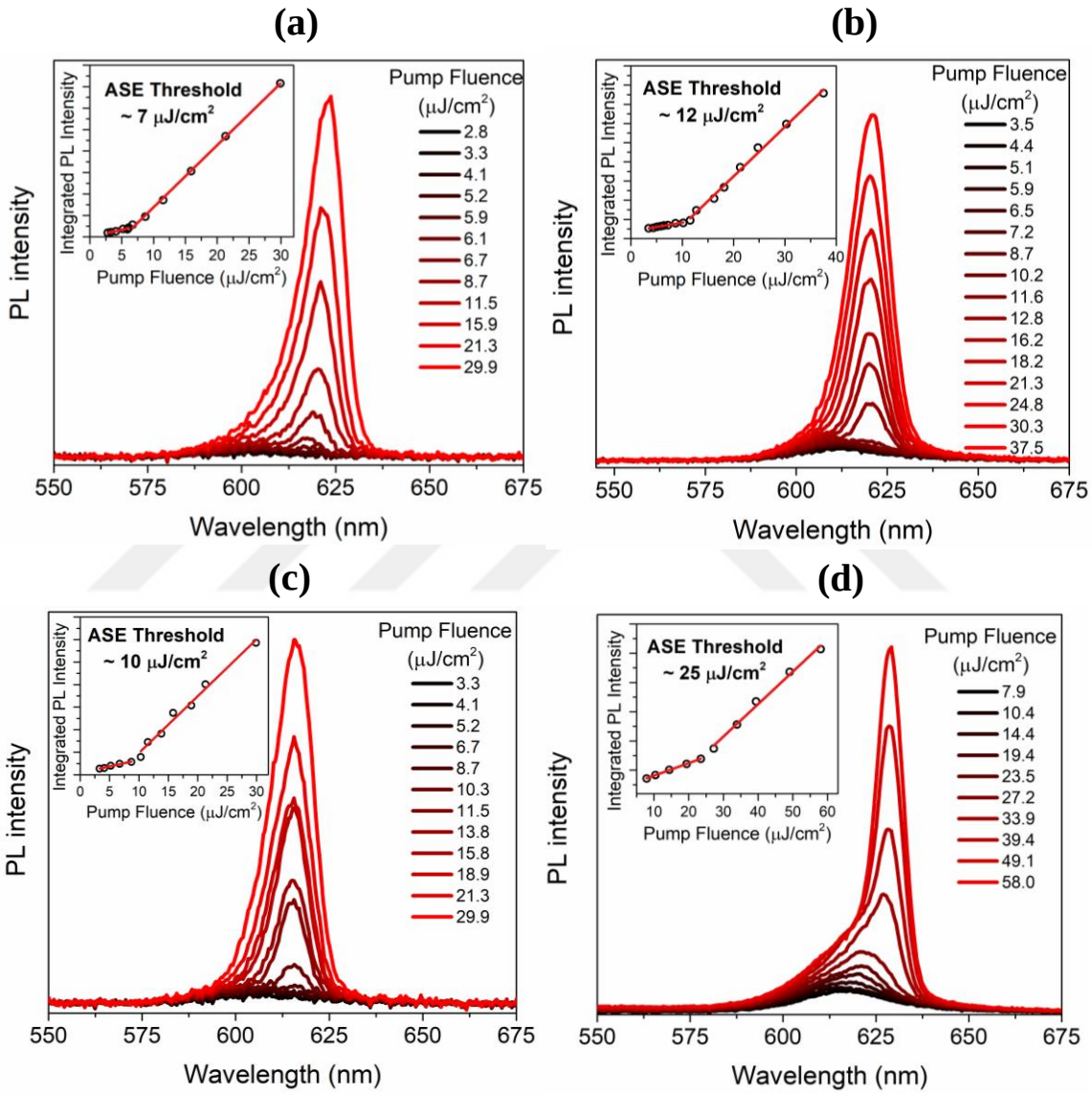

Figure 7.2. 17 Amplified spontaneous emission spectra of (a) CdSe/ZnS HI thin-shell NPL and (b) HI thick-shell NPL films. CdSe/ZnS HI thin-shell NPL film (c) annealed at 400 K and (d) annealed at 500 K under stripe excitation pumping. Annealed films at high temperature also display very low gain threshold values (slightly above pristine films) which proves that the annealed film samples possess significant thermal stability. The insets show the integrated emission intensity as a function of the pumping energy density. Reprinted with permission from [117]. Copyright 2019 WILEY-VCH Verlag GmbH & Co. KGaA, Weinheim.

Under 1PA pumping, the HI thin- and HI thick-shell NPLs films have ultra-low optical gain threshold values as low as 7 μJ cm^{-2} and 12 μJ cm^{-2}, respectively. This observed ASE threshold value for the thin-shell HI NPLs is very close to previously reported record low threshold values for II-VI nanocrystals. This reduced ASE threshold values compared to the core NPLs giving 18 μJ cm^{-2} can be explained with the enhanced absorption cross-section of HI NPLs and effective passivation of surface trap sites. Unlike CdS shell resulting in quasi-Type-II band structure, ZnS shell provides a band offset for the conduction band preventing interaction of electrons with surface defects. Because of the reduction in trap state interactions, HI shell NPLs shows near-unity efficiency in spontaneous emission, which also improves their optical gain performance. Owing to the high thermal stability of the HI shell NPLs, their annealed films also exhibit outstanding gain performance and their threshold values are obtained as low as 10 μJ cm^{-2} after annealing at 400 K, and 25 μJ cm^{-2} after annealing at 500 K.

7.3 Summary

We have successfully synthesized the high-quality CdSe/ZnS core/HI shell NPLs by using hot injection shell growth. With this new synthesis approach, CdSe/ZnS core/HI shell NPLs having near-unity QY have been synthesized in a reproducible way. These new HI CdSe/ZnS core/shell NPLs exhibit also excellent photo and thermal stability, surpassing the performance of their counterparts synthesized with the conventional c-ALD method. These enhanced optical properties of HI shell NPLs also enable outstanding optical gain performance with thresholds as low as 7 μJ cm^{-2}. These findings indicate that these new core/HI shell NPLs will be important step for the development of robust continuous-wave lasers from the chemically synthesized colloidal nanocrystals and various optoelectronic applications requiring high thermal stability.

7.4 Methods

7.4.1 4ML CdSe only-core and CdSe/ZnS core/c-ALD shell NPL synthesis.

4mLCdSe core synthesis

4mLCdSe core NPLs are synthesized according to the protocol presented in the literature with slight modifications [160]. As a first step, Cd myristate was prepared by mixing sodium myristate and cadmium nitrate tetrahydrate initially dissolved in methanol. Then, when the solution becomes bulky, it was filtered and washed with methanol and left under vacuum overnight [160]. For a typical synthesis of 4mLCdSe core NPLs, 340 mg of Cd myristate, 24 mg of Se, and 30mLof ODE were loaded in a 100mLthree-neck flask. After stirring the solution at ~ 100 ˚C under vacuum for an hour, the reaction mixture was heated to 237 ˚C under argon atmosphere. When the color of solution became dark orange at ~195 ˚C, 80 mg of cadmium acetate dihydrate was swiftly added to the reaction mixture. After 10 min growth at 240 ˚C, the reaction was cooled down to room temperature with the addition of 1mLof OA. The resulting CdSe core NPLs were cleaned with the addition of ethanol and centrifuged at 6000 rpm for 6 min. The precipitated CdSe core NPLs were dissolved in hexane and further purified by using ethanol to obtain pure population of 4mLCdSe core NPLs.

CdSe/ZnS core/c-ALD shell NPLs synthesis

CdSe/ZnS core/c-ALD shell NPLs were synthesized according to the methods of Ithurria et al. with slight modifications [132]. For a typical synthesis, 1mLof CdSe core NPLs (100 µL of stock solution diluted in 3mLof hexane has an optical density (OD) of 1 at 350 nm, assuming a 1-cm optical path length) was purified several times with ethanol. The precipitated NPLs were dissolved in 3mLhexane and mixed with 3mLNMF in 50mLcentrifuge tube, forming a two-phase mixture. With the addition of excess amount of ammonium sulfide solution (75 µL), the color of the solution was changed and the NPLs were transferred from nonpolar hexane to polar NMF phase. The solution was shaken for 5-10 min to completely cover the surface of NPLs with sulfur. The upper hexane phase was removed and the NPLs were precipitated with the addition of 0.5mLof acetonitrile and excess toluene until the flocculation was observed. Then, the solution was centrifuged at 10000 rpm for 3 minutes. The purification step was performed at least two times for the complete removal of excess S precursor to inhibit the formation of ZnS nanoparticles as a side product. The precipitated NPLs were dissolved in 2mLof NMF and combined with 2mLof 0.2 M Zn acetate dihydrate solution in NMF. After shaking for 5 - 10 min, the solution was washed two times according to the same method as described above. Thus, one layer of ZnS was coated on

the surface. After the desired number of layers of ZnS shell was coated, 0.5mLof the OLA capping agent and 5mLof hexane were added. The sample was heated a little bit, sonicated and placed in the dark for at least 2 hours. Then, the solution cleaned with ethanol and dispersed in hexane.

7.4.2 CdSe/ZnS HI thin-shell NPLs synthesis.

5mLof ODE, 0.2 mmol of Zn acetate, a certain amount of the 4ML core NPL and 500 µL OA are introduced to a 50mLthree-necked flask. The solution is stirred under vacuum at room temperature for an hour to evaporate hexane. Then, the mixture is heated up to 85-90 ˚C and kept for 30 min to completely remove water and/or any other remaining volatile solvents. After degassing step, OLA is added at 90 ˚C and the solution is heated to 300 ˚C under argon atmosphere. Meanwhile, 70 µL of octanethiol in 4mLof ODE solution is prepared and it is started to inject around 170 ˚C by using syringe pump. Initially, the rate of the syringe pump is adjusted to 10 mL/h, and then at 250 ˚C, it is switched to 4 mL/h. After the temperature is reached to 300 ˚C, it is kept at this temperature for an hour to growth of ZnS shell. After that, the flask is cooled immediately by cold water and 5mLof hexane is inserted. No precipitate is attained after the first centrifugation. Later, by ethanol cleaning, the whole NPLs are precipitated and finally dispersed in hexane.

7.4.3 CdSe/ZnS HI thick-shell NPLs synthesis.

The recipe is similar to the thin-shell synthesis with slight modifications. Similarly, the CdSe core solution, Zn acetate, ODE, and OA are loaded into a 50mLof quartz flask and stirred at room temperature under vacuum of 0.1-0.2 mbar for at least 1.5 hour. Then, after 50 min evacuation at 90 ˚C, the system is flushed with Argon gas at 85-90 ˚C and 500 µL of OLA is swiftly injected into the flask. Then, injection pump is adjusted. In the beginning, 70 µL octanethiol in 2mLof degassed ODE (prepared in glovebox) is injected with the rate of 4 mL/h for 30 min. Then, Zn-oleate solution [161] is added drop by drop. We wait 5 min until it is properly mixed with the reaction mixture. After that, the 2nd S precursor is added by using the syringe pump with the rate of 5 mL/h, which is composed of 170 µL of octanethiol in 2mLof degassed. After the growth of additional ZnS shell layers for 40 min, the reaction flask is cooled and 5mLof hexane is added. The cleaning procedure is similar to the thin-shell recipe. In

both syntheses, no side products are observed during the cleaning processes pointing out high reaction yield.

7.4.4 Characterization

For optical characterization, measurements were taken with quartz cuvettes by using in-solution samples (in hexane). For collecting absorption spectra of all NPLs, UV-Visible spectrophotometer Varian Cary 100 Bio was used. PL measurements were performed using Varian Cary Eclipse with Xenon lamp at the excitation wavelength of 400 nm. X-ray Powder Diffraction (XRD) spectra were obtained by Panalytical Xpert Pro MPD. The liquid samples were drop casted on a glass slide, evaporated and then their diffraction patterns were collected from 20^{o} to 70^{o}. In order to understand size distribution and elemental ratio of the synthesized NPLs Transmission Electron Microscopy (TEM) and Energy-dispersive X-ray spectroscopy (EDS) were employed using Tecnai G2 F30 at 300 kV voltages. Samples were washed several times with ethanol and dropped on carbon-coated 300-mesh copper grids. Time-Resolved Photoluminescence Spectroscopy measurements were acquired with Pico Quant FluoTime 200 with an excitation laser having wavelength of 375 nm, repetition rate of 2.5 MHz and pulse width of 230 ps. A TimeHarp time-correlated single-photon counting system was utilized to record the fluorescence decays of dilute solutions of NPLs in hexane. The decays were fitted by using the FluoFit software in the deconvolution mode with multiexponential decays.

Absolute Photoluminescence Quantum Yield (QY) Measurements:

Quantum yield of the samples were measured with absolute QY measurement system by using the methodology reported by de Mello et al.[162]. QY measurement setup compose of Ocean Optics Maya 2000 spectrometer, a Hamamatsu integrating sphere, a monochromator integrated Xenon lamp. QY measurements of CdSe/ZnS core/HI shell NPLs were carried out at 400 nm of excitation wavelength.

Chapter 8

8. CONCLUSION and FUTURE PERSPECTIVE

In this thesis work, green, yellow and red emissive CdSe/ZnS QDs have been synthesized as high as 95 % QY to make flexible and efficient color converter films for white-LED application. White-LED performance of the flexible QD films have been characterized by color parameter such as color coordinate, color gamut and color temperature and obtained white light spectrum shows high performance white-LED application.

Nowadays, owing to environmental concerns on Cd-based QDs, InP-based Cd-free QDs have been synthesized in our laboratory with as high as 87 % QY and FWHM value as narrow as 43 nm for various optoelectronic applications.

While optical properties of green emitting Cd-free QDs have been improved significantly in the recent years, the increase in the optical properties of the red emitting QDs have remained limited. Their optical properties should be increased given more effort and new synthetic approach. To increase the usage of Cd-free semiconductor QDs in optoelectronic devices, their optical properties especially QYs and color purity should be further improved by different heterostructure and bandgap engineering. QLED and solar cell performance of the Cd-free samples is far from the Cd-based produced device. To address this issue, Cd-free new synthesis recipe, precursor and structure resolve the problem of low device efficiency.

Cd-based atomically flat NPLs have unique excitonic and electronic structure to be used in many applications especially optical gain and laser. But their low QYs and

low stability limits their usage in some optoelectronic application as QLED. Our new synthesis recipe and near-unity emitting QY samples may lead to high quality QLED device application of the NPLs. Our future perspective and research focus will be LED applications of the NPLs, solar cell applications of the QDs and Cd-free nanoplatelets synthesis.

8.1 Publications

[1] **Y. Altintas**, S. Genç, M. Y. Talpur, E. Mutlugün, "CdSe/ZnS quantum dot films for high performance flexible lighting and display applications," *Nanotechnology*, vol. 27, pp.295604-295612, **2016**

[2] **Y. Altintas**, M. Y. Talpur, M. Ünlü, E. Mutlugün, "Highly Efficient Cd-Free Alloyed Core/Shell Quantum Dots with Optimized Precursor Concentrations," *Journal of Physical Chemistry C*, vol. 120, pp.7885-7892, **2016**

[3] **Y. Altintas**, M.Y. Talpur, E. Mutlugün, "Efficient FRET Donors of In(Zn)P/ZnS Quantum Dots," *Journal of Physical Chemistry C*, vol. 121, no. 5, pp.3034-3043, **2017**.

[4] **Y. Altintas**, A. F. Yazıcı, M. Unlu, Ş. Dadı, S. Genç, E. Mutlugün, "Excitonic interaction amongst InP/ZnS salt pellets, " *Journal of Material Chemistry C*, Journal of Material Chemistry C, vol. 5, pp.7328-7336, 2017.

[5] **Y. Altintas**, M. Y. Talpur, E. Mutlugün, "The Effect of Ligand Chain Length on the Optical Properties of Alloyed Core-Shell InPZnS/ZnS Quantum Dots," *Journal of Alloys and Compounds*, vol. 711, pp.335-341, **2017**.

[6] **Y. Altintas**, M. Y. Talpur, E. Mutlugün, "Cd-free Quantum Dot Pellets for Efficient White Light Generation," *Optics Express*, vol. 25, pp.28371-28384, **2017**.

[7] **Y. Altintas**, N. B. Kiremitler, S. Genç, M. S. Onses, E. Mutlugün, "FRET enabled light harvesting within quantum dot loaded nanofibers, " *J. Phys. D: Appl. Phys.* vol. 51, pp.065111, **2018**.

[8] Ş. Dadı.*, **Y. Altintas***, E. Beskazak, E. Mutlugün, "Plasmonic Enhancement of Perovskite Quantum Dot Films," (***Equal contribution**) ", *MRS Advances*, vol. 3, pp.733-739, **2018**.

[9] **Y. Altintas**, U. Quliyeva, K. Gungor, O. Erdem, Y. Kelestemur, E. Mutlugun, M. V. Kovalenko, and H. V. Demir, "Highly Stable, Near-Unity Efficiency Atomically Flat Semiconductor Nanocrystals of CdSe/ZnS Hetero-Nanoplatelets enabled by ZnS-Shell Hot-Injection Growth," *Small*, DOI:10.1002/smll.201804854, **2019**.

[10] T. Erdem, L. Yang, P. Xu, **Y. Altintas**, T. ONeil, A. Caciagli, C. Ducati, E. Mutlugun, O. A Scherman, E. Eiser, "Inducing transparency in the films of highly scattering particles," *under revision*, **2019**.

BIBLIOGRAPHY

[1] E. A. A. Onushchenko, "Quantum size effect in three-dimensional micorscopic semiconductor crystals," *Jetp Letters*, vol. 34. pp. 345–349, 1981.

[2] N. Yaacobi-Gross, M. Soreni-Harari, M. Zimin, S. Kababya, A. Schmidt, and N. Tessler, "Molecular control of quantum-dot internal electric field and its application to CdSe-based solar cells," *Nat. Mater.*, vol. 10, no. 12, pp. 974–979, 2011.

[3] X. L. Dai *et al.*, "Solution-processed, high-performance light-emitting diodes based on quantum dots," *Nature*, vol. 515, no. 7525, p. 96–+, 2014.

[4] S. S.-W. Kim, S. H. Im, and S. S.-W. Kim, "Performance of light-emitting-diode based on quantum dots.," *Nanoscale*, vol. 5, no. 12, pp. 5205–14, 2013.

[5] K. Roy Choudhury, Y. Sahoo, T. Y. Ohulchanskyy, and P. N. Prasad, "Efficient photoconductive devices at infrared wavelengths using quantum dot-polymer nanocomposites," *Appl. Phys. Lett.*, vol. 87, no. 7, 2005.

[6] C. Liao *et al.*, "Ultralow-Threshold Single-Mode Lasing from Phase-Pure CdSe/CdS Core/Shell Quantum Dots," *J. Phys. Chem. Lett.*, vol. 7, no. 24, pp. 4968–4976, 2016.

[7] B. Guzelturk, Y. Kelestemur, M. Olutas, S. Delikanli, and H. V. Demir, "Amplified spontaneous emission and lasing in colloidal nanoplatelets," *ACS Nano*, vol. 8, no. 7, pp. 6599–6605, 2014.

[8] B. Dubertret, "In Vivo Imaging of Quantum Dots Encapsulated in Phospholipid Micelles," *Science (80-.).*, vol. 298, no. 5599, pp. 1759–1762, 2002.

[9] Y. Zheng, S. Gao, and J. Y. Ying, "Synthesis and cell-imaging applications of glutathione-capped CdTe quantum dots," *Adv. Mater.*, vol. 19, no. 3, pp. 376–380, 2007.

[10] A. C. Samia, X. Chen, and C. Burda, "Semiconductor quantum dots for photodynamic therapy," *J. Am. Chem. Soc.*, vol. 125, pp. 15736–15737, 2003.

[11] C. B. Murray, C. R. Kagan, and M. G. Bawendi, "Synthesis and Characterization of Monodisperse Nanocrystals and Close-Packed Nanocrystal Assemblies," *Annu. Rev. Mater. Sci.*, vol. 30, no. 1, pp. 545–610, 2000.

[12] C. B. Murray, D. J. Norris, and M. G. Bawendi, "Synthesis and characterization of nearly monodisperse CdE (E = sulfur, selenium, tellurium) semiconductor nanocrystallites," *J. Am. Chem. Soc.*, vol. 115, no. 19, pp. 8706–8715, 1993.

[13] P. Reiss, M. Protière, and L. Li, "Core/shell semiconductor nanocrystals," *Small*, vol. 5, no. 2, pp. 154–168, 2009.

[14] C. B. Murray, C. R. Kagan, and M. G. Bawendi, "Synthesis And Characterization Of Monodisperse Nanocrystals And Close -Packed Nanocrystal Assemblies," vol.30, pp. 545–610, 2000.

[15] S. Abe, R. K. Capek, B. De Geyter, and Z. Hens, "Reaction Chemistry/Nanocrystal Property Relations in the Hot Injection Synthesis, the Role of the Solute Solubility," *ACS Nano*, vol. 7, no. 2, pp. 943–949, Feb. 2013.

[16] Z. A. Peng and X. Peng, “Nearly monodisperse and shape-controlled CdSe nanocrystals via alternative routes: Nucleation and growth,” *J. Am. Chem. Soc.*, vol. 124, no. 13, pp. 3343–3353, Apr. 2002.
[17] W. W. Yu and X. Peng, “Formation of High-Quality CdS and Other II-VI Semiconductor Nanocrystals in Noncoordinating Solvents: Tunable Reactivity of Monomers,” *Angew. Chemie Int. Ed.*, vol. 41, no. 13, pp. 2368–2371, Jul. 2002.
[18] N. Pradhan, D. Reifsnyder, R. Xie, J. Aldana, and X. Peng, “Surface Ligand Dynamics in Growth of Nanocrystals,” *J. Am. Chem. Soc.*, vol. 129, no. 30, pp. 9500–9509, Aug. 2007.
[19] Z. A. Peng and X. Peng, “Mechanisms of the Shape Evolution of CdSe Nanocrystals,” *J. Am. Chem. Soc.*, vol. 123, no. 7, pp. 1389–1395, Feb. 2001.
[20] S. Kumar and T. Nann, “Shape Control of II–VI Semiconductor Nanomaterials,” *Small*, vol. 2, no. 3, pp. 316–329, Mar. 2006.
[21] X. Wang, J. Zhuang, Q. Peng, and Y. Li, “A general strategy for nanocrystal synthesis,” *Nature*, vol. 437, no. 7055, pp. 121–124, Sep. 2005.
[22] V. K. LaMer and R. H. Dinegar, “Theory, Production and Mechanism of Formation of Monodispersed Hydrosols,” *J. Am. Chem. Soc.*, vol. 72, no. 11, pp. 4847–4854, Nov. 1950.
[23] G. Konstantatos and E. H. Sargent, *Colloidal Quantum Dot Optoelectronics and Photovoltaics*, 2013th ed. CUP.
[24] I. M. Lifshitz and V. V. Slyozov, “The kinetics of precipitation from supersaturated solid solutions,” *J. Phys. Chem. Solids*, vol. 19, no. 1–2, pp. 35–50, 1961.
[25] M. Grabolle, M. Spieles, V. Lesnyak, N. Gaponik, A. Eychmüller, and U. Resch-Genger, “Determination of the fluorescence quantum yield of quantum dots: Suitable procedures and achievable uncertainties,” *Anal. Chem.*, vol. 81, no. 15, pp. 6285–6294, 2009.
[26] Y. Altintas, S. Genc, M. Y. Talpur, and E. Mutlugun, “CdSe/ZnS quantum dot films for high performance flexible lighting and display applications,” *Nanotechnology*, vol. 27, no. 29, p. 295604, Jul. 2016.
[27] D. V. Talapin, J. H. Nelson, E. V. Shevchenko, S. Aloni, B. Sadtler, and A. P. Alivisatos, “Seeded Growth of Highly Luminescent CdSe/CdS Nanoheterostructures with Rod and Tetrapod Morphologies,” *Nano Lett.*, vol. 7, no. 10, pp. 2951–2959, Oct. 2007.
[28] P. V Kamat, “Quantum Dot Solar Cells. Semiconductor Nanocrystals as Light Harvesters,” *J. Phys. Chem. C*, vol. 112, no. 48, pp. 18737–18753, Dec. 2008.
[29] J. Duan, H. Zhang, Q. Tang, B. He, and L. Yu, “Recent advances in critical materials for quantum dot-sensitized solar cells: A review,” *J. Mater. Chem. A*, vol. 3, no. 34, pp. 17497–17510, 2015.
[30] Z. Jiang *et al.*, “Ultra-sensitive tandem colloidal quantum-dot photodetectors,” *Nanoscale*, vol. 7, no. 39, pp. 16195–16199, 2015.
[31] V. Sukhovatkin, S. Hinds, L. Brzozowski, and E. H. Sargent, “Colloidal quantum-dot photodetectors exploiting multiexciton generation,” *Science (80-.).*, vol. 324, no. 5934, pp. 1542–1544, 2009.
[32] H. V. Demir, S. Nizamoglu, T. Erdem, E. Mutlugun, N. Gaponik, and A. Eychmüller, “Quantum dot integrated LEDs using photonic and excitonic color conversion,” *Nano Today*, vol. 6, no. 6, pp. 632–647, 2011.
[33] X. Yang *et al.*, “A bright cadmium-free, hybrid organic/quantum dot white light-emitting diode,” *Appl. Phys. Lett.*, vol. 101, no. 23, 2012.
[34] G. Konstantatos and E. H. Sargent, *Colloidal Quantum Dot Optoelectronics and*

Photovoltaics, vol. 9780521198. Cambridge: Cambridge University Press, 2013.
[35] "Market Report by Yole Développement: Phosphors-Quantum Dots 2015: LED Down Converters for Lighting and Displays," no. April, 2015.
[36] S. Nizamoglu, G. Zengin, and H. V. Demir, "Color-converting combinations of nanocrystal emitters for warm-white light generation with high color rendering index," *Appl. Phys. Lett.*, vol. 92, no. 3, 2008.
[37] E. Jang, S. Jun, H. Jang, J. Lim, B. Kim, and Y. Kim, "White-light-emitting diodes with quantum dot color converters for display backlights," *Adv. Mater.*, vol. 22, no. 28, pp. 3076–3080, 2010.
[38] T. H. Kim *et al.*, "Full-colour quantum dot displays fabricated by transfer printing," *Nat. Photonics*, vol. 5, no. 3, pp. 176–182, 2011.
[39] K. A. Denault, A. A. Mikhailovsky, S. Brinkley, S. P. Denbaars, and R. Seshadri, "Improving color rendition in solid state white lighting through the use of quantum dots," *J. Mater. Chem. C*, vol. 1, no. 7, pp. 1461–1466, 2013.
[40] M. Grabolle, M. Spieles, V. Lesnyak, N. Gaponik, A. Eychmüller, and U. Resch-Genger, "Determination of the Fluorescence Quantum Yield of Quantum Dots: Suitable Procedures and Achievable Uncertainties," *Anal. Chem.*, vol. 81, no. 15, pp. 6285–6294, Aug. 2009.
[41] E. Mutlugun *et al.*, "Large-Area (over 50 cm × 50 cm) freestanding films of colloidal InP/ZnS quantum dots," *Nano Lett.*, vol. 12, no. 8, pp. 3986–3993, 2012.
[42] T. Erdem and H. V. Demir, "Color science of nanocrystal quantum dots for lighting and displays," *Nanophotonics*, vol. 2, no. 1, pp. 57–81, 2013.
[43] W. K. Bae, K. Char, H. Hur, and S. Lee, "Single-step synthesis of quantum dots with chemical composition gradients," *Chem. Mater.*, vol. 20, no. 2, pp. 531–539, 2008.
[44] W. Ki Bae *et al.*, "Multicolored light-emitting diodes based on all-quantum-dot multilayer films using layer-by-layer assembly method," *Nano Lett.*, vol. 10, no. 7, pp. 2368–2373, 2010.
[45] Y. Altıntas, M. Y. Talpur, M. Ünlü, and E. Mutlugün, "Highly Efficient Cd-Free Alloyed Core/Shell Quantum Dots with Optimized Precursor Concentrations," *J. Phys. Chem. C*, vol. 120, no. 14, pp. 7885–7892, Apr. 2016.
[46] J. Lim, S. Jun, E. Jang, H. Baik, H. Kim, and J. Cho, "Preparation of highly luminescent nanocrystals and their application to light-emitting diodes," *Adv. Mater.*, vol. 19, no. 15, pp. 1927–1932, 2007.
[47] S. Coe, W.-K. Woo, M. Bawendi, and V. Bulović, "Electroluminescence from single monolayers of nanocrystals in molecular organic devices," *Nature*, vol. 420, no. 6917, pp. 800–803, Dec. 2002.
[48] J. Kwak *et al.*, "Bright and efficient full-color colloidal quantum dot light-emitting diodes using an inverted device structure," *Nano Lett.*, vol. 12, no. 5, pp. 2362–2366, 2012.
[49] E. Mutlugun, B. Guzelturk, A. P. Abiyasa, Y. Gao, X. W. Sun, and H. V. Demir, "Colloidal quantum dot light-emitting diodes employing phosphorescent small organic molecules as efficient exciton harvesters," *J. Phys. Chem. Lett.*, vol. 5, no. 16, pp. 2802–2807, 2014.
[50] A. J. Nozik, "Nanoscience and nanostructures for photovoltaics and solar fuels," *Nano Lett.*, vol. 10, no. 8, pp. 2735–2741, 2010.
[51] Y. L. Lee and Y. S. Lo, "Highly efficient quantum-dot-sensitized solar cell based on co-sensitization of CdS/CdSe," *Adv. Funct. Mater.*, vol. 19, no. 4, pp. 604–609, 2009.

[52] Y. Park *et al.*, “Spraying quantum dot conjugates in the colon of live animals enabled rapid and multiplex cancer diagnosis using endoscopy,” *ACS Nano*, vol. 8, no. 9, pp. 8896–8910, 2014.
[53] X. He and N. Ma, “An overview of recent advance of quantum dots for biomedical applications,” *Colloids Surfaces B Biointerfaces*, vol. 124, pp. 118–131, 2014.
[54] F. A. Esteve-Turrillas and A. Abad-Fuentes, “Applications of quantum dots as probes in immunosensing of small-sized analytes,” *Biosens. Bioelectron.*, vol. 41, no. 1, pp. 12–29, 2013.
[55] Y. Zhang and T. H. Wang, “Quantum dot enabled molecular sensing and diagnostics,” *Theranostics*, vol. 2, no. 7, pp. 631–654, 2012.
[56] P. A. S. Jorge, M. Mayeh, R. Benrashid, P. Caldas, J. L. Santos, and F. Farahi, “Applications of quantum dots in optical fiber luminescent oxygen sensors,” *Appl. Opt.*, vol. 45, no. 16, p. 3760, 2006.
[57] Z. Yue *et al.*, “Quantum-dot-based photoelectrochemical sensors for chemical and biological detection,” *ACS Appl. Mater. Interfaces*, vol. 5, no. 8, pp. 2800–2814, 2013.
[58] S. Xu, J. Ziegler, and T. Nann, “Rapid synthesis of highly luminescent InP and InP/ZnS nanocrystals,” *J. Mater. Chem.*, vol. 18, no. 23, pp. 2653–2656, 2008.
[59] H. Virieux *et al.*, “InP/ZnS nanocrystals: Coupling NMR and XPS for fine surface and interface description,” *J. Am. Chem. Soc.*, vol. 134, no. 48, pp. 19701–19708, 2012.
[60] S. Joung, S. Yoon, C. S. Han, Y. Kim, and S. Jeong, “Facile synthesis of uniform large-sized InP nanocrystal quantum dots using tris(tert-butyldimethylsilyl)phosphine,” *Nanoscale Res. Lett.*, vol. 7, no. 1, p. 93, 2012.
[61] P. Reiss, J. Bleuse, and A. Pron, “Highly Luminescent CdSe/ZnSe Core/Shell Nanocrystals of Low Size Dispersion,” *Nano Lett.*, vol. 2, no. 7, pp. 781–784, 2002.
[62] X. Yang *et al.*, “Full Visible Range Covering InP/ZnS Nanocrystals with High Photometric Performance and Their Application to White Quantum Dot Light-Emitting Diodes,” *Adv. Mater.*, vol. 24, no. 30, pp. 4180–4185, Aug. 2012.
[63] J. R. Dethlefsen and A. Døssing, “Preparation of a ZnS shell on CdSe quantum dots using a single-molecular ZnS precursor,” *Nano Lett.*, vol. 11, no. 5, pp. 1964–1969, 2011.
[64] T. D. T. Ung, P. Reiss, and Q. L. Nguyen, “Luminescence properties of In(Zn)P alloy core/ZnS shell quantum dots,” *Appl. Phys. Lett.*, vol. 97, no. 19, p. 193104, 2010.
[65] E. Ryu *et al.*, “Step-Wise Synthesis of InP/ZnS Core−Shell Quantum Dots and the Role of Zinc Acetate,” *Chem. Mater.*, vol. 21, no. 4, pp. 573–575, Feb. 2009.
[66] L. Li and P. Reiss, “One-pot Synthesis of Highly Luminescent InP / ZnS Nanocrystals without,” *J. Am. Chem. Soc.*, vol. 130, pp. 11588–11589, 2008.
[67] S. J. Yang, J. H. Oh, S. Kim, H. Yang, and Y. R. Do, “Realization of InP/ZnS quantum dots for green, amber and red down-converted LEDs and their color-tunable, four-package white LEDs,” *J. Mater. Chem. C*, vol. 3, no. 15, pp. 3582–3591, 2015.
[68] S. Kim *et al.*, “Highly luminescent InP/GaP/ZnS nanocrystals and their application to white light-emitting diodes,” *J. Am. Chem. Soc.*, vol. 134, no. 8, pp. 3804–3809, 2012.
[69] C. Ippen, T. Greco, and A. Wedel, “InP/ZnSe/ZnS: A Novel Multishell System for InP Quantum Dots for Improved Luminescence Efficiency and Its application

in a Light-Emitting Device," *J. Inf. Disp.*, vol. 13, no. 2, pp. 91–95, 2012.
[70] M. D. Tessier, D. Dupont, K. De Nolf, J. De Roo, and Z. Hens, "Economic and Size-Tunable Synthesis of InP / ZnE (E=S, Se) Colloidal Quantum Dots.," *Chem. Mater.*, vol. 27, pp. 4893–4898, 2015.
[71] M. Banski, M. Afzaal, M. A. Malik, A. Podhorodecki, J. Misiewicz, and P. O'Brien, "Special Role for Zinc Stearate and Octadecene in the Synthesis of Luminescent ZnSe Nanocrystals," *Chem. Mater.*, vol. 27, no. 11, pp. 3797–3800, 2015.
[72] T. Kim, S. W. Kim, M. Kang, and S. W. Kim, "Large-scale synthesis of inpzns alloy quantum dots with dodecanethiol as a composition controller," *J. Phys. Chem. Lett.*, vol. 3, no. 2, pp. 214–218, 2012.
[73] T. Mishra, R. K. Sahu, S. H. Lim, L. G. Salamanca-Riba, and S. Bhattacharjee, "Hexadecylamine capped silver and gold nanoparticles: Comparative study on formation and self-organization," *Mater. Chem. Phys.*, vol. 123, no. 2–3, pp. 540–545, 2010.
[74] J. Lim *et al.*, "Highly efficient cadmium-free quantum dot light-emitting diodes enabled by the direct formation of excitons within InP@ZnSeS quantum dots," *ACS Nano*, vol. 7, no. 10, pp. 9019–9026, 2013.
[75] Y. Altıntas, M. Y. Talpur, and E. Mutlugün, "Efficient Förster Resonance Energy Transfer Donors of In(Zn)P/ZnS Quantum Dots," *J. Phys. Chem. C*, vol. 121, no. 5, pp. 3034–3043, 2017.
[76] D. V. Talapin and E. V. Shevchenko, "Introduction: Nanoparticle chemistry," *Chem. Rev.*, vol. 116, no. 18, pp. 10343–10345, 2016.
[77] J. Q. Grim, L. Manna, and I. Moreels, "A sustainable future for photonic colloidal nanocrystals," *Chem. Soc. Rev.*, vol. 44, no. 16, pp. 5897–5914, 2015.
[78] D. Battaglia and X. Peng, "Formation of High Quality InP and InAs Nanocrystals in a Noncoordinating Solvent," *Nano Lett.*, vol. 2, no. 9, pp. 1027–1030, 2002.
[79] A. M. Nightingale and J. C. Demello, "Improving the ensemble optical properties of InP quantum dots by indium precursor modification," *J. Mater. Chem. C*, vol. 4, no. 36, pp. 8454–8458, 2016.
[80] P. Ramasamy, B. Kim, M. S. Lee, and J. S. Lee, "Beneficial effects of water in the colloidal synthesis of InP/ZnS core-shell quantum dots for optoelectronic applications," *Nanoscale*, vol. 8, no. 39, pp. 17159–17168, 2016.
[81] L. Xi *et al.*, "Understanding the role of single molecular ZnS precursors in the synthesis of In(Zn)P/ZnS nanocrystals," *ACS Appl. Mater. Interfaces*, vol. 6, no. 20, pp. 18233–18242, 2014.
[82] L. Xi *et al.*, "Effect of Zinc Incorporation on the Performance of Red Light Emitting InP Core Nanocrystals," *Inorg. Chem.*, vol. 55, no. 17, pp. 8381–8386, 2016.
[83] D. K. Harris and M. G. Bawendi, "Improved precursor chemistry for the synthesis of III-V quantum dots," *J. Am. Chem. Soc.*, vol. 134, no. 50, pp. 20211–20213, 2012.
[84] E. Mutlugun *et al.*, "Highly efficient nonradiative energy transfer mediated light harvesting in water using aqueous CdTe quantum dot antennas.," *Opt. express*, vol. 18, no. 10, pp. 10720–10730, 2010.
[85] A. Thomas, P. V. Nair, and K. G. Thomas, "InP quantum dots: An environmentally friendly material with resonance energy transfer requisites," *J. Phys. Chem. C*, vol. 118, no. 7, pp. 3838–3845, 2014.
[86] B. Guzelturk and H. V. Demir, "Near-Field Energy Transfer Using Nanoemitters For Optoelectronics," *Adv. Funct. Mater.*, vol. 26, no. 45, pp. 8158–8177, 2016.

[87] C. Ai, Y. Ma, C. Yuan, and G. Dong, “Semi-implicit non-hydrostatic model for 2D nonlinear wave interaction with a floating/suspended structure,” *Eur. J. Mech. B/Fluids*, vol. 72, no. 50, pp. 545–560, 2018.
[88] L. Li and P. Reiss, “One-pot Synthesis of Highly Luminescent InP / ZnS Nanocrystals without,” *J. Am. Chem. Soc.*, vol. 130, pp. 11588–11589, 2008.
[89] J. R. Lakowicz, *Principles of Fluorescence Spectroscopy*. New York: Springer, 2007.
[90] Y. Altintas, A. Faruk Yazici, M. Unlu, S. Dadi, S. Genc, and E. Mutlugun, “Excitonic interaction amongst InP/ZnS salt pellets,” *J. Mater. Chem. C*, vol. 5, no. 29, pp. 7328–7336, 2017.
[91] Z. A. Peng and X. Peng, “Formation of High-Quality CdTe, CdSe, and CdS Nanocrystals Using CdO as Precursor,” *J. Am. Chem. Soc.*, vol. 123, no. 1, pp. 183–184, Jan. 2001.
[92] L. Qu and X. Peng, “Control of photoluminescence properties of CdSe nanocrystals in growth,” *J. Am. Chem. Soc.*, vol. 124, no. 9, pp. 2049–2055, 2002.
[93] W. W. Yu, L. Qu, W. Guo, and X. Peng, “Experimental Determination of the Extinction Coefficient of CdTe, CdSe, and CdS Nanocrystals,” *Chem. Mater.*, vol. 15, no. 14, pp. 2854–2860, Jul. 2003.
[94] S. Kim, B. Fisher, H. J. Eisler, and M. Bawendi, “Type-II quantum dots: CdTe/CdSe(core/shell) and CdSe/ZnTe(core/shell) heterostructures,” *J. Am. Chem. Soc.*, vol. 125, no. 38, pp. 11466–11467, 2003.
[95] D. V Talapin, I. Mekis, S. Götzinger, A. Kornowski, O. Benson, and H. Weller, “CdSe/CdS/ZnS and CdSe/ZnSe/ZnS Core−Shell−Shell Nanocrystals,” *J. Phys. Chem. B*, vol. 108, no. 49, pp. 18826–18831, Dec. 2004.
[96] Y. Altintas, S. Genc, M. Y. Talpur, and E. Mutlugun, “CdSe/ZnS quantum dot films for high performance flexible lighting and display applications,” *Nanotechnology*, vol. 27, no. 29, p. 295604, 2016.
[97] R. Hardman, “A toxicologic review of quantum dots: Toxicity depends on physicochemical and environmental factors,” *Environ. Health Perspect.*, vol. 114, no. 2, pp. 165–172, 2006.
[98] O. I. Micic, C. J. Curtis, K. M. Jones, J. R. Sprague, and A. J. Nozik, “Synthesis and Characterization of InP Quantum Dots,” *J. Phys. Chem.*, vol. 98, no. 19, pp. 4966–4969, 1994.
[99] S. Xu, J. Ziegler, and T. Nann, “Rapid synthesis of highly luminescent InP and InP/ZnS nanocrystals,” *J. Mater. Chem.*, vol. 18, no. 23, p. 2653, 2008.
[100] R. Xie, D. Battaglia, and X. Peng, “Colloidal InP Nanocrystals as Efficient Emitters Covering Blue to Near-Infrared,” *J. Am. Chem. Soc.*, vol. 129, no. 50, pp. 15432–15433, 2007.
[101] “Website:” [Online]. Available: https://technology.ihs.com/586177/display-dynamics quantum-dots-to-cement-itself-as-a-mainstream-wide-colorgamut-display-solution.
[102] P. Pust, P. J. Schmidt, and W. Schnick, “A revolution in lighting,” *Phys. World*, vol. 18, no. 7, p. 13, 2005.
[103] C. C. Lin and R. S. Liu, “Advances in phosphors for light-emitting diodes,” *J. Phys. Chem. Lett.*, vol. 2, no. 11, pp. 1268–1277, 2011.
[104] P. O. Anikeeva, J. E. Halpert, M. G. Bawendi, and V. Bulović, “Quantum dot light-emitting devices with electroluminescence tunable over the entire visible spectrum,” *Nano Lett.*, vol. 9, no. 7, pp. 2532–2536, 2009.
[105] W. S. Song and H. Yang, “Efficient white-light-emitting diodes fabricated from

highly fluorescent copper indium sulfide core/shell quantum dots," *Chem. Mater.*, vol. 24, no. 10, pp. 1961–1967, 2012.
[106] T. Otto *et al.*, "Colloidal nanocrystals embedded in macrocrystals: Robustness, photostability, and color purity," *Nano Lett.*, vol. 12, no. 10, pp. 5348–5354, 2012.
[107] A. Benad *et al.*, "Cold Flow as Versatile Approach for Stable and Highly Luminescent Quantum Dot-Salt Composites," *ACS Appl. Mater. Interfaces*, vol. 8, no. 33, pp. 21570–21575, 2016.
[108] M. Adam *et al.*, "Liquid-liquid diffusion-assisted crystallization: A fast and versatile approach toward high quality mixed quantum dot-salt crystals," *Adv. Funct. Mater.*, vol. 25, no. 18, pp. 2638–2645, 2015.
[109] M. Adam, N. Gaponik, A. Eychmüller, T. Erdem, Z. Soran-Erdem, and H. V. Demir, "Colloidal Nanocrystals Embedded in Macrocrystals: Methods and Applications," *J. Phys. Chem. Lett.*, vol. 7, no. 20, pp. 4117–4123, 2016.
[110] M. Adam, R. Tietze, N. Gaponik, and A. Eychmüller, "QD-salt mixed crystals: The influence of salt-type, free-stabilizer, and pH," *Zeitschrift fur Phys. Chemie*, vol. 229, no. 1–2, pp. 109–118, 2015.
[111] B. Guzelturk and H. V. Demir, "Near-Field Energy Transfer Using Nanoemitters For Optoelectronics," *Adv. Funct. Mater.*, vol. 26, no. 45, pp. 8158–8177, 2016.
[112] J. B. Hoffman, H. Choi, and P. V. Kamat, "Size-dependent energy transfer pathways in CdSe quantum dot-squaraine light-harvesting assemblies: Förster versus dexter," *J. Phys. Chem. C*, vol. 118, no. 32, pp. 18453–18461, 2014.
[113] A. Gopi, S. Lingamoorthy, S. Soman, K. Yoosaf, R. Haridas, and S. Das, "Modulating FRET in Organic–Inorganic Nanohybrids for Light Harvesting Applications," *J. Phys. Chem. C*, vol. 120, no. 46, pp. 26569–26578, 2016.
[114] L. Yuan, W. Lin, K. Zheng, and S. Zhu, "FRET-based small-molecule fluorescent probes: Rational design and bioimaging applications," *Acc. Chem. Res.*, vol. 46, no. 7, pp. 1462–1473, 2013.
[115] M. Li, H. Gou, I. Al-Ogaidi, and N. Wu, "Nanostructured sensors for detection of heavy metals: A review," *ACS Sustain. Chem. Eng.*, vol. 1, no. 7, pp. 713–723, 2013.
[116] T. Erdem, Z. Soran-Erdem, Y. Kelestemur, N. Gaponik, and H. V. Demir, "Excitonic improvement of colloidal nanocrystals in salt powder matrix for quality lighting and color enrichment," *Opt. Express*, vol. 24, no. 2, p. A74, 2016.
[117] Y. Altintas, U. Quliyeva, K. Gungor, O. Erdem, Y. Kelestemur, E. Mutlugun, M. V. Kovalenko, H. V. Demir "Highly Stable, Near-Unity Efficiency Atomically Flat Semiconductor Nanocrystals of CdSe/ZnS Hetero- Nanoplatelets Enabled by ZnS-Shell Hot-Injection Growth," *Small*, doi: 10.1002/smll.201804854, 2019.
[118] D. V. Talapin, J.-S. Lee, M. V. Kovalenko, and E. V. Shevchenko, "Prospects of Colloidal Nanocrystals for Electronic and Optoelectronic Applications," *Chem. Rev.*, vol. 110, no. 1, pp. 389–458, 2010.
[119] M. A. Hines and P. Guyot-Sionnest, "Synthesis and characterization of strongly luminescing ZnS-capped CdSe nanocrystals," *J. Phys. Chem.*, vol. 100, no. 2, pp. 468–471, 1996.
[120] B. O. Dabbousi *et al.*, "(CdSe)ZnS Core−Shell Quantum Dots: Synthesis and Characterization of a Size Series of Highly Luminescent Nanocrystallites," *J. Phys. Chem. B*, vol. 101, no. 46, pp. 9463–9475, 1997.
[121] Z. A. Peng and X. Peng, "Formation of high-quality CdTe, CdSe, and CdS nanocrystals using CdO as precursor [6]," *J. Am. Chem. Soc.*, vol. 123, no. 1, pp. 183–184, 2001.

[122] O. I. Micic, C. J. Curtis, K. M. Jones, J. R. Sprague, and A. J. Nozik, “Synthesis and Characterization of InP Quantum Dots,” *J. Phys. Chem.*, vol. 98, no. 19, pp. 4966–4969, 1994.
[123] S. Ithurria and B. Dubertret, “Quasi 2D Colloidal CdSe Platelets with Thicknesses Controlled at the Atomic Level,” *J. Am. Chem. Soc.*, vol. 130, no. 49, pp. 16504–16505, 2008.
[124] M. Olutas, B. Guzelturk, Y. Kelestemur, A. Yeltik, S. Delikanli, and H. V. Demir, “Lateral Size-Dependent Spontaneous and Stimulated Emission Properties in Colloidal CdSe Nanoplatelets,” *ACS Nano*, vol. 9, no. 5, pp. 5041–5050, 2015.
[125] M. D. Tessier, C. Javaux, I. Maksimovic, V. Loriette, and B. Dubertret, “Spectroscopy of single CdSe nanoplatelets,” *ACS Nano*, vol. 6, no. 8, pp. 6751–6758, 2012.
[126] A. Yeltik, S. Delikanli, M. Olutas, Y. Kelestemur, B. Guzelturk, and H. V. Demir, “Experimental Determination of the Absorption Cross-Section and Molar Extinction Coefficient of Colloidal CdSe Nanoplatelets,” *J. Phys. Chem. C*, vol. 119, no. 47, pp. 26768–26775, 2015.
[127] C. She *et al.*, “Low-Threshold Stimulated Emission Using Colloidal Quantum Wells,” *Nano Lett.*, vol. 14, no. 5, pp. 2772–2777, May 2014.
[128] B. Guzelturk, Y. Kelestemur, M. Olutas, S. Delikanli, and H. V. Demir, “Amplified spontaneous emission and lasing in colloidal nanoplatelets,” *ACS Nano*, vol. 8, no. 7, pp. 6599–6605, 2014.
[129] B. Liu, S. Delikanli, Y. Gao, D. Dede, K. Gungor, and H. V. Demir, “Nanocrystal light-emitting diodes based on type II nanoplatelets,” *Nano Energy*, vol. 47, no. November 2017, pp. 115–122, 2018.
[130] S. J. Lim, W. Kim, and S. K. Shin, “Surface-dependent, ligand-mediated photochemical etching of CdSe nanoplatelets,” *J. Am. Chem. Soc.*, vol. 134, no. 18, pp. 7576–7579, 2012.
[131] M. D. Tessier, B. Mahler, B. Nadal, H. Heuclin, S. Pedetti, and B. Dubertret, “Spectroscopy of colloidal semiconductor core/shell nanoplatelets with high quantum yield,” *Nano Lett.*, vol. 13, no. 7, pp. 3321–3328, 2013.
[132] S. Ithurria and D. V. Talapin, “Colloidal Atomic Layer Deposition (c-ALD) using self-limiting reactions at nanocrystal surface coupled to phase transfer between polar and nonpolar media,” *J. Am. Chem. Soc.*, vol. 134, no. 45, pp. 18585–18590, 2012.
[133] J. Zhou, M. Zhu, R. Meng, H. Qin, and X. Peng, “Ideal CdSe/CdS Core/Shell Nanocrystals Enabled by Entropic Ligands and Their Core Size-, Shell Thickness-, and Ligand-Dependent Photoluminescence Properties,” *J. Am. Chem. Soc.*, vol. 139, no. 46, pp. 16556–16567, 2017.
[134] C. E. Rowland, I. Fedin, B. T. Diroll, Y. Liu, D. V. Talapin, and R. D. Schaller, “Elevated Temperature Photophysical Properties and Morphological Stability of CdSe and CdSe/CdS Nanoplatelets,” *J. Phys. Chem. Lett.*, vol. 9, no. 2, pp. 286–293, 2018.
[135] A. Polovitsyn *et al.*, “Synthesis of Air-Stable CdSe/ZnS Core-Shell Nanoplatelets with Tunable Emission Wavelength,” *Chem. Mater.*, vol. 29, no. 13, pp. 5671–5680, 2017.
[136] B. Mahler, B. Nadal, C. Bouet, G. Patriarche, and B. Dubertret, “Core/shell colloidal semiconductor nanoplatelets,” *J. Am. Chem. Soc.*, vol. 134, no. 45, pp. 18591–18598, 2012.
[137] A. A. Rossinelli, A. Riedinger, P. Marqués-Gallego, P. N. Knüsel, F. V.

Antolinez, and D. J. Norris, “High-temperature growth of thick-shell CdSe/CdS core/shell nanoplatelets,” *Chem. Commun.*, vol. 53, no. 71, pp. 9938–9941, 2017.
[138] S. Yadav, A. Singh, L. Thulasidharan, and S. Sapra, “Surface Decides the Photoluminescence of Colloidal CdSe Nanoplatelets Based Core/Shell Heterostructures,” *J. Phys. Chem. C*, vol. 122, no. 1, pp. 820–829, 2018.
[139] H. Cruguel *et al.*, “Electronic structure of CdSe-ZnS 2D nanoplatelets,” *Appl. Phys. Lett.*, vol. 110, no. 15, 2017.
[140] J. Cui *et al.*, “Evolution of the Single-Nanocrystal Photoluminescence Linewidth with Size and Shell: Implications for Exciton-Phonon Coupling and the Optimization of Spectral Linewidths,” *Nano Lett.*, vol. 16, no. 1, pp. 289–296, 2016.
[141] L. T. Kunneman *et al.*, “Nature and decay pathways of photoexcited states in CdSe and CdSe/CdS nanoplatelets,” *Nano Lett.*, vol. 14, no. 12, pp. 7039–7045, 2014.
[142] M. L. H. Green, “A new approach to the formal classification of covalent compounds of the elements,” *J. Organomet. Chem.*, vol. 500, pp. 127–148, 1995.
[143] M. L. H. Green and G. Parkin, “Application of the covalent bond classification method for the teaching of inorganic chemistry,” *J. Chem. Educ.*, vol. 91, no. 6, pp. 807–816, 2014.
[144] B. Fritzinger, R. K. Capek, K. Lambert, J. C. Martins, and Z. Hens, “Utilizing Self-Exchange To Address the Binding of Carboxylic Acid Ligands to CdSe Quantum Dots,” *J. Am. Chem. Soc.*, no. 23, pp. 10195–10201, 2010.
[145] F. Yan *et al.*, “Highly Efficient Visible Colloidal Lead-Halide Perovskite Nanocrystal Light-Emitting Diodes,” *Nano Lett.*, vol. 18, no. 5, pp. 3157–3164, 2018.
[146] P. Ramasamy, D. H. Lim, B. Kim, S. H. Lee, M. S. Lee, and J. S. Lee, “All-inorganic cesium lead halide perovskite nanocrystals for photodetector applications,” *Chem. Commun.*, vol. 52, no. 10, pp. 2067–2070, 2016.
[147] Y. Bi, S. Pradhan, S. Gupta, M. Z. Akgul, A. Stavrinadis, and G. Konstantatos, “Infrared Solution-Processed Quantum Dot Solar Cells Reaching External Quantum Efficiency of 80% at 1.35 μm and Jscin Excess of 34 mA cm−2,” *Adv. Mater.*, vol. 30, no. 7, pp. 1–6, 2018.
[148] J. Q. Grim *et al.*, “Continuous-wave biexciton lasing at room temperature using solution-processed quantum wells,” *Nat. Nanotechnol.*, vol. 9, no. 11, pp. 891–895, Nov. 2014.
[149] C. E. Rowland and R. D. Schaller, “Exciton fate in semiconductor nanocrystals at elevated temperatures: Hole trapping outcompetes exciton deactivation,” *J. Phys. Chem. C*, vol. 117, no. 33, pp. 17337–17343, 2013.
[150] H. C. Y. Yu, S. G. Leon-Saval, A. Argyros, and G. W. Barton, “Temperature Effects on Emission of Quantum Dots Embedded in Polymethylmethacrylate,” *Appl. Opt.*, vol. 49, no. 15, pp. 2749–2752, 2010.
[151] Y. Zhao, C. Riemersma, F. Pietra, R. Koole, C. De Mello Donegá, and A. Meijerink, “High-temperature luminescence quenching of colloidal quantum dots,” *ACS Nano*, vol. 6, no. 10, pp. 9058–9067, 2012.
[152] B. T. Diroll and C. B. Murray, “High-temperature photoluminescence of CdSe/CdS core/shell nanoheterostructures,” *ACS Nano*, vol. 8, no. 6, pp. 6466–6474, 2014.
[153] O. Chen *et al.*, “Compact high-quality CdSe-CdS core-shell nanocrystals with narrow emission linewidths and suppressed blinking,” *Nat. Mater.*, vol. 12, no. 5, pp. 445–451, 2013.

[154] M. Pelton, “Carrier Dynamics, Optical Gain, and Lasing with Colloidal Quantum Wells,” *J. Phys. Chem. C*, vol. 122, no. 20, pp. 10659–10674, 2018.
[155] B. Guzelturk *et al.*, “Stable and low-threshold optical gain in CdSe/CdS quantum dots: An all-colloidal frequency up-converted laser,” *Adv. Mater.*, vol. 27, no. 17, pp. 2741–2746, 2015.
[156] V. I. Klimov, A. A. Mikhailovsky, D. W. McBranch, C. A. Leatherdale, and M. G. Bawendi, “Quantization of multiparticle Auger rates in semiconductor quantum dots,” *Science (80-.).*, vol. 287, no. 5455, pp. 1011–1014, 2000.
[157] Q. Li and T. Lian, “Area- and Thickness-Dependent Biexciton Auger Recombination in Colloidal CdSe Nanoplatelets: Breaking the ‘Universal Volume Scaling Law,’” *Nano Lett.*, vol. 17, no. 5, pp. 3152–3158, 2017.
[158] Y. Kelestemur, B. Guzelturk, O. Erdem, M. Olutas, K. Gungor, and H. V. Demir, “Platelet-in-Box Colloidal Quantum Wells: CdSe/CdS@CdS Core/Crown@Shell Heteronanoplatelets,” *Adv. Funct. Mater.*, vol. 26, no. 21, pp. 3570–3579, 2016.
[159] Y. Kelestemur, D. Dede, K. Gungor, C. F. Usanmaz, O. Erdem, and H. V. Demir, “Alloyed Heterostructures of CdSexS1-xNanoplatelets with Highly Tunable Optical Gain Performance,” *Chem. Mater.*, vol. 29, no. 11, pp. 4857–4865, 2017.
[160] M. D. Tessier, P. Spinicelli, D. Dupont, G. Patriarche, S. Ithurria, and B. Dubertret, “Efficient exciton concentrators built from colloidal core/crown CdSe/CdS semiconductor nanoplatelets,” *Nano Lett.*, vol. 14, no. 1, pp. 207–213, 2014.
[161] H. C. Wang *et al.*, “Cadmium-Free InP/ZnSeS/ZnS Heterostructure-Based Quantum Dot Light-Emitting Diodes with a ZnMgO Electron Transport Layer and a Brightness of Over 10 000 cd m−2,” *Small*, vol. 13, no. 13, pp. 1–7, 2017.
[162] John C. de Mello, H. Felix Wittmann, and Richard H. Friend, “An Improved Experimental Determination of External Photoluminescence Quantum Efficiency,” *Adv. Mater.*, vol. 9, no. 3, pp. 230–232, 1997.